Università degli Studi di Cagliari

**DOTTORATO DI RICERCA**

Ingegneria del Territorio

Ciclo XXVI

# On the Turbulence in Negatively Buoyant Jets

Settore scientifico disciplinare di afferenza

ICAR/01 Idraulica


| | |
|---|---|
| Presentata da: | Besalduch Luigi Antonio |
| Coordinatore Dottorato | Prof. Roberto Deidda |
| Relatori | Prof. Giorgio Querzoli<br>Dott. Maria Grazia Badas |


Esame finale anno accademico 2012 – 2013

UNIONE EUROPEA
Fondo sociale europeo

REGIONE AUTONOMA DELLA SARDEGNA

FSE 2007-2013
POR SARDEGNA
obiettivo competitività regionale e occupazione

UNIVERSITA' DEGLI STUDI DI CAGLIARI

La presente tesi è stata prodotta durante la frequenza del corso di dottorato in Ingegneria del Territorio dell'Università degli Studi di Cagliari, a.a. 2012/2013 - XXVI ciclo, con il supporto di una borsa di studio finanziata con le risorse del P.O.R. SARDEGNA F.S.E. 2007-2013 - Obiettivo competitività regionale e occupazione, Asse IV Capitale umano, Linea di Attività l.3.1 "Finanziamento di corsi di dottorato finalizzati alla formazione di capitale umano altamente specializzato, in particolare per i settori dell'ICT, delle nanotecnologie e delle biotecnologie, dell'energia e dello sviluppo sostenibile, dell'agroalimentare e dei materiali tradizionali".

Luigi Antonio Besalduch gratefully acknowledges Sardinia Regional Government for the financial support of her PhD scholarship (P.O.R. Sardegna F.S.E. Operational Programme of the Autonomous Region of Sardinia, European Social Fund 2007-2013 - Axis IV Human Resources, Objective l.3, Line of Activity l.3.1.).

# Acknowledgments

Un sincero ringraziamento va al Prof. Giorgio Querzoli per aver condiviso con me la sua enorme esperienza e le sue conoscenze, e per avermi dato tante opportunità di confronto e di miglioramento.

Desidero ringraziare inoltre la Dott.ssa Maria Grazia Badas e il Dott. Simone Ferrari, per i loro preziosi insegnamenti, per la pazienza e la disponibilità, nell'accompagnarmi in questo percorso di crescita scientifica e personale.

Il vostro supporto sia durante i periodi di successo, che durante quelli di stallo, è stato veramente apprezzato.

Un grazie va al Prof. Roberto Verzicco, per avermi iniziato allo studio della Fluidodinamica Computazionale.

Un infinito grazie va inoltre ad Antonio, per il suo supporto tecnico nelle simulazioni sperimentali, per aver con pazienza e disponibilità assecondato le mie infinite richieste ... ma anche per l'amicizia, il conforto ... e i tanti caffè.

Desidero ringraziare mio padre e mia madre, che con il loro affettuoso aiuto hanno reso meno impegnative le fatiche del lavoro, per tutto quello che hanno fatto e continueranno a fare, sperando siano sempre orgogliosi di me.

Un grazie ad Antonella che mi è sempre stata vicina con il suo paziente amore.

Un pensiero va inoltre ai tanti amici, dentro e fuori il mondo accademico, incontrati in giro per l'Europa durante questi tre anni indimenticabili.

# Contents

## Chapter 1: Introduction



## Chapter 2: State of the art



## Chapter 3: Theoretical analysis of buoyant jets

## Chapter 7: Experimental Results

# Chapter 1

# Introduction

## 1.1 - Introduction

A simple jet is a discharge of fluid from an orifice into a receiving body of the same or a similar fluid, and it is produced by a source of momentum (figure 1.1). A plume is similar to a jet, but it is caused by a potential energy source that provides buoyancy to the fluid of a source (figure 1.2).

**Figure 1.1 Simple Jet with high Reynolds number produced by a rocket.**

Apparently, the behaviour is similar, but the mechanisms that govern the entrainment (the drag of ambient fluid into the flow that increases its mass flux) and the mixing (occurs when two fluid are allowed or forced to flow together, reducing the length scales by stretching or breakup) are different. In the Simple Jet, they are due to the inertia of the turbulent eddies but in the plume are by the inertia generated by the buoyancy forces.

Figure 1.2 Fire in the Deep-water Horizon oil drilling into the Gulf of Mexico.

The mechanisms that govern the entrainment are different depending on the flow regime, in particular in a laminar jet (or plume); it is caused by viscous drag, while in the turbulent case it is a result of the convoluted outer boundary of the jet which continually engulfs external fluid. Far from the jet, there is a small but finite flow towards the jet which feeds its increasing girth (figure 1.3).

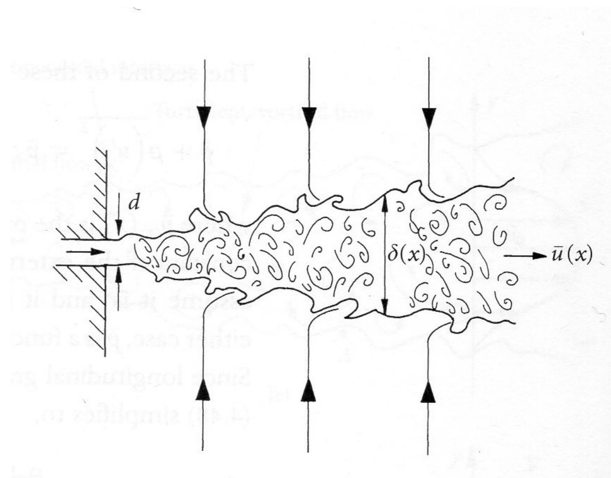


Figure 1.3 Entrainment in a jet

Many of the flows in nature are classified as buoyant jets, which are derived from sources of both momentum and buoyancy. They are flows that develop when a denser fluid is discharged into a lighter receiving body, or downwards into a heavier one. The initial flow is driven mostly by the momentum, and the behaviour is typical of a simple jet, further the buoyancy prevails bending the jet, and making it similar to a plume (figure 1.4).

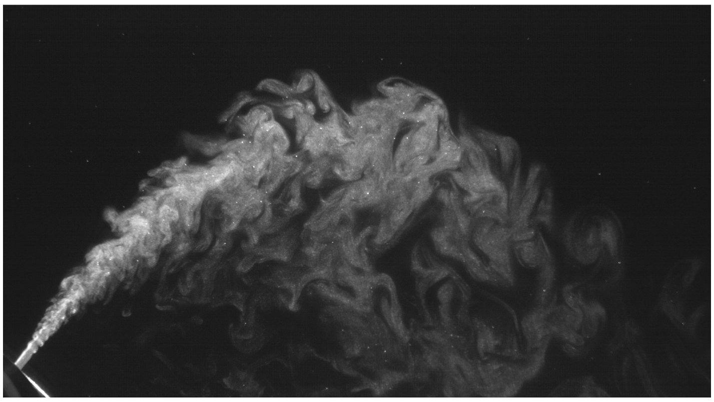

Figure 1.4 Buoyant Jet investigated with a LIV technique

This thesis focuses in particular in turbulent Negatively Buoyant jets (NBJs), so discharges of dense effluent into lighter receiving fluid. One of the most common practical cases of a NBJ is the discharge of domestic and industrial wastewater or brine by submarine outfall.

## 1.2 - Objective

A discharge near a beach could contaminate it, and could cause health risks and damages to the fauna and flora. This impact can be almost completely eliminated by using efficient diffusers. The dilution using diffusers instead of solely discharging the fluid at the end of a pipe could reach values ranging from 1:100 up to 1:1000, since the jets entrain large volumes of ambient fluid and mix it. Moreover, this kind of release with this level of dilution does not need advanced treatments. Consequently, in order to design an efficient outfall that allows these results, the understanding of the turbulence processes and the parameters governing their behaviour are needed.

The objective of this study is, therefore, to better understand the fluid dynamics of NBJs by both experimental and numerical approaches.

Typically, these flows are investigated using Light Induced Fluorescence (LIF), i.e. concentration fields are the only measured quantities. The novel approach of this research is the use of image analysis techniques to determine the velocity field in NBJs, which is very poorly investigated in the literature. In particular, a novel algorithm (Feature Tracking Velocimetry, FTV) was applied, which is very useful in the presence of difference seeding density and high velocity gradients.

The fluid is released through a sharp-edged orifice; this kind of release has never been used in dense jet studies, although it allows larger entrainment than contoured orifice or at the end of a long pipe (Mi et al. 2007). To investigate the effect of the nozzle shape on the upstream flow (due to the presence of vena contracta, i.e. the smallest cross sectional area of the jet, which is the consequence of bending the streamlines towards the exit area) and on the contraction coefficient, Light Induced Visualization (LIV) was used. It is similar to Light Induced Fluorescence. In this technique titanium dioxide was applied, which scatters light all over the spectrum, instead of fluoresceine which emits at a single wavelength.

Another objective of this work is a preliminary numerical investigation of NBJs using a non-commercial numerical model, based on Immersed boundary algorithm. The choice of this kind of model allows the simulation of NBJs with an easier geometrical representation of the diffuser, without refining the grid along the path of the jet, being unknown a priori.

The results have been compared to the data of simple jets, i.e. Quinn (2006), Mi et al. (2007), and Pope (2000), to study the different behaviour and the numerical problems of buoyancy in a new way.

The aim of the present study is also to provide results that can be useful for the development and validation of future numerical and experimental models.

The experiments were performed varying the density, and the inclination of the release, focusing in particular on the angle of maximum dilution of 65°.

## 1.3 - Outline of the thesis

The thesis is structured into nine chapters. In Chapter 1, the objective and the scope of this study are described, followed by a short introduction. Chapter 2 presents the current understanding of this phenomenon, with a summary of the previous experiments and numerical simulations about negatively buoyant jets. Chapter 3 and 4 show the theoretical aspects of jets and plumes, and the basic governing equations useful for the numerical simulations of buoyant jets. In Chapter 5 we introduce the experimental set-up and the procedure for the simulation of NBJs. In Chapter 6 we overview the image analysis techniques, furthermore present and validate the FTV algorithm. In Chapter 7 we present some of the most representative results. In Chapter 8 the numerical model of the simulation is explained. Finally, in Chapter 9 we summarize and discuss the results.

# Chapter 2

# State of the art

## 2.1 - Introduction

There are many cases of practical interest of release of effluent heavier than the environmental fluid: gypsum or acidic wastes from fertilizer factories (Roberts et al., 1997), oil or gas drilling facilities, leaching of mineral salts domes (James et al., 1983; McLellanet al., 1986), sea discharges of effluents from wastewater treatment plants (Kohet al., 1975), ventilation of aircraft hangars heated using ceiling-mounted fans (Baines et al.,1990), forced mixing in reservoirs and harbours to improve the water quality ( McClimans et al., 2000), vehicle exhausts and accidental leaks of hazardous gases (Lane-Serff et al., 1993), the replenishment of magma chambers in the Earth's crust (Turner et al., 1966; Campbell et al., 1989), explosive volcanic jets (Kaminski et al., 2004), replenishing of cold salt water at the bottom of solar ponds (Caruso et al., 2001), cooling water discharges from liquefied natural gas plants (Lai and Lee, 2012), or two-phase jets as snow exits from snow ploughs (Lindberg et al., 1991), sand and slurry jets as dredging and island building operations and pulverized coal combustion (Hall et al, 2010).

One of the most important applications of Negative Buoyant Jets is certainly sea discharge of brine from desalination plants through submerged outfalls: their diffusion in the last years is due to the water scarcity, climatic change and growing population (Palomar et al., 2010). The release of the brine from these plants can have impact on the environment, because elevated salinity may cause the inhibition of the growth of marine species and the reduction of fish cultures (Milione and Zeng, 2008).

NBJ has been studied extensively; an overview of the most important works on this subject is discussed below.

## 2.2 - Experimental studies

### 2.2.1 Experimental methods

The earlier experimental studies of this phenomenon were carried out with a variety of techniques. Investigations were performed by means of visual observation, single point measurements with probes or suction pipes, and with image analysis techniques.

The typical instruments used for single point measurements of concentration are conductivity probes, which employ a potentiometric method and several electrodes to relate the measured voltage to the concentration of the solution.

The traditional systems to measure velocity in a single point of a flow are: pitot tubes, Laser Doppler Anemometry (LDA), Hot-wire Anemometry (HWA), and Flying Hot-Wire anemometry (FHW) (Kleppe et al. 2000).

All of them provide the time history of velocity in a single point of space and, if a spatial investigation is needed, a large number of probes must be used. Their advantage is mainly the high frequency response (more than 100 Hz), on the other hand their main disadvantage is the intrusiveness, i.e. they need calibration and it is difficult to obtain results over a large area of interest.

Nowadays, Image analysis (IA) techniques are most commonly used, since they allow non-intrusive quantitative measurements as well as multi-point measurements. The most adopted techniques are Light Attenuation (LA) and Light-Induced Fluorescence (LIF) for concentration measurements, Particle Image Velocimetry (PIV) and Particle Tracking Velocimetry (PTV) for velocity measurements. IA techniques provide measurements all over the investigation field, they are not intrusive and, do not need any particular calibration.

- **Light Attenuation (LA)**. In this technique, the flow acts between the camera and the light source, therefore integrated concentration is measured. When the light passes through a dye, its intensity is reduced proportionally to the concentration.
- **Laser Induced Fluorescence (LIF)**. To excite the fluorescent dye (for example fluoresceine), a light sheet is produced in the test section, and the concentration can be computed being proportional to the dye.
- **Particle Image Velocimetry (PIV)** (see Adrian 1991, Bergthorson and Dimotakis 2006) and **Particle Tracking Velocimetry (PTV)** (see Adrian 1991, Dalziel 1992, Querzoli 1996). The flow is seeded with neutrally buoyant particles, and the velocity field can be determined following the particles patterns. In the PIV technique, the displacement is obtained by means of the auto/cross correlation, while in the PTV by identifying the individual particles into successive frames. In these

techniques a plane of the flow must be lighted with a laser or a light source.

### 2.2.2 Vertical Buoyant Jets

Many studies were dedicated to vertical Negatively Buoyant jets (NBJs).One of the first studies was conducted by Turner (1966): salt water was discharged from a reservoir into a plexiglass tank filled with fresh water. The setup was compared to a plume. The authors measured the variation of the maximum height as function of time by visual observation. Using dimensional analysis he showed that the characteristic lengths of the jet (like the maximum height of rise and the level dilution in the impact point) can be expressed in terms of the discharge conditions: the density of the solution of the receiving body, the diameter of the orifice, the exit velocity and the inclination of the discharge.

James et al. (1983) simulated the discharge of brine into a stagnant ambient, which represented a reserve in the salt domes along the Gulf of Mexico. The authors studied the dilution and the maximum height of rise of NBJs using a 1:10 scale model, varying the nozzle diameter and the outlet velocity. The experimental data were compared to the measured data of the full scale discharge. They focused on the problems related to the continuous discharging, that could cause the formation of a layer of undiluted brine, and consequently the reduction of the maximum height of the jet.

Cressewell et al. (1993) showed that in vertical flows it is possible to identify the formation of three different flow regions (figure 2.1): a central jet flow, an annular reverse flow, and the “cap” region where the flow reverses and falls.

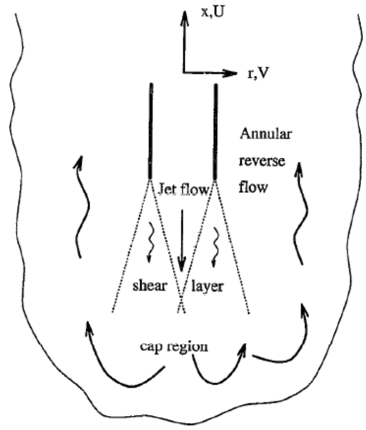


**Figure 2.1 A schematic diagram of the flow field in a negative buoyant jet (Cressewell et al. 1993)**

Zhang et al. (1998) focused mainly on the jet height and its decrease due to the buoyancy effect. They showed also that the maximum height of rise is inversely proportional to the density of the discharge, and for small density, the mass flux had no effect on the maximum jet penetration. For high density the reduction of the dimensionless penetration is apparent.

Cuthbertson et al. (2006) studied the influence of localized patch of turbulence on vertical buoyant jets. In particular, they found that the core of the buoyant jet is arrested at a critical distance from its source, which is determined by the relative strength of the source momentum, buoyancy, and the intensity distribution of the turbulence within the patch. That distance is smaller than the one of a simple jet.

Yannoupoulos et al. (2006a, 2006b) focused on the interaction from 2 to 5 Vertical Buoyant jets in a still ambient fluid, the centreline axial velocities were determined using IA technique; the concentrations were measured using a conductivity probe. The authors developed an integral method, which is based on the partial differential equations of continuity, momentum and tracer, with the assumption of Gaussian profiles of the mean axial velocity and the mean concentration.

### 2.2.3 Concentration measurements in inclined buoyant jets

To our knowledge, most probably Bosanquet et al. (1961) wrote one of the first papers based on inclined NBJs. The authors simulated horizontal and 45° inclined jets using the experimental set-up, which is shown schematically in Figure 2.2.They discharged diluted magnetite slurry that allows the visualization and density increase of the jet.

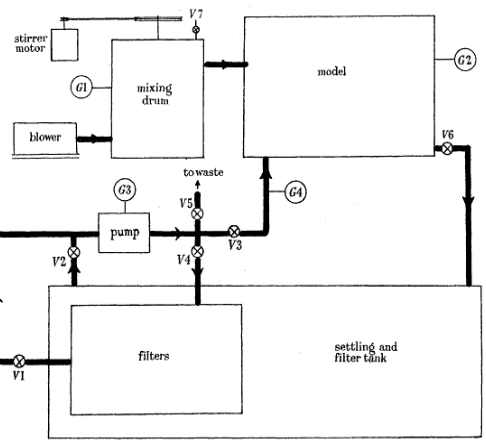


**Figure 2.2 Experimental setup of Bousanquet et al. 1961**

Instantaneous photographs were presented, but due to the intense concentration of the slurry, the jet is uniformly dark (figure 2.3), and the authors can discern only the boundaries, therefore the centreline was calculated as the mean of the upper and the lower edges coordinates.

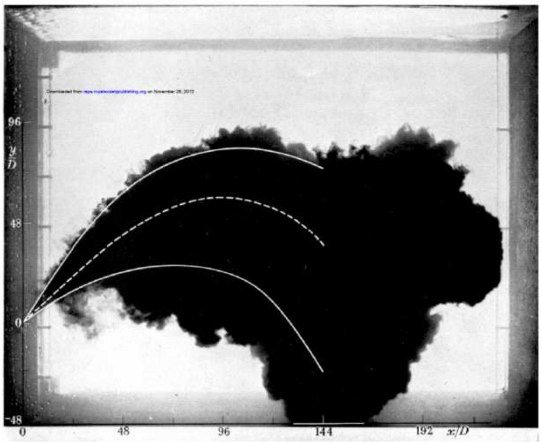

**Figure 2.3 Photograph of a NBJ with inclination of 45°, and $U_0$ = 19 ft/s, the dashed line is the jet axis, the continuous lines the boundary, Bousanquet et al. 1961**

In this work, an integral model for the prediction of the centreline trajectory was also presented. Although their model can predict the horizontal jet with reasonable accuracy, 45° inclined jet prediction is not very accurate.

In a successive paper, Zeitoun et al (1970) measured the axis trajectories and the maximum dilution for 30°, 45°, 60° and 90° inclined jets. Their main outcome is the following: although the non-dimensional maximal height varied with the inclination, the impact point was approximately the same for all inclinations. By plotting the product of these two parameters, the maximum path and consequently the maximum dilution was found for the angle of 60° - considering the same initial flow.

Roberts and Tom (1987) studied the behaviour of jets released upwards, vertically or with an angle of 60° with respect to the horizontal. The release was seeded with rhodamine B and the concentration was determined by fluorometer measurements of vacuum-extracted samples from a vertically arranged rack of sampling tubes. A set of three photographs was taken for each jet, and the authors found the maximum non-dimensional height of the edge and the impact point of the jet. The results were in good agreement with those obtained by Zeitoun et al 1970. However the non-dimensionless minimum dilution and the maximum jet centreline height was different (68% of Zeitoun's values). The authors found that the maximum height of the 60° jet was smaller than the height of the vertical jet, and that the effect of volume flux was not negligible for high density.

Later, Baines et al (1990) found that due to the re-entrainment, an inclined NBJ (with small angle) mixes with its surroundings more rapidly than the vertical one. The largest maximum height was reached for the inclination of 83°. Mixing increases both due to larger penetration (by 17 %) and the entrainment at all elevations is about 40% larger.

On the contrary, Lane-Serff et al (1993) found that for angles between 0° and 75°, the maximum height increases with the angle. The authors conducted NBJs experiments with shadowgraphs images (figure 2.4), a technique similar to LA, in which the shadow in the images represents the two-dimensional projection of the volumetric changes in the investigated area. They determined the maximum height and the vertical concentration profiles with conductivity probes.

**Figure 2.4 Shadowgraph of a NBJ (Lane-Serff1993)**

The authors also developed a practical prediction model to determine the axis trajectories and the concentrations.

Lindberg (1994) conducted shadowgraph experiments of NBJs with inclination of 30°, 45°, 60° and 90° to the horizontal, including also the effects of the cross-flow. The author analyzed the geometrical dimension of the jets and found that the non-dimensional length scales are correlated with the jet and cross-flow Froude number.

Roberts et al. (1997), by using a LIF technique with micro-conductivity probes, studied jets with an angle of 60° at different Froude number (18.7 ÷ 35.7) focusing on the impact point and the bottom layer dilution. The impact point dilution is considerably higher with respect to their previous work (Roberts and Tom, 1987), due, as the authors explain, to the fairly crude sampling method. The authors found 60° to the horizontal as the optimum angle to design brine outfall and to achieve maximum dilution. Also, the authors found the decay of the turbulent fluctuation of the local concentration in the stream-wise direction due to the collapse of the turbulence and the relaminarization of the flow due to the influence of the density stratification.

Donekeret al. (1999) performed experiments with LIF and micro-conductivity probes for inclined dense jets with inclination of 60°. The authors investigated concentration profiles and they found that, due to the interaction of the boundary of the jet with the bottom of the test volume, the dilution at the jet impact point was higher than the one reported in the work of Roberts et al. (1997), because downstream from the impact point, the flow becomes predominantly horizontal with a complex additional mixing process that results in ultimate dilutions considerably higher than the impact dilution. The authors also found normalized expressions and experimental coefficients for dilution, rise height, impact point position etc.

Roberts et al. (1999) argued about the paper of Doneker et al. (1999) that, in Robert et al. (1997), the false floor placed in the channel bypass the problem and also all laboratory experiments are influenced in some way by the experimental configuration.

Bloomfield et al. (2002) focused on the maximum edge heights for jets with inclination between 30° and 90° in a homogeneous and stratified receptor. The authors used shadowgraph technique (figure 2.5) to determine the initial height above the source, the final height of the NBJ and the height at which the mixed fluid finally intrudes where the environment is stratified. They found that the initial NBJ height (the height reached during the first penetration) decreases monotonically as the inclination increases (due to the decrease of vertical momentum).

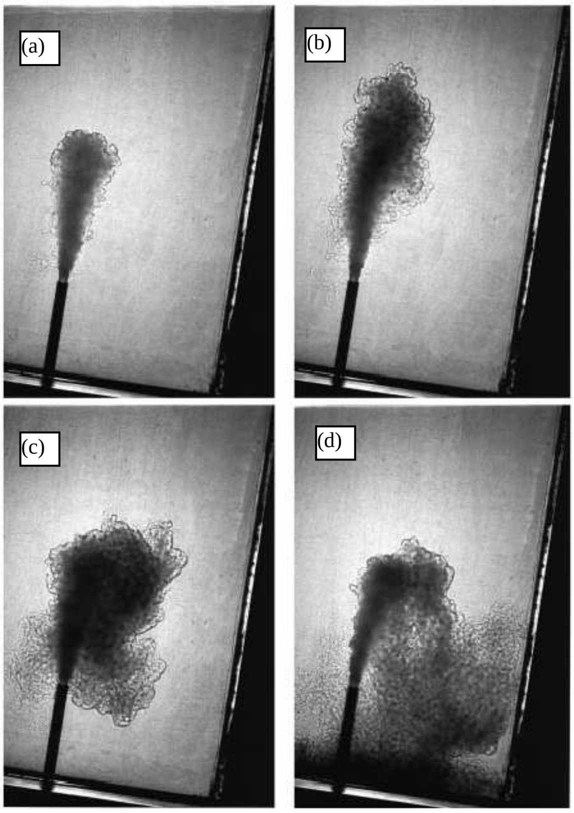


**Figure 2.5 Photographs of Negative buoyant jets formed from a source inclined of 10° to the vertical. The four picture represent 4 different subsequent state of the jet (a) The initial flow is jet-like. (b) The downward buoyancy force brings the fluid to rest at an initial maximum height. (c, d) The fluid then falls as a plume and partially interacts with the upflow, resulting in smaller final height of the fountain. (Bloomfield et al. 2002)**

In contrast, the final NBJ height (the height reached in stationary conditions) was found to increase and then to decrease with the maximum height for an inclination of about 80°. This behaviour is due to the re-entrainment, i.e., to the interaction between the up-flow and the down-flow. The maximum height was found for 80° to the horizontal, whose height is 20% higher than the vertical NBJ.

Law et al. (2004) simulated horizontal buoyant jets varying Reynolds number from 400 to 8000, and obtained a power law to determine the trajectory of the jet.

Cipollina et al. (2005) studied NBJs with inclination of 30°, 45° and 60° to the horizontal axis with different Froude number (30 ÷ 120) and different nozzle diameters. The authors focused on the flow geometrical characteristics of the jet: maximum height, distance from the source and dilution of the impact point. They found that the geometry of the jet is independent of the Reynolds number for moderate viscosity changes.

Kikkert et al. (2006 and 2010) used the experimental set-up shown in figure 2.6to simulate NBJs with Froude number from 14 to 99, different horizontal and vertical inclination of the release (from 0° to 75°), and of the ambient receptor, measuring dilution and trajectories by means of Light Attenuation (LA) and Light induced fluorescence (LIF) techniques. They also developed an analytical solution from an integral model to predict the behaviour of these jets, comparing also the model with experimental results. The analytical solutions gave reasonable predictions of the flow path and the jet height; however the inner spread, the maximum centreline height, the impact point and the minimum integrated dilution were underestimated.

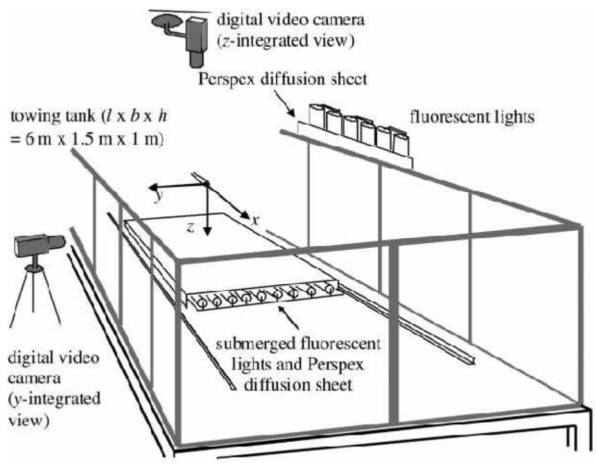


**Figure 2.6 Experimental set-up of Kikkert et al. (2007, 2010)**

In contrast with the previously mentioned authors, who discharged the jet at the end of a pipe, Ferrari and Querzoli (2004, 2010) studied NBJs emitted from a sharp edged orifice, as this kind of release allows a larger entrainment (Mi et al. 2001, 2007). The inclination ranged from 45° to 90° and Froude from 8 to 30.8. The authors studied the characteristic dimensions of the jet axis, the re-entrainment and the distance of Kelvin-Helmholtz instability onset. These works explained that the non-axis-symmetry of NBJs was due to the different stratifications in the upper and lower boundary of a NBJ (see also Ferrari and Querzoli, 2011). Moreover, they showed that the maximum height of the jet axis increases from 45° to approximately 80° in agreement with the results of Bloomfield and Kerr (2002), and then decreases because of the re-entrainment phenomenon. They demonstrated that the impact distance and the maximum jet height depend linearly on the horizontal momentum component, without any dependence on the re-entrainment. Also, they observed that the maximum height for angles larger than 80° is reduced by the re-entrainment.

Papakostantis et al. (2011a, 2011b) simulated NBJs with inclination from 45° to 90°, Froude number from 7 to 60 and three different diameters of the nozzle (0.6, 0.8, 1 cm). The experiments were carried out in a large tank to eliminate the possible effects of the boundary (figure 2.7). The release was a salt-water solution coloured with red food dye.

The authors, using micro scale conductivity probes and image analysis, identified the geometrical characteristic of the jets and the turbulent concentration distribution and fluctuation.

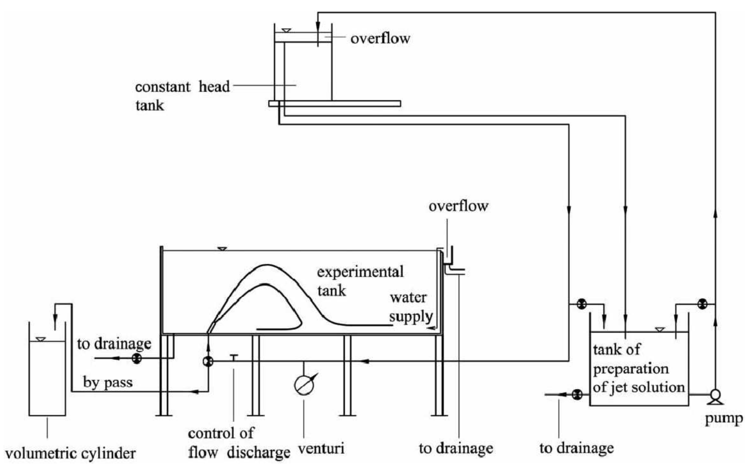


**Figure 2.7 Experimental set-up used by Papakostantis et al. 2011**

They concluded that the dimensionless initial terminal rise height increases monotonically with the discharge angle and reaches its maximum for vertical discharge. The dimensionless final terminal rise height increases as the discharge angle increases up to 80° where it reaches its maximum value and then decreases. The ratio between the initial terminal rise height and final terminal rise height is approximately 1.16, and it is independent of the discharge angle. The dimensionless horizontal distance from the source at which the terminal height of rise appears, as well as the horizontal distance where the upper jet boundary crosses the source elevation, decreases as the discharge angle increases. They found also that the concentration and concentration turbulent intensity on the jet axis plane at the horizontal location of the terminal rise height are self-similar for large Froude numbers, for all discharge angles considered. The vertical mean concentration distribution, at the location of the terminal height of rise, is approximately Gaussian in the upper jet boundary, but deviates considerably in the lower boundary due to the detachment of dense fluid. They found also that the dilution rate, normalized by the densimetric Froude number, does not depend on the discharge angles.

### 2.2.4 Velocity measurements in inclined buoyant jets

The works exposed in the previous paragraphs were generally performed by using optical techniques, such as LA or LIF; as a consequence, only the concentration fields and related quantities were measured; only very few investigations were conducted using Particles Image Velocimetry (PIV) or Particle Tracking Velocimetry (PTV) techniques to study the velocity fields.

Cenedese et al. (2005) used both LIF and PTV techniques to study velocity and concentration profiles at different Froude numbers for horizontally released laminar jets. The experimental set-up was a glass tank 0.80m high, 0.80 m wide and 1.32 m long. The jet was discharged from a smooth pipe of 0.012 m in diameter (figure 2.8).The authors investigated the structures inside the jet under laminar conditions.

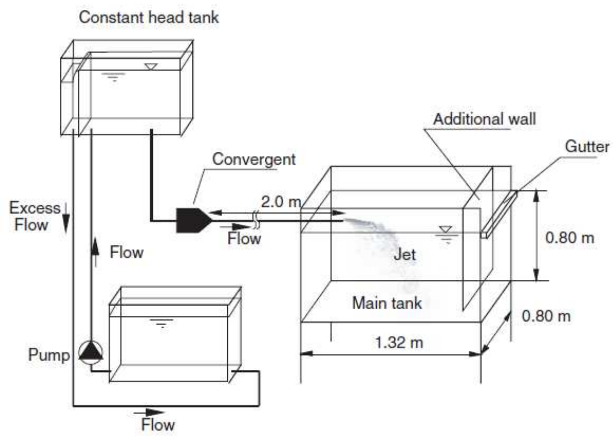


**Figure 2.8 Experimental Set-Up used by Cenedese et al. 2005**

Shao and Law (2010) focused on small angles (30° and 45°) in a steady ambient. They used combined PIV and LIF, and studied the Coanda effect due to the proximity of the seabed. The experimental set-up is a glass tank 285 cm long, 85 cm wide and 100 cm dept. The discharge was at the end of a Perspex tube of 5.8 mm (figure 2.9).

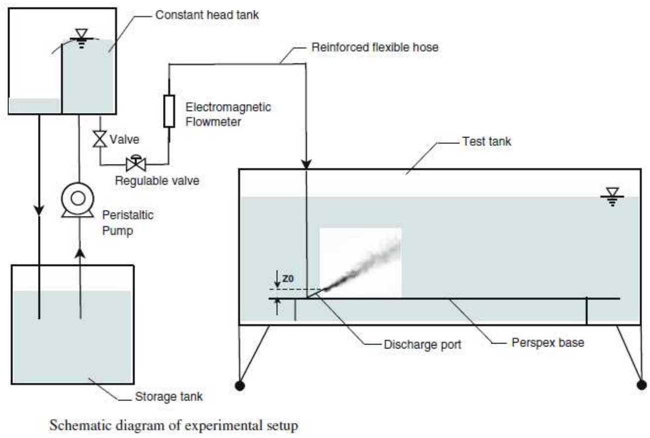


**Figure 2.9 Experimental Set-up of Shao - Law 2010**

In this work, the centreline trajectories, the normalized dilutions, and the coefficients of the non-dimensional equations for the determination of the geometrical characteristics of the jet were shown. The authors also obtained a relation for the prediction of the velocity decay (figure 2.10).

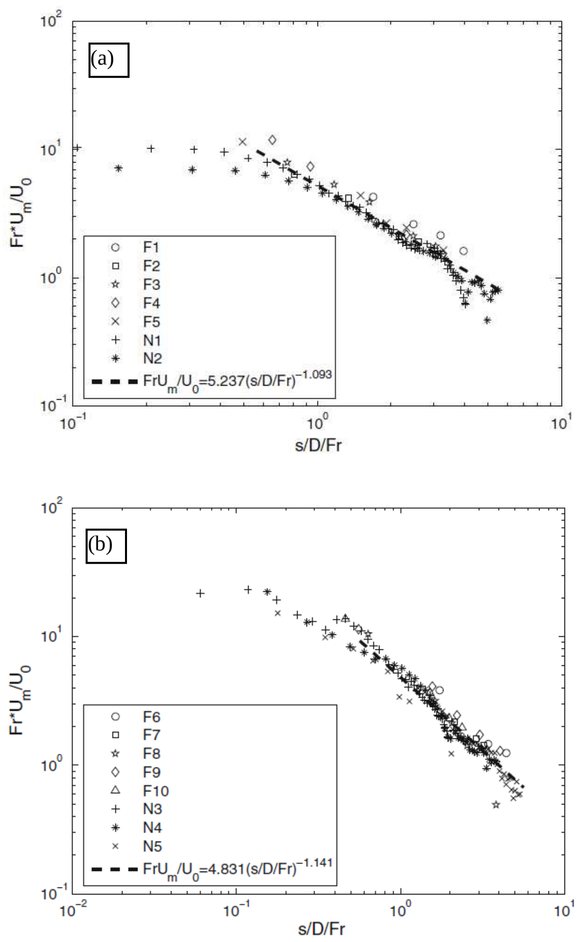


**Figure 2.10Comparison of non-dimensionalized centreline maximum velocity magnitude decay (log-log scale) (a) 30°, (b) 45°,Fr is the Froude number, $U_m$ is the maximum velocity, $U_0$ the maximum exit velocity(Shao and Law 2010).**

See the table 2.1 for the test cases related to the figure (2.10).

**Table 2.1**

| Exp. no. | Inclined angle $\theta$ | Nozzle diameter D (mm) | Distance $z_0$ (mm) | $\Delta\rho/\rho_a$ (%) | Discharge velocity $U_0$ (m/s) | Reynolds number $Re$ | Densimetric Froude number $Fr$ |
|---|---|---|---|---|---|---|---|
| F1 | 30° | 5.80 | 24.00 | 0.995 | 0.238 | 1390 | 10.0 |
| F2 | 30° | 5.80 | 24.00 | 0.995 | 0.356 | 2074 | 15.0 |
| F3 | 30° | 5.80 | 24.00 | 0.995 | 0.503 | 2934 | 21.1 |
| F4 | 30° | 5.80 | 24.00 | 0.995 | 0.602 | 3508 | 25.3 |
| F5 | 30° | 5.80 | 24.00 | 0.995 | 0.727 | 4236 | 30.6 |
| F6 | 45° | 5.80 | 24.00 | 0.995 | 0.238 | 1390 | 10.0 |
| F7 | 45° | 5.80 | 24.00 | 0.995 | 0.356 | 2074 | 15.0 |
| F8 | 45° | 5.80 | 24.00 | 0.995 | 0.507 | 2956 | 21.3 |
| F9 | 45° | 5.80 | 24.00 | 0.995 | 0.606 | 3530 | 25.5 |
| F10 | 45° | 5.80 | 24.00 | 0.995 | 0.765 | 4456 | 32.2 |
| N1 | 30° | 10.75 | 11.17 | 1.984 | 0.507 | 5478 | 11.0 |
| N2 | 30° | 10.75 | 11.17 | 1.984 | 0.338 | 3652 | 7.4 |
| N3 | 45° | 10.75 | 12.92 | 1.984 | 1.173 | 12672 | 25.5 |
| N4 | 45° | 10.75 | 12.92 | 1.984 | 0.586 | 6336 | 12.8 |
| N5 | 45° | 10.75 | 12.92 | 1.984 | 0.391 | 4224 | 8.5 |

Shao and Law (2011) studied horizontal dense jets with Froude from 7.7 to 16.2 varying the discharge velocity. They used PIV – PLIF techniques and focused on the influence of the bottom attachment. The authors found that the concentration and velocity axis initially coincide, but they begin to deviate from each other when the edges of the jet impinges with the bottom; and in particular the concentration axis then descends to the wall due to the no-flux boundary condition (impermeable boundary, and consequently no concentration gradients), while the maximum velocity is higher due to the no-slip condition (velocity equal to zero at the boundary).

Another paper was by Lai and Lee (2012): the release angles were between 15° and 60° and Froude number between 10 and 40.The authors compared their results with the two previous work by Shao and Law (2010, 2011), and with the predictions of the VISJET model (Lee and Chu 2003) for inclinations of 30° and 45°. The experiments were carried out in a flume 1.2 m wide and 11 m long. The nozzle was tapered with internal diameter that varies from 30 mm to 5 mm. The head nozzle is mounted onto a false floor. To avoid jet attachment with the floor, the release is fixed at 5 cm. The distance between the camera and the test section is 3.5 m to minimize the effect of the parallax (figure 2.11).

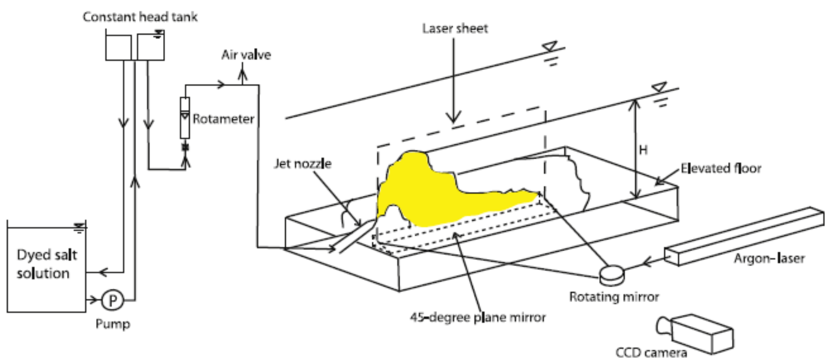


Experimental setup for inclined dense jets in stagnant ambient.

**Figure 2.11 Experimental Set-Up used by Lai and Lee (2012)**

In this paper, the geometrical characteristics of the jet and the concentration profiles normalized to the initial source concentration (determined using a calibration box, filled with the source fluid placed at the measurement section and illuminated with the same laser sheet) were obtained. The authors observed that the concentration profiles were Gaussian up to s/D = 20 (s is the stream-wise coordinate and D the diameter of the nozzle). Studying the velocity fields, the authors found that the effects of the negative buoyancy are not significant in the decay of the stream-wise velocity.

## 2.3 - Numerical models

### 2.3.1. Integral jet models

Several numerical models have been proposed, the most commonly adopted method is the jet integral model developed by Fan et al. (1969) and adopted for positively buoyant jets. They analyzed unstratified and stratified environments, and assumed that the profiles of velocity, density and tracer concentration were self-similar and Gaussian. The following section gives a review on integral approach on negatively buoyant jets.

Abraham (1967) developed a model for negatively buoyant jets into stationary ambient, issued horizontally or vertically. The assumptions made were self-similarity and Gaussian profiles on momentum and mass profiles, but the transition between positive and negative entrainment was also included.

Wang et al. (2002) have proposed second-order integral models only for positively buoyant jets, which take the turbulent mass and momentum fluxes into account. The model employs the entrainment assumption with the entrainment coefficient and the variation of turbulent mass flux modelled as a function of the local Richardson number. Instead, the turbulent momentum flux treated as a percentage of the local mean momentum flux. The model also assumes a constant concentration-to-velocity width ratio, in which the ratio is expressed as a function of the local Richardson number. The model can predict positively buoyant jets quite well, however dense jets were not simulated.

Jirka (2004) proposed a model to simulate buoyant jets released at different angles in stagnant or flowing current conditions. The integral model for the flux conservation of mass, momentum, buoyancy and scalar quantities uses an entrainment closure approach that separates the transverse shear contribute and azimuthally shear mechanism. It defines these flux quantities based on Gaussian profiles for the transverse distribution of velocity and scalars. The model contains also a quadratic law turbulent drag force mechanism. The initial zone of flow establishment is specified with explicit account for the effects of discharge buoyancy and of cross-flow on this region.

Kikkert et al. (2007) developed an analytical solution for arbitrary inclined negatively buoyant jets into stationary water. The model does not solve the typical equations of the common integral model, but is a semi-empirical analytical model, based on kinematic consideration, i.e. a pure jet is assumed before the terminal rise. The model has several limitations in the prediction of the minimum impact point dilution.

Papanicolau et al. (2008) proposed two integral models to simulate buoyant jets issued into calm, homogeneous or density stratified environment. The applied assumptions are the “top-hat” formulation, and Gaussian cross-sectional distribution. The formula of Priestley et al. (1955) was used to model the variation of the entrainment coefficient. The authors, comparing the model with their experimental results, found that the entrainment coefficient must be reduced from 0.057 to 0.03 ÷ 0.04; which corresponds to a reduction of the shear entrainment and consequently an increase of the maximum height. The result is valuable, because previous models underestimated this quantity. They also found that a better prediction could be achieved using the top-hat formulation.

Jirka (2008) used the Corjet model (Jirka, 2004) at different discharge angles (from 0° to 90° to the horizontal), and different offshore bathymetry. The author found the largest offshore impingement location from 30° to 45°. The optimal inclination to achieve the maximum dilution at the maximum rise level was reached for an inclination of 45°, but with small difference from 30° to 60°. Instead, the maximum dilution in the impingement point was found for a flat bottom, for discharge inclination from 60° to 75°, for moderate slope of the bottom (10 - 20°) at about 45-60°, for strong slope (30°) at about 30 - 45°. Comparing these results with previous experimental works, the author found that the geometrical characteristics of the jets simulated with his model were in agreement with the previous experimental works. On the contrary, the dilution levels on the impact point and on the maximum rise level showed more disagreement.

### 2.3.2. Simulation of NBJs with generic Computational Fluid Dynamics algorithms

Another approach for the numerical prediction of the behaviour on NBJs is to solve directly the Navier-Stokes equations under different assumptions using Computational Fluid Dynamics (CFD) solvers. There are several CFD techniques, for example direct numerical simulation (DNS), where Navier-Stokes equations are solved at scales small enough to solve the entire turbulence spectrum form the largest eddies to the Kolmogorov scale. Another approach is Large Eddy Simulation, the Navier - Stokes equations are solved to solve motion bigger than the grid size, smaller scales are modelled with sub-grid models. The most common models are the so-called Reynolds Averaged Navier - Stokes models (RANS), in which the time averaged formulations of the Navier-Stokes equations are solved. Assumptions are made about the new terms that arise from this time averaging.

There has not been application of CFD simulations of buoyant jets. In a stagnant ambient, vertical buoyant jets have been performed by several authors, e.g., Hwang and Chiang (1995) and Hwang et al. (1995) that simulated the initial mixing in a density stratified cross flow using a RANS model with a buoyancy modified $\kappa$-$\varepsilon$ model.

Blumberg et al. (1996) used far field CFD circulation model of Massachusetts Bay to calculate near field dilution levels. The results have been compared with similar predictions from near field plume model (ULINE). The comparison indicates that the trap heights and initial dilutions obtained with the far field model were in agreement with those generated by the near field model.

Lin and Armfield (2000) studied the behaviour of weak axisymmetric vertical fountains with a time-accurate finite volume code. They found that the relation between the Froude number and the maximum height is a linear function and that the time scale for the development of the fountain flow is a quadratic function of the Froude number.

Law et al (2002) used a RANS model with $\kappa$-$\varepsilon$ turbulence closure to investigate the dilution of an 8 port rosette-shaped diffuser.

Vafaiadou et al (2005) used the software package ANSYS CFX[1]to simulate NBJs with inclinations between 45° and 90°. They compared their results with those obtained by Roberts et al. (1997) and Bloomfeld and Kerr (2002). The model adopted was the Shear Stress Transport (SST) turbulence model, developed by Menter (1994) to effectively blend the robust and accurate formulation of the $\kappa-\omega$ model in the near-wall region with the free-stream independence of the $\kappa-\varepsilon$ model in the far field. By comparing the results with available experimental data, they found that the initial height of rise of a negatively buoyant jet at the initiation of flow is always larger than the terminal height of rise. The computed difference was around 20%. Also the initial and final height of rise obtained by the numerical model is in satisfactory agreement with the results of Bloomfield and Kerr (2002) for the range of angles between 0° and 45° to the vertical. Finally, the numerical results underestimated slightly the height of rise obtained by Roberts et al. (1997) for an angle of 30° to the vertical. According to the authors, the model can be considered as a valuable tool for the simulation of NBJs.

[1]http://www.ansys.com/Products/Simulation+Technology/Fluid+Dynamics/Fluid+Dynamics+Products/ANSYS+CFX

Plumb (2008) simulated a submerged single port jet (figure 2.12) with the software package ANSYS FLUENT[2] using several turbulence models. The grid was built with GAMBIT, and the refinement was necessary in the hypothetical path of the jet (figure 2.13). Comparing his results with experimental data, he found a similar shape but different dilution levels.

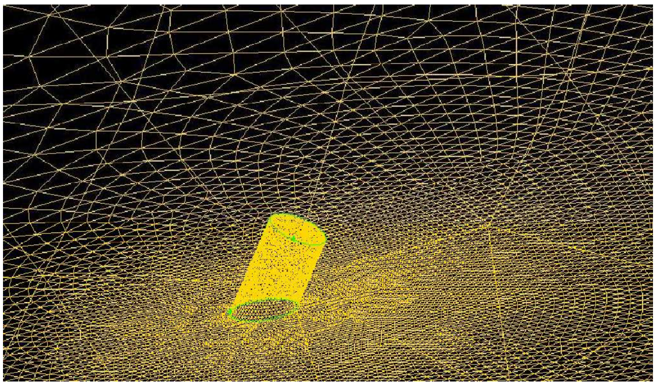

**Figure 2.12Diffuser port geometry (Plumb 2008)**

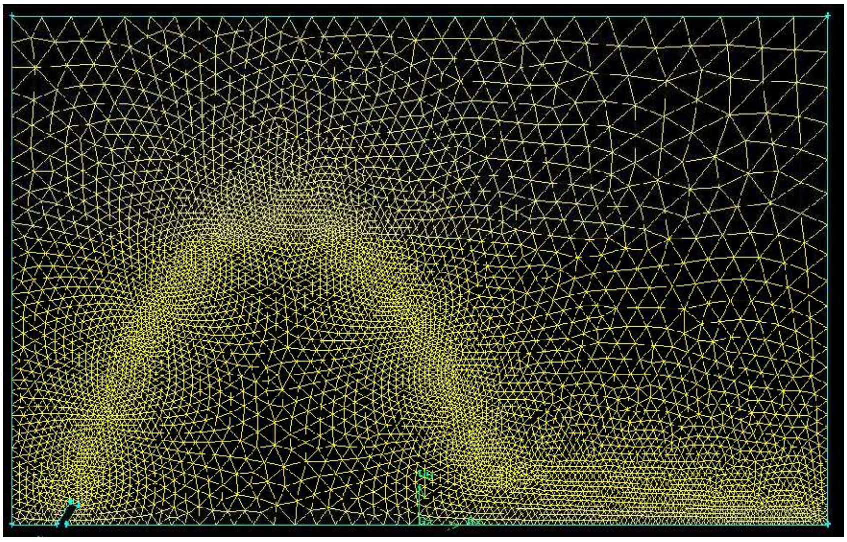

**Figure 2.13 2D Grid with refinement (Plumb 2008)**

Tang et al. (2008) developed a three-dimensional Reynolds-averaged Navier-Stokes computational fluid dynamics model with embedded grids to model accurately the geometry of the diffusers. The authors used an algebraic mixing length model with a Richardson - number correction is used for the turbulence closure. The governing equations were solved with a second-order-accurate, finite-volume, artificial compressibility method. They applied the model to simulate negatively buoyant wall jet flows and the computed results were shown to be in good overall agreement with the experimental measurements. Also, the comparisons with results obtained by applying two empirical mixing

[2]http://www.ansys.com/Products/Simulation+Technology/Fluid+Dynamics/Fluid+Dynamics+Products/ANSYS+Fluent

zone models showed that the results were similar in terms of rate of dilution and geometrical characteristics.

Oliver et al (2008 and 2012) used a k-e model of the software package ANSYS CFX to simulate NBJs. The authors took two models, the first using an essentially standard form to predict the flow behaviour, the second to calibrate the model with respect to the experimental analysis. Comparing the results with experimental data, the predictions from both the simulations were comparable for the trajectory but the integrated dilution predictions at the centreline maximum height were conservative (mean-integrated concentrations are over-predicted).

Mier – Torrecilla et al. (2010) developed a numerical scheme for the simulation of multi-fluid flows with a particle finite element method (PFEM), which can model immiscible fluids. In a successive paper (Mier – Torrecilla et al. 2012), they applied the scheme to study negatively buoyant jets in a homogeneous immiscible ambient fluid, solving the 2D Navier–Stokes equations for vertical jets. The authors focused on the jet height and its variation in time, varying Reynolds and Froude number.

They found three different regimes (figure 2.12), the first characterized by being very stable, with an approximately constant height, the second described as a pulsating fountain in which the height oscillates in time. The third type, observable at higher injection velocities, in which the jet initially penetrates upward and, when it reaches the maximum height, forms a cap on the top.

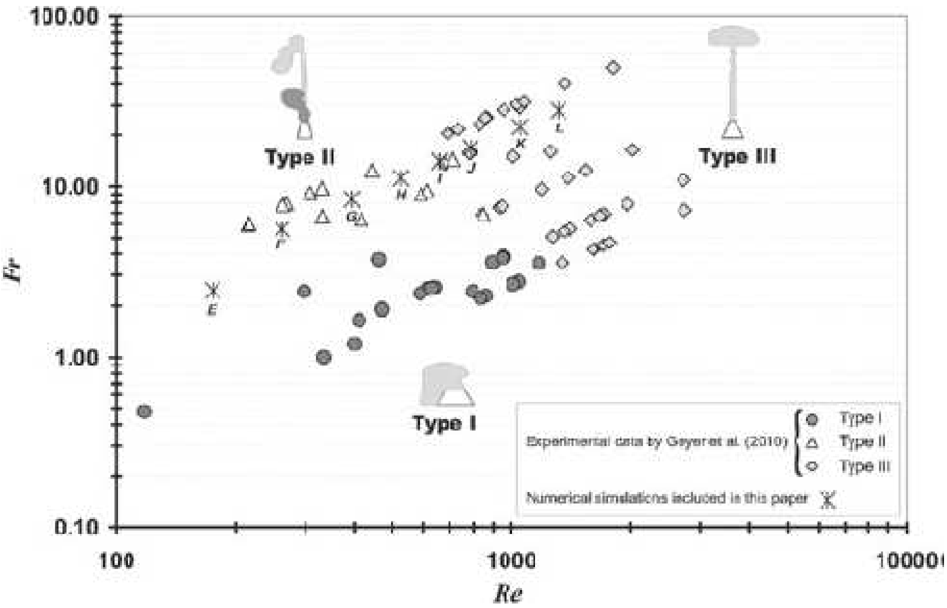


Figure 2.12Behaviour of the jets, in terms of the Froude number and the Reynolds number

Seil and Zhang (2010) modelled single and multi-port diffusers using ANSYS FLUENT, and also they compared their results with those of Roberts et al. (1997) and Nemlioglu et al. (2006). The jets were found to be conservative near the orifice, till a, dimensionless with the Froude number, distance of 7 diameter. For the multi-port configuration, they presented qualitative images. The important result is that: “impact dilutions from the individual jets were in both cases found to be less than for the equivalent single plume”.

### 2.3.3. Commercial tools dedicated to buoyant jets

Extensive papers about commercial models for the simulation of brine discharge have been presented by Palomar et al. (2012a and 2012b) and Roberts et al. (2010). According to the authors, the most important tools for the simulation of the near field region in buoyant jets are “CORMIX”, “VISJET”, and “VISUAL PLUMES”.

CORMIX (Cornell Mixing Zone Expert System) software was developed in the 1980s at Cornell University under the support of the EPA (Environmental Protection Agency), and can simulate positive, neutral and negative buoyant jets. In this software, there are several subsystems, CORMIX 1 and 2 are based on dimensional analysis and can simulate single-port (CORMIX 1) and multi-port jets (CORMIX 2) using semi-empirical formulas to calculate the main features of single port discharge, and, CORJET based on the integral differential equations. CORJET is an Eulerian model, so the typical assumptions are self-similarity and Gaussian profiles; the motion and differential equations in the axisymmetric coordinate system through the cross section are solved by using a Runge-Kutta 4th order numerical method. The assumptions are unlimited environment, self-similarity of the cross sectional profiles and stationary state. The entrainment model is based on the Priestly et al. (1955) formula for round vertical jets, adding a term to take into account the inclination. The model is strictly valid only for the asymptotic self-similar regimes (pure jet, pure plume, pure wake, advected puff, advected thermal), while in the intermediate cases an approximation is used.

VISUAL PLUMES (VP) was developed by the Environment Protection Agency (EPA), and can simulate positively, negatively and neutrally buoyant jets with single or multi-port diffuser. The model considers the effluent properties (total flow rate, effluent salinity, temperature or density, effluent pollutant concentration), the discharge configuration (number of port, diameter, depth, port orientation) and the ambient condition (flowing or stratified water, current speed and direction, salinity and temperature, background pollutant concentration, diffusion coefficient, decay rate). VP has several independent models:

- UM3 a Lagrangian model for single and merging plume
- DKHW, an Eulerian model for single and merging plume

- NRFIELD, a semi-empirical model for multiport diffusers

- PDSW, an Eulerian model for surface discharges

The differential equations are solved using a Runge-Kutta 4th order method. The assumptions are unlimited environment, self-similarity of the cross sectional profiles, stationary state, top-hat jet profiles. The mass into the plume in the presence of current is quantified using the generalized 3D projected area entrainment (PAE) hypothesis(Frick 1984), this assumes that entrainment due to the cross-flow (the vortex pair entrainment in the far field) is equal to the ambient flow intercepted by the "windward" face of the plume element.

Generally in the Lagrangian models, the basic assumption are different, instead of using the Eulerian equations, the marked material volume (with an initial mass, momentum and buoyancy) issued from the source is followed with time, and it mixes itself with the surrounding fluid due to the turbulent entrainment, and in so doing, it changes its width, mass, momentum and concentration.

VISJET (Innovative Modelling and Visualization Technology for environmental Impact Assessment) is a model developed at the University of Hong Kong and can simulate negatively and positively buoyant jets with single or multi-port diffuser, and like VISUAL PLUME, considers the effluent properties, the discharge configuration and the ambient condition. At difference with the previous two software, VISJET is a Lagrangian Model; the assumptions are unlimited environment, self-similarity of the cross sectional profiles, stationary state, top-hat jet profiles. The unknown jet trajectory is modelled as a sequence of plume elements, following the jet path, increasing the mass as a results of the shear entrainment (due to the jet discharge) and vortex entrainments (due to the cross-flow, if presents). The entrainment in a cross-flow is determined by the PAE hypothesis that includes terms to take into account the effect of excess velocity of the jet, and the presence of a cross ambient current.

According to Palomar et al. (2012b), the three previous models tend to underestimate the jet dimensions. The Terminal rise height deviations ($Z_t$) are between 10% and 30% and this deviation increases according to the initial discharge angle. Also, they significantly underestimate the dilution at the impact point ($S_i$). See table 2.2, for the results of complete set of cases under validation.

**Table 2.2 Estimated errors in commercial Tools (Palomar et al. 2012 b)**

| ESTIMATED ERRORS MADE BY COMMERCIAL TOOLS WHEN MODELING BRINE DISCHARGES (↓: underestimation; ↑: overestimation) | | | | | | | | | | |
|---|---|---|---|---|---|---|---|---|---|---|
| STAGNANT AMBIENT | Variable | $\theta = 30°$ inclined jet | | | $\theta = 45°$ inclined jet | | | $\theta = 60°$ inclined jet | | |
| | | Corjet | UM3 | JetLag | Corjet | UM3 | JetLag | Corjet | UM3 | JetLag |
| | $Z_t$ | ~10%↓ | ~25%↓ | 0% | ~10%↓ | ~20%↓ | ~20%↓ | ~15%↓ | ~30%↓ | ~25%↓ |
| | $S_i$ | ~60%↓ | | | ~60%↓ | ~60%↓ | ~50%↓ | ~60%↓ | ~65%↓ | ~55%↓ |
| | $X_r$ | ~15%↓ | ~25%↓ | ~15%↓ | ~10%↓ | ~25%↓ | ~10%↓ | ~15%↓ | ~25%↓ | ~10%↓ |
| | All variables are underestimated by the commercial models, especially dilution rates. | | | | | | | | | |
| DYNAMIC AMBIENT 60° inclined jet | Variable | Coflowing case $\theta = 60°, \phi = 180°$ | | | Counter-flowing case $\theta = 60°, \phi = 0°$ | | | Transverse current case $\theta = 60°, \phi = 90°$ | | |
| | | Corjet | UM3 | JetLag | Corjet | UM3 | JetLag | Corjet | UM3 | JetLag |
| | $Z_t$ | ~25%↓ | ~30%↓ | ~30%↓ | ~10%↑ to ~5%↓ | ~5%↓ to ~15%↓ | ~5%↓ to ~20%↓ | ~30%↓ | ~40%↓ | ~40%↓ |
| | $S_i$ | ~15%↓ to ~5%↑ | ~35%↓ | ~30%↓ to ~15%↑ | ~5%↓ to ~65%↑ | ~20%↓ to ~5%↑ | ~5%↓ to ~90%↑ | ~25%↓ to ~25%↑ | ~15%↓ to ~2%↓ | ~20%↓ to ~45%↑ |
| | For values $U_r F_{rd} > 0.75$, commercial models tend to overestimate variables, especially dilution at the impact point and jets opposing the crossflow. | | | | | | | | | |

# Chapter 3

# Theoretical analysis of buoyant jets

## 3.1 - Introduction

As stated by Fisher et al. (1979): "*A jet is the discharge of fluid from an orifice or a slot into a large body of the same or similar fluid. A plume is a flow that looks like a jet, but is caused by a potential energy source that provides the fluid with positive or negative buoyancy relative to its surroundings*."

A buoyant jet is an intermediate flow between a jet and a plume, on which both the buoyancy and the momentum are present. In particular, the initial part of the flow is driven mostly by the momentum, while later mostly by the buoyancy forces.

The behaviour of jets and plumes depends on three classes of parameters:

**Jet parameters**

Initial velocity distribution, turbulence level, the jet mass flux, the jet momentum flux and the flux of the contaminant (such as heat, salinity, etc...)

**Environmental parameters**

The environmental parameters are all the ambient factors which influence the jet at a certain distance from the nozzle, like currents, density stratifications, etc.

**Geometrical factors**

These factors are: the shape and the size of the nozzle, the orientation and the influence of other jets, solid obstacles, or the free surface.

In this chapter, the limiting asymptotic solutions for simple flows (jets and plumes) are shown, and then these solutions are combined to deduce the behaviour of more complex flows, such as buoyant jets, and the qualitative influence of buoyancy, momentum, etc.

## 3.2 – Jets and Plumes

In a jet (or plume), near the nozzle, the flow is controlled entirely by the initial conditions (geometry of the nozzle, mean velocity, difference between the density of the discharge and the one of the ambient fluid).

A general description of the factors important to jet dynamics can be defined by:

1) The mass flux of the jet ($\rho\mu$) is the mass of fluid passing through a jet cross-section per unit time. The mass flux is given by:

$$\rho\mu = \int_A \rho w dA \,, \tag{3.1}$$

- $A$ is the cross-sectional area of the jet
- $w$ is the mean velocity in the axial direction
- $\mu$ is the specific mass flux of the jet

2) The momentum flux of the jet ($\rho m$) is the amount of stream-wise momentum passing a jet cross section per unit time. It is given by:

$$\rho m = \int_A \rho w^2 dA \,, \tag{3.2}$$

- m is the specific momentum flux

3) The buoyancy flux ($\rho\beta$) is the buoyant or submerged weight of the fluid passing through a cross section per unit time. It is given by:

$$\rho\beta = \int_A g\Delta\rho w dA = \int_A \rho g' w dA \tag{3.3}$$

- $\Delta\rho$ is the difference in density between the ambient fluid and the jet fluid
- β is the specific buoyancy flux
- $g' = g\dfrac{\Delta\rho}{\rho}$ is the effective gravitational acceleration

Referring to the initial values i.e. volume flux (Q), specific momentums flux (M) and specific buoyancy fluxes (B) for a circular buoyant jet, these quantities are given by:

$$Q = \frac{1}{4}\pi D^2 W \,, \tag{3.4}$$

$$M = \frac{1}{4}\pi D^2 W^2 \,, \tag{3.5}$$

$$B = g\frac{\Delta\rho_0}{\rho}Q = g'_0 Q \,, \tag{3.6}$$

where D is the jet diameter and W denotes the mean outflow velocity assumed uniform across the jet; $\Delta\rho_0$ indicates the difference in density between the fluid discharged and the surrounding fluid, and $g'_0 = \frac{\Delta\rho_0}{\rho}$.

### 3.2.1. Simple Jet

In simple jets, the time-averaged concentration C across the jet shows essentially a Gaussian distribution of tracer concentration, which may be defined as:

$$C = C_m \cdot \exp\left[-k\left(\frac{r}{x}\right)^2\right], \tag{3.7}$$

where $C_m$ is the value of concentration along the jet axis, x indicates the distance along the jet axis, r denotes the radial distance from the jet axis and k is a constant.

The Gaussian distribution is verified also for the time-averaged velocity profile. This Gaussian shape is present only after six jet diameters downstream the nozzle. In the region from the jet orifice to six diameters downstream, the shear layer is still being established at the expense of the velocity core of the jet flow, as it exits the nozzle; for this reason, the latter region is named the zone of flow establishment (ZFE).

The flow downstream of the ZFE, in which the jet continues to expand and the mean velocities and tracer concentration decreases, is called zone of established flow (ZEF). In this zone, the profiles are “self-similar”, i.e.at any cross section, it is possible to express any time-averaged concentration and velocity profile in terms of a maximum value and a measure of the width.

In the ZFE, the flow forms a transition between the wall shear controlled flow and the free-shear region. In the ZFE, the core flow is essentially irrotational and is not affected by the jet diffusion. The second region (ZEF) is downstream the ZFE, where the entrainment with the ambient fluid begins, and the jet continues to expand.

As shown by Lee et al. (2003) (see also figure 3.1), for a round jet, the expression of the profiles in the zone of flow establishment is:

$$\begin{aligned} u &= u_0 && r \le R \\ u &= u_0 \cdot \exp\left[-\frac{(r-R)^2}{b^2}\right] && r > R \end{aligned} \tag{3.8}$$

$$\begin{aligned} c &= c_0 && r \le R \\ c &= c_0 \cdot \exp\left[-\frac{(r-R)^2}{(\lambda \cdot b)^2}\right] && r > R \end{aligned} \tag{3.9}$$

where $r$ is the half width of the potential core, $b$ indicates the width of the mixing layer. $\lambda$ denotes a parameter introduced to take the difference between the diffusion of mass and that of momentum into account, and R is the thickness of the velocity core.

In the ZEF, for $x > 6.2\ D$, the profiles can be expressed as:

$$u = u_m \cdot f\left(\frac{r}{b}\right) = u_m \cdot \exp\left[-\frac{r^2}{b_u^{\ 2}}\right] \quad , \tag{3.10}$$

$$c = c_m \cdot \exp\left[-\frac{r^2}{(\lambda \cdot b)^2}\right] \quad , \tag{3.11}$$

where $u_m$ and $c_m$ are the maximum velocity and concentration along the centreline. function $f$ is usually of Gaussian form.

The width of the jet $b$ is defined as the lateral location where the velocity is equal to 1/e of the centreline value.

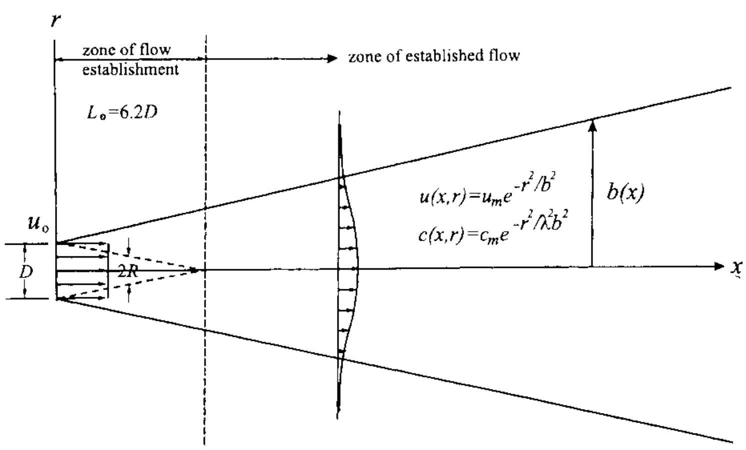


**Figure 3.1 Round turbulent jet showing the Zone of Flow Establishment (ZFE) and Zone of Established Flow (ZEF) (Lee and Chu 2003)**

For a simple turbulent round jet, we can define a characteristic length scale:

$$l_Q = \frac{Q}{M^{1/2}} = \sqrt{A} = \left(\frac{\pi}{4}\right)^{0.5} \cdot D \quad , \tag{3.12}$$

where $A$ is the initial cross sectional area of the jet. This represents the distance downstream from the jet orifice in which all the properties of the jet will be function of $x/l_Q$, Q and M.

Considering this argument, we can deduce how $u_m$, $c_m$, $b$, $\mu$, and $m$ must depend on the distance from the jet orifice. For example, since $u_m$ has the dimensions length/time, we must have that

$$u_m \frac{Q}{M} = f\left(\frac{x}{l_Q}\right) \tag{3.13}$$

- For $x \to 0$, $u_m \to M/Q$
- Considering $x/l_Q >> 1$, this limit is formally equivalent to:

  - $x \to \infty$, with Q and M fixed
  - $Q \to 0$, with z and M fixed
  - $M \to \infty$, with z and Q fixed

From the previous equivalences, it is possible to note that further from the jet orifice, the volume flow becomes less important and on the contrary, the momentum flux increases its importance. Therefore, for x $>>l_Q$, all properties of the jet are defined solely in terms of x and M. This result indicates that it is possible to define the velocity on the jet centreline as the product of a constant$a_1$ times the ratio between the length scale $l_Q$ and the stream-wise coordinate $x$:

$$u_m \frac{Q}{M} \to a_1 \frac{l_Q}{x} \quad . \tag{3.14}$$

Also $b$ can be specified by a function of the form:

$$\frac{b}{l_Q} = f\left(\frac{x}{l_Q}\right) \quad . \tag{3.15}$$

### 3.2.2. Simple Plume

In the simple plume, there is no initial volume or momentum flux, therefore the flux is only function of the buoyancy flux B, the distance from the origin z, and the viscosity of the fluid $\upsilon$.

The time – averaged vertical velocity on the axis of the plume is given by:

$$u_m = f(B, x, \upsilon) \quad . \tag{3.16}$$

Since there are only four variables, it is possible to define two dimensionless groups. Therefore, assuming a point source one obtains for a round plume:

$$u_m \left( \frac{x}{B} \right)^{1/3} = f\left( \frac{B^{1/3} \cdot x^{2/3}}{\upsilon} \right) \quad . \tag{3.17}$$

The term on the right hand side is similar to the Reynolds number, i.e. when it is sufficiently large ($x >> \upsilon^{3/2}/B^{1/2}$), the flow is fully turbulent and the effect of the viscosity is negligible. In this case we get:

$$u_m = b_1 \left( \frac{B}{z} \right)^{1/3} \quad . \tag{3.18}$$

In the plumes, that term changes the momentum of the flow, and increases along the axis of the plume (in contrast to the jet). The momentum flux depends only on *B* and *x*.

Using dimensional analysis we get

$$m = b_2 \frac{B^{2/3}}{x^{4/3}} \quad . \tag{3.19}$$

Similarly, the volume flux in a round plume is given by

$$\mu = b_3 \frac{B^{1/3}}{x^{5/3}} \quad , \tag{3.20}$$

where $b_1$, $b_2$ and $b_3$ are constant to be determined experimentally.

### 3.2.3. Buoyant Jets

A buoyant jet is a jet governed at the same time by the difference of density between the fluid discharged and that of surrounding, and by the momentum fluxes. In particular, near the nozzle, the flow is governed only by the momentum fluxes and it behaves like a simple jet. Instead, at far away, it is governed solely by the buoyancy, and it behaves like a plume. In between the behaviour is intermediate. The density difference may be positive or negative, therefore it is important to analyse the orientation of the jet with respect to the vertical axis.

In this paragraph we consider a jet, which is discharged vertically upwards. Its density is smaller than the one of its surroundings, therefore it travels upwards.

The parameters which determine the flow are the initial fluxes of volume (*Q*), momentum (*M*) and buoyancy (*B*) furthermore the distance from the source point.

Froude number is one of the most important dimensionless parameters used to characterise buoyant jets:

$$Fr = \frac{w}{(g' \cdot D)^{1/2}} \quad . \tag{3.21}$$

The Froude number compares buoyancy and inertial forces of buoyant jets.

For a round jet, we can define two separate length scales:

$$l_Q = \frac{Q}{M^{1/2}} \quad (3.22a) \qquad\qquad l_M = \frac{M^{3/4}}{B^{1/2}} \quad (3.22b)$$

The first length scale is important in the analysis of the jets and represents the distance from the origin over which the initial conditions influence the flow field. The second includes the effect of buoyancy and represents the relative importance of the momentum flux and the buoyancy flux. Consequently, for a distance much lower than $l_M$, the flow is dominated by the momentum, and the behaviour is similar to the one of a jet; for distances larger than $l_M$, the flow is instead dominated by the buoyancy, and the behaviour is plume-like.

The length scales are related to the Froude number and nozzle by:

$$\frac{x}{D \cdot Fr} = \left(\frac{\pi}{4}\right)^{-1/4} \frac{x}{l_M} \quad (3.23a) \qquad\qquad Fr = \left(\frac{\pi}{4}\right)^{-1/4} \frac{l_M}{l_Q} \quad (3.23b)$$

Any flow variable is a function of these parameters. For example:

$$u_m = \frac{M}{Q} f\left(\frac{x}{l_Q}, \frac{x}{l_M}\right) \quad . \tag{3.24}$$

Note, however, that this is not a convenient function to evaluate, since *x* is involved in both independent parameters.

For x>>$l_Q$, the only relevant length scale for a round jet is $l_M$, and the expression for $u_m$ is:

$$u_m \frac{M^{1/4}}{B^{1/2}} = f\left(\frac{x \cdot B^{1/2}}{M^{3/4}}\right) \tag{3.25}$$

For B → 0, $w_m$ must be independent of B so that the form of *f* must be such that B vanishes. However, since B → 0 is formally identical to x → 0 or M → ∞, it follows that

$$u_m \frac{M^{1/4}}{B^{1/2}} \rightarrow c_1 \left( \frac{M^{3/4}}{xB^{1/2}} \right) \qquad \text{for } x \ll l_M \tag{3.26}$$

Similarly,

$$u_m \frac{M^{1/4}}{B^{1/2}} \rightarrow c_2 \left( \frac{M^{3/4}}{xB^{1/2}} \right)^{1/2} \qquad \text{for } x \gg l_M \tag{3.27}$$

where $c_1$ and $c_2$ are empirical constants.

Considering the scale $l_Q$, if x >>$l_Q$, the flow is fully developed and till x ~ $l_Q$ the flow is still controlled by the jet exit geometry. Thus, if $l_M$ and $l_Q$ are of the same order, then the flow is similar to a plume from the outset. The ratio between the two length scales is the Richardson number ($R_0$) and for a round jet is:

$$R_0 = \frac{l_Q}{l_M} = \left( \frac{\pi}{4} \right)^{1/4} \left( \frac{g'_0 D^{3/4}}{W^2} \right)^{1/2} = \left( \frac{\pi}{4} \right)^{1/4} \frac{1}{Fr} \tag{3.28}$$

### 3.2.4. Dependence with discharge inclination

The previous considerations apply for buoyant jets released vertically. However, in order to increase the length path, it is more useful to use different inclinations. For example, in negatively buoyant jets, this path can be extended using different angles. To maximize the path and consequently the dilution, a discharge inclination of 65° to the horizontal axis is useful (see Ferrari et al., 2010). Generally, with a dense effluent, it is better to avoid the angle of 90°, where the jet falls on itself and the entrainment is mostly with the same fluid.

The geometrical parameter of the jet, following the dimensional analysis of Fisher et al. (1979), can be expressed as:

$$z_t \approx \frac{(M \cdot \sin\theta)^{3/4}}{B^{1/2}} \quad , \tag{3.29}$$

where $\theta$ is the angle from the horizontal and $z_t$ is the maximum height of rise.

# Chapter 4

# Numerical model of buoyant jets

## 4.1 - Introduction

The strategy of Computational Fluid Dynamics (CFD) is to replace the continuous problem domain of the Navier-Stokes equations with a discrete domain, i.e. the quantities are calculated only in the given grid points. The system is transformed into a large set of coupled, algebraic equations.

The fundamental elements of any CFD simulation are (Apsley 2013):

- The flow field is discretized into a finite number of nodes, and the variables are approximated by their values in these nodes

- The equations of motion are discretized by means of numerical methods to obtain a system of algebraic equations;

- The resulting system of algebraic equations is solved to obtain values at the nodes.

The main stages in a CFD simulation are:

**Pre-processing**

- Formulation of the problem

    - Determination of the equation to be solved

    - Specification of the boundary conditions

- Construction of a computational mesh

**Solving:**

- Discretization of the governing equations;

- Solving the resulting system of algebraic equations.

**Post-processing**:

- Validation (comparison to measurements or analytical predictions, grid independency check)

- Analysis of results (calculation of derived quantities: forces, flow rates, etc.).

- Visualization (graphs and plots of the solution);

## 4.2 - Basic governing equations

In the numerical simulation, the first step is the determination of the governing equation of the problem. For NBJs, the equations are the continuity equation, the momentum conservation equations, a transport equation and an equation of state.

The simplifying assumptions that can be considered are: incompressible fluid, Boussinesq approximation (density difference negligible with the exception of the buoyancy forces and molecular diffusion negligible).

### 4.2.1. Boussinesq hypothesis

Under the hypothesis of Boussinesq, the pressure distribution is hydrostatic for a stagnant receiving fluid:

$$\frac{\partial p_0}{\partial z} = -\rho_0 \cdot g \quad . \tag{4.1}$$

If the receptor fluid is not stagnant:

$$\begin{aligned} p(t,x,y,z) &= p_0(z) + \tilde{p}(t,x,y,z) \\ \rho(t,x,y,z) &= \rho_0(z) + \tilde{\rho}(t,x,y,z) \end{aligned} \tag{4.2}$$

where

$\rho_0$ is the reference density,

$\tilde{\rho}$ is the deviation from the reference density,

$p_0$ is the hydrostatic pressure,

$\tilde{p}$ is the deviation from the hydrostatic pressure.

The deviation from the hydrostatic pressure and from the reference density in general is small:

$$\tilde{\rho} << \rho_0 \qquad\qquad \tilde{p} << p_0 \tag{4.3}$$

Under the Boussinesq hypothesis, the relative variation of velocity is considered smaller than the relative variation of density:

$$\frac{\Delta\rho}{\rho} \cong \frac{\Delta\rho_0}{\rho_0} << \frac{\Delta u}{u} \tag{4.4}$$

The Boussinesq hypothesis is verified for velocities smaller than the speed of sound. Under this hypothesis, the Navier-Stokes equation has a special form.

### 4.2.2. Continuity equation

Considering a material volume V(t) and mass $M = \int_{V(t)} \rho dV$ , the conservation of mass can be expressed as

$$\frac{DM}{Dt} = \frac{D}{Dt}\int_{V(t)} \rho dV = 0 \quad . \tag{4.5}$$

Applying the transport theorem:

$$\frac{DM}{Dt} = \int_{V(t)} \frac{\partial \rho}{\partial t} dV + \int_{S(t)} \rho\vec{u}\cdot\vec{n} dS = \int_{V(t)} \left(\frac{\partial \rho}{\partial t} + \nabla\cdot(\rho\vec{u})\right) dV = 0 \quad . \tag{4.6}$$

If the argument function is required to be continuous to the first order, it follows that

$$\frac{\partial \rho}{\partial t} + \nabla\cdot(\rho\vec{u}) = \frac{\partial \rho}{\partial t} + \rho\nabla\cdot\vec{u} + \vec{u}\nabla\cdot\rho = 0 \quad , \tag{4.7}$$

$$\frac{D\rho}{Dt} + \rho\nabla\cdot\vec{u} = 0 \quad , \tag{4.8}$$

and under the Boussinesq hypothesis

$$\frac{D\rho_0}{Dt} + \frac{D\tilde{\rho}}{Dt} + \rho_0\nabla\cdot\vec{u} + \tilde{\rho}\nabla\cdot\vec{u} = 0 \quad . \tag{4.9}$$

Since $\rho_0$ is a constant, $\tilde{\rho} \to 0$ therefore Eq. (4.09) can be expressed as

$$\frac{D\,{}^{\tilde{\rho}}\!/_{\rho_0}}{Dt} + \nabla\cdot\vec{u} = 0 \quad . \tag{4.10}$$

Since the deviation from the reference density is small, we get

$$\frac{D\,\tilde{\rho}/\rho_0}{Dt} \cong 0,$$

and the equation (4.10) becomes

$$\nabla \cdot \vec{u} = 0 \tag{4.11}$$

### 4.2.3. Momentum equation

Momentum of a control volume is $\vec{q} = \int_{V(t)} \rho \vec{u} dV$ .

According to the momentum conservation principle, the fluid particles acceleration in a material volume *V(t)* is equal to the sum of the surface forces and the body forces.

$$\frac{D\vec{q}}{Dt} = \vec{R} \quad , \tag{4.12}$$

$$\frac{D}{Dt} \int_{V(t)} \rho \vec{u} dV = \int_{V(t)} \rho \vec{f} dV + \int_{S(t)} \underline{\underline{\tau}} \cdot \vec{n} dS \quad , \tag{4.13}$$

where:

$\int_{V(t)} \rho \vec{f} dV$ are the mass forces, the only one considered in this case is the gravity $\rho \vec{g} dV$

$\int_{S(t)} \underline{\underline{\tau}} \cdot \vec{n} dS$ are the forces acting in the material surface {S(t)}.

Applying the transport theorem, the equation (4.13) becomes:

$$\frac{D}{Dt} \int_{V(t)} \rho \vec{u} dV = \int_{V(t)} \frac{D}{Dt}(\rho \vec{u}) + (\rho \vec{u}) \nabla \cdot \vec{u} = \int_{V(t)} \left[ \rho \frac{D\vec{u}}{Dt} + \vec{u} \frac{D\rho}{Dt} + (\rho \vec{u}) \nabla \cdot \vec{u} \right] dV \tag{4.14}$$

$$\int_{V(t)} \left[ \vec{u} \left( \frac{D\rho}{Dt} + \rho (\nabla \cdot \vec{u}) \right) + \rho \frac{D\vec{u}}{Dt} \right] dV \tag{4.15}$$

$$\int_{V(t)} \rho \frac{D\vec{u}}{Dt} dV = \int_{V(t)} \rho \vec{f} dV + \int_{S(t)} \underline{\underline{\tau}} \cdot \vec{n} dS = \int_{V(t)} \left( \rho \vec{f} + \nabla \cdot \underline{\underline{\tau}} \right) dV \tag{4.16}$$

$$\int_{V(t)} \left( \rho \frac{D\vec{u}}{Dt} + \rho \vec{f} + \nabla \cdot \underline{\underline{\tau}} \right) dV = 0 \tag{4.17}$$

Considering that the equation (4.17) is continuous, it can be expressed as:

$$\rho \frac{D\vec{u}}{Dt} = \rho \vec{f} + \nabla \cdot \underline{\underline{\tau}} \tag{4.18}$$

If we assume constant material properties of a Newtonian fluid, the stress tensor can be expressed as:

$$\underline{\underline{\tau}} = -p \cdot I + \lambda \cdot (\nabla \cdot \vec{u}) \cdot I + 2 \cdot \mu \cdot \underline{\underline{e}} \quad , \tag{4.19}$$

where $p$ is the pressure and $\mu$ is the coefficient of viscosity and $\lambda = -\frac{2}{3}\mu$

In particular

$$\underline{\underline{\tau}} = -p \cdot I + 2 \cdot \mu \left( \underline{\underline{e}} - \frac{1}{3} (\nabla \cdot \vec{u}) \cdot I \right) \quad , \tag{4.20}$$

$$\tau_{ij} = -p \cdot \delta_{ij} + 2 \cdot \mu \left( e_{ij} - \frac{1}{3} u_{k,k} \cdot \delta_{ij} \right) \; , \tag{4.21}$$

where $e_{ij} = \frac{1}{2}(u_{i,j} + u_{j,i})$. Substitution yields

$$\tau_{ij} = -p \cdot \delta_{ij} + \mu \cdot (u_{i,j} + u_{j,i}) - \frac{2}{3} \cdot \mu \cdot u_{k,k} \cdot \delta_{ij} \; , \tag{4.22}$$

$$\tau_{ij,j} = -p_{,i} + \mu \cdot (u_{i,j} + u_{j,i})_{,j} - \frac{2}{3}\mu \cdot (u_{k,k})_{,i} \quad . \tag{4.23}$$

Substituting with Equation (4.23) into Equation (4.18) gives

$$\rho \frac{Du_i}{Dt} = \rho f_{,i} - p_{,i} + \mu \cdot u_{i,jj} + \mu \cdot u_{j,ij} - \frac{2}{3}\mu \cdot u_{j,ji} \tag{4.24}$$

Applying Schwartz's theorem we get,

$$\frac{D\vec{u}}{Dt} = \nabla \vec{f} - \frac{\nabla \vec{p}}{\rho} + \nu \cdot \left[ \nabla^2 \vec{u} + \frac{1}{3} \cdot \nabla (\nabla \cdot u) \right] \tag{4.25}$$

If the fluid is incompressible ($\nabla \cdot \vec{u} = 0$) and the only mass force is the gravity: $\vec{f} = -g \cdot \vec{z}$, it follows

$$\rho \frac{D\vec{u}}{Dt} = -\rho g \nabla \vec{z} - \nabla \vec{p} + \mu \cdot \nabla^2 \vec{u} \tag{4.26}$$

Under the Boussinesq hypothesis,

$$(\rho_0+\tilde{\rho})\frac{D\vec{u}}{Dt}=-(\rho_0+\tilde{\rho})g\nabla\vec{z}-\nabla\vec{p}+\mu\cdot\nabla^2\vec{u} \quad . \tag{4.27}$$

Defining the modified pressure p as

$$p=P+\tilde{p} \quad , \tag{4.28}$$

where

$P$ is the hydrostatic pressure,

$\tilde{p}$ is the deviation from the hydrostatic pressure,

$$p=p_0-\rho_0 gz-\tilde{p} \quad , \tag{4.29}$$

$p_0$ = pressure at z = 0

$$\nabla p=-\rho_0 g\nabla z-\nabla\tilde{p} \quad . \tag{4.30}$$

The equation (4.27) becomes,

$$(\rho_0+\tilde{\rho})\frac{D\vec{u}}{Dt}=-(\rho_0+\tilde{\rho})g\nabla z+\rho_0 g\nabla z-\nabla\tilde{p}+\mu\cdot\nabla^2\vec{u} \quad . \tag{4.31}$$

Neglecting the deviation of the density, whit respect to the reference density,

$$\rho_0\frac{D\vec{u}}{Dt}=-\tilde{\rho}g\nabla z-\nabla\tilde{p}+\mu\cdot\nabla^2\vec{u} \quad , \tag{4.32}$$

and introducing $g'=\frac{\tilde{\rho}}{\rho_0}g$ , one obtains

$$\frac{D\vec{u}}{Dt}=-g'\nabla z-\frac{\nabla\tilde{p}}{\rho_0}+\nu\cdot\nabla^2\vec{u} \quad , \tag{4.33}$$

where $-g'\nabla z$ are the buoyancy forces.

### 4.2.4 Tracer Conservation Equation

A scalar is passive when its value has no effects on material properties in the fluid dynamics.

If $C$ is the concentration of the passive scalar, the equation of conservation, in a more general way, can be expressed as:

$$\frac{DC}{Dt}=\nu_C\nabla^2 C+S_C \tag{4.34}$$

where $S_C$ is the scalar source of unit mass, and $\nu_C$ is the molecular diffusivity.

## 4.3 - Mean - Flow equations

### 4.3.1 Reynolds decomposition

Decomposition of a variable $A$ into its mean $\overline{A}$, and into its fluctuation $A'$:

$$A(x,t) = \overline{A}(x,t) + A'(x,t) \quad , \tag{4.35}$$

where $\overline{A}$ denotes the average of $A$ and $A'$ is its fluctuating part (or perturbations). If the process is stationary and ergodic, it is possible to use the time instead of the ensemble average.

Note that the mean of a mean value remains the mean value:

$$\overline{A} = \overline{\overline{A}} \ . \tag{4.36}$$

Similarly, the mean of a fluctuating quantity vanishes:

$$\overline{A} = \overline{\overline{A}} + \overline{A'} \quad \Rightarrow \quad \overline{A'} = 0 \tag{4.37}$$

### 4.3.2. Mean Continuity equation

Using the continuity equation (4.11),

$$\nabla \cdot \vec{u} = 0 \quad , \tag{4.38}$$

furthermore applying Reynolds averaging yields

$$\overline{u}_{i,j} + u'_{i,j} = 0 \ . \tag{4.39}$$

The second (fluctuating) term on the left hand side of Equation (4.39) vanishes while taking the mean:

$$\overline{u}_{i,j} + \overline{u}'_{i,j} = 0 \ \Rightarrow \quad \overline{u}_{i,j} = 0 \tag{4.40}$$

### 4.3.3. Mean Momentum equation

The momentum equation (4.33)

$$\frac{Du_i}{Dt} = -g' z,_i - \frac{\tilde{p},_i}{\rho_0} + \nu \cdot u_{i,jj} \tag{4.41}$$

can also be expressed as

$$u_{i,t} + u_j \cdot u_{i,j} = -\frac{\tilde{\rho}}{\rho_0} g \cdot z,_i - \frac{\tilde{p},_i}{\rho_0} + \nu \cdot u_{i,jj} \quad . \tag{4.42}$$

Applying the Reynolds decomposition Equation (4.42) becomes

$$\bar{u}_{i,t} + u'_{i,t} + \left(\bar{u}_j + u'_j\right) \cdot \left(\bar{u}_{i,j} + u'_{i,j}\right) = -\frac{\bar{\tilde{\rho}}}{\rho_0} g \cdot z,_i - \frac{\tilde{\rho}'}{\rho_0} g \cdot z,_i - \frac{\tilde{p},_i}{\rho_0} + \nu \cdot \bar{u}_{i,jj} + \nu \cdot u'_{i,jj} \tag{4.43}$$

Upon performing the indicating multiplications, and separating terms, the mean of the previous equation is:

$$\bar{u}_{i,t} + \bar{u}'_{i,t} + \bar{u}_j \bar{u}_{i,j} + \bar{u}_j \bar{u}'_{i,j} + \bar{u}'_j \bar{u}_{i,j} + \overline{u'_j u'}_{i,j} = -\frac{\bar{\tilde{\rho}}}{\rho_0} g \cdot z_{,i} - \frac{\bar{\tilde{\rho}}'}{\rho_0} g \cdot z_{,i} - \frac{\tilde{p}_{,i}}{\rho_0} + \nu \cdot \bar{u}_{i,jj} + \nu \cdot \bar{u}'_{i,jj}$$

$$\bar{u}_{i,t} + \bar{u}_j \bar{u}_{i,j} + \overline{u'_j u'}_{i,j} = -\frac{\bar{\tilde{\rho}}}{\rho_0} g \cdot z_{,i} - \frac{\tilde{p}_{,i}}{\rho_0} + \nu \cdot \bar{u}_{i,jj} \tag{4.44}$$

Note that

$$\left(\overline{u'_j u'_i}\right)_{,j} = \overline{u'_j u'}_{i,j} - \overline{u'_i u'}_{j,j} = \overline{u'_j u'}_{i,j} \tag{4.45}$$

Equation (4.44) becomes

$$\bar{u}_{i,t} + \bar{u}_j \bar{u}_{i,j} + \left(\overline{u'_j u'}_i\right)_{,j} = -\frac{\bar{\tilde{\rho}}}{\rho_0} g \cdot z_{,i} - \frac{\tilde{p}_{,i}}{\rho_0} + \nu \cdot \bar{u}_{i,jj} \tag{4.46}$$

The constitutive equation for the total stresses is equal to

$$\tau_{Tij} = -\tilde{p} \cdot \delta_{ij} + 2 \cdot \mu \cdot \bar{e}_{ij} - \rho_0 \cdot \overline{u'_j u'_i} \tag{4.47}$$

$\tau_{Rij} = -\rho_0 \cdot \overline{u'_j u'_i}$ where $\tau_{Rij}$ are the so called Reynolds stresses

The derivative of the equation (4.47) is

$$\tau_{Tij,j} = -\tilde{p}_{,i} + \mu \cdot \bar{u}_{i,jj} - \rho_0 \cdot \left(\overline{u'_j u'}_i\right)_{,j} \tag{4.48}$$

so, the equation (4.46) becomes

$$\bar{u}_{i,t} + \bar{u}_j \bar{u}_{i,j} = -\frac{\bar{\tilde{\rho}}}{\rho_0} g \cdot z_{,i} - \frac{1}{\rho_0} \tau_{Tij,j} \tag{4.49}$$

In the equation (4.46),

$\bar{u}_{i,t}$ represents the storage of momentum (inertia)

$\overline{u}_j \overline{u}_{i,j}$ describes the advection of mean momentum

$-\dfrac{\overline{\tilde{\rho}}}{\rho_0} g \cdot z_{,i}$ represents the gravity force

$-\dfrac{1}{\rho_0} \tau_{Tij,j}$ represents the influence of the surface forces

$\left(\overline{u'_j u'_i}\right)_{,j}$ represents the influence of the Reynolds stresses on the mean motion

$-\dfrac{\tilde{p}_{,i}}{\rho_0}$ describes the mean pressure gradient forces

$\nu \cdot \overline{u}_{i,jj}$ represents the influence of viscous stresses on the mean motion influence of the surface forces.

### 4.3.4 Mean tracer conservation equation

Applying the Reynolds decomposition to equation (4.45), one obtains

$$\frac{DC}{Dt} = \frac{\partial \overline{C}}{\partial t} + \nabla\left(\overline{uC} + \overline{u'C'}\right) = \nu_C \nabla^2 \overline{C} + S_C \qquad (4.50)$$

where

$\dfrac{\partial \overline{C}}{\partial t}$ represents the mean storage of tracer C,

$\nabla\left(\overline{uC}\right)$ describes the advection of the tracer by the mean flow,

$\nabla\left(\overline{u'C'}\right)$ represents the divergence of turbulent tracer flux,

$\nu_C \nabla^2 \overline{C}$ represents the mean molecular diffusion of the tracer,

$S_C$ is the mean net body source term for additional tracer processes.

The term $\left(\overline{u'C'}\right)$ is an analogue term of the Reynolds shear stresses for the mean tracer conservation equation.

### 4.3.5. Kinetic Energy equation for the mean flow

The kinetic energy for the mean flow can be defined as

$$E = \frac{1}{2}\sum_{i=1}^{3}\overline{u}_i^{\,2} \tag{4.51}$$

Multiplying Equation (4.49) by $\overline{u}_i$ yields

$$\overline{u}_i\overline{u}_i,_t + \overline{u}_i\overline{u}_j\overline{u}_i,_j = -\overline{u}_i\frac{\overline{\tilde{\rho}}}{\rho_0}g\cdot z,_i - \overline{u}_i\frac{1}{\rho_0}\tau_{Tij},_j \tag{4.52}$$

$$\left(\frac{\overline{u}_i}{2}\right)^2,_t + \overline{u}_j\left(\frac{\overline{u}_i}{2}\right)^2,_j = -\overline{u}_i\frac{\overline{\tilde{\rho}}}{\rho_0}g\cdot z,_i - \overline{u}_i\frac{1}{\rho_0}\tau_{Tij},_j \tag{4.53}$$

The equation (4.53), taking into account the equation (4.51), can be expressed as

$$E_{,t} + \overline{u}_j E_{,j} = -\overline{u}_i\frac{\overline{\tilde{\rho}}}{\rho_0}g\cdot z_{,i} - \overline{u}_i\frac{1}{\rho_0}\tau_{Tij_{,j}} \tag{4.54}$$

In Equation (4.54) it can be seen that the variation of the kinetic energy is due to the work of the gravitational forces $\overline{u}_i\frac{\overline{\tilde{\rho}}}{\rho_0}g$ and of the total stresses $\overline{u}_i\frac{1}{\rho_0}\tau_{Tij},_j$.

### 4.3.6. Kinetic Energy equation for the turbulent flow

The kinetic energy for a turbulent flow can be expressed as

$$\varepsilon = \frac{1}{2}\sum_{i=1}^{3}\overline{u}_i'^2 \tag{4.55}$$

.

The Navier – Stokes equations under the Boussinesq hypothesis are

$$u_i,_t + u_j\cdot u_i,_j = -\frac{\tilde{\rho}}{\rho_0}g\cdot z,_i - \frac{\tilde{p},_i}{\rho_0} + 2\nu\cdot u_i,_{jj} \tag{4.56}$$

Using the Reynolds decomposition, one obtains

$$\overline{u}_i,_t + u'_i,_t + \left(\overline{u}_j + u'_j\right)\cdot\left(\overline{u}_i,_j + u'_i,_j\right) =$$

$$= -\frac{\overline{\tilde{\rho}}}{\rho_0}g\cdot z,_i - \frac{\tilde{\rho}'}{\rho_0}g\cdot z,_i - \frac{\overline{\tilde{p}},_i}{\rho_0} - \frac{\tilde{p}',_i}{\rho_0} + 2\nu\cdot\overline{e}_i,_{jj} + 2\nu\cdot e'_{ij},_j \tag{4.57}$$

The mean part is

$$\bar{u}_i,_t + _t + \bar{u}_j \bar{u}_i,_j = -\frac{\bar{\tilde{\rho}}}{\rho_0} g \cdot z,_i - \frac{\bar{\tilde{p}},_i}{\rho_0} - \left(\overline{u'_j u'_i}\right),_j + 2\nu \cdot \bar{e}_{ij},_j \tag{4.58}$$

Subtracting the equation (4.57) from the equation (4.58)

$$u'_i,_t + u'_j \bar{u}_i,_j + \bar{u}_j u'_i,_j + u'_j u'_i,_j = -\frac{\tilde{\rho}'}{\rho_0} g \cdot z,_i - \frac{\tilde{p}',_i}{\rho_0} + 2\nu \cdot e'_{ij},_j + \left(\overline{u'_j u'_i}\right),_j \tag{4.59}$$

Note that

$\tilde{\rho}' = \rho'$ ,

$\tilde{p}' = p'$ ,

Under the previous consideration

$$u'_i,_t + u'_j \bar{u}_i,_j + \bar{u}_j u'_i,_j + u'_j u'_i,_j = -\frac{\rho'}{\rho_0} g \cdot z,_i - \frac{p',_i}{\rho_0} + 2\nu \cdot e'_{ij},_j + \left(\overline{u'_j u'_i}\right),_j \tag{4.60}$$

Multiplying the equation (4.60) with $u'_i$ and averaging

$$\begin{aligned} &\overline{u'_i u'_i,_t} + \overline{u'_i u'_j \bar{u}_i,_j} + \bar{u}_j \overline{u'_i u'_i,_j} + \overline{u'_i u'_j u'_i,_j} = \\ &= -\overline{u'_i \frac{\rho'}{\rho_0} g \cdot z,_i} - \overline{u'_i \frac{p',_i}{\rho_0}} + 2\nu \cdot \overline{u'_i \cdot e'_{ij},_j} + \overline{u'_i}\left(\overline{u'_j u'_i}\right),_j \end{aligned} \tag{4.61}$$

$$\overline{\left(\frac{u'_i}{2}\right)^2},_t + \overline{u'_j \left(\frac{u'_i}{2}\right)^2},_j + \bar{u}_j \overline{\left(\frac{u'_i}{2}\right)^2},_j + \overline{u'_i u'_j u'_i,_j} = -\overline{u'_i \frac{\rho'}{\rho_0} g \cdot z,_i} - \frac{\overline{(u'_i\ p'),_i}}{\rho_0} + 2\nu \cdot \overline{u'_i \cdot e'_{ij},_j} \tag{4.62}$$

then,

$$\bar{\varepsilon},_t + \bar{u}_j \bar{\varepsilon},_j = -\overline{u'_i \frac{\rho'}{\rho_0} g \cdot z,_i} - \frac{\overline{(u'_i\ p'),_i}}{\rho_0} - \underbrace{\overline{u'_i u'_j} \bar{u}_i,_j}_{a} - \left(\overline{u'_j\ \varepsilon}\right),_j + \underbrace{2\nu \cdot \overline{u'_i \cdot e'_{ij},_j}}_{b} \tag{4.63}$$

The term (a) in the equation (4.63) can be express as

$$\overline{u'_i u'_j} \bar{u}_i,_j = -\frac{\overline{\underline{\underline{\tau_R}}}}{\rho_0} \cdot \nabla \bar{u}^T = -\frac{\overline{\underline{\underline{\tau_R}}}}{\rho_0} \cdot \left(\underline{\underline{e}} + \underline{\underline{r}}\right) = -\frac{\overline{\underline{\underline{\tau_R}}}}{\rho_0} \cdot \underline{\underline{e}} - \frac{\overline{\underline{\underline{\tau_R}}}}{\rho_0} \cdot \underline{\underline{r}} \tag{4.64}$$

Since the scalar product between the symmetric and antisymmetric tensors is equal to zero i.e. $\left(\frac{\overline{\underline{\underline{\tau_R}}}}{\rho_0}\cdot \underline{\underline{r}} = 0\right)$, then the equation (4.64) becomes

$$-\frac{\overline{\underline{\underline{\tau_R}}}}{\rho_0}\cdot \underline{\underline{e}} = \overline{u'_i\, u'_j}\, \overline{e}_{ij}$$

The term (b) in the equation (4.63) can be expressed as

$$\overline{u'_i \cdot e'_{ij}}{,}_j = \left(\overline{u'_i \cdot e'_{ij}}\right){,}_j - \overline{u'_i{,}_j \cdot e'_{ij}} = \nabla\left(\overline{\vec{u'}\cdot \underline{\underline{e'}}}\right) - \overline{\nabla u'^T \cdot \underline{\underline{e'}}} = \nabla\left(\overline{\vec{u'}\cdot \underline{\underline{e'}}}\right) - \overline{\left(\underline{\underline{e'}} + \underline{\underline{r'}}\right)\cdot \underline{\underline{e'}}} =$$

$$= \nabla\left(\overline{\vec{u'}\cdot \underline{\underline{e'}}}\right) - \overline{\underline{\underline{e'}}\cdot\underline{\underline{e'}}} - \overline{\underline{\underline{r'}}\cdot\underline{\underline{e'}}} = \nabla\left(\overline{\vec{u'}\cdot \underline{\underline{e'}}}\right) - \overline{\underline{\underline{e}}'^2} = \left(\overline{u'_i \cdot e_{ij}'}\right){,}_j - \overline{e_{ij}'^2}$$

Under the previous consideration, the turbulent kinetic energy equation can be expressed as

$$\overline{\varepsilon}{,}_t + \overline{u}_j\, \overline{\varepsilon}{,}_j + \left(\overline{u'_j\, \varepsilon}\right){,}_j = -\frac{g}{\rho_0}\overline{u'_i\, \rho' \cdot z{,}_i} - \frac{\overline{(u'_i\, p'){,}_i}}{\rho_0} - \overline{u'_i\, u'_j}\,\overline{e}_{ij} + 2\nu\cdot\left(\overline{u'_i \cdot e_{ij}'}\right){,}_j - 2\nu\overline{e_{ij}'^2} \tag{4.65}$$

The meaning of the terms in the equation (4.65) is

| | |
|---|---|
| $\overline{\varepsilon}{,}_t$ | represents the local storage or tendency of the turbulent kinetic energy (TKE) |
| $\overline{u}_j\,\overline{\varepsilon}{,}_j$ | represents the advection of TKE by the mean flow |
| $\left(\overline{u'_j\, \varepsilon}\right){,}_j$ | represents the transport of the TKE due to turbulent flow |
| $-\frac{g}{\rho_0}\overline{u'_i\, \rho' \cdot z{,}_i}$ | is the buoyant production or consumption term. It is a production or loss term, so can produce or destroy turbulence depending on whether the flux $\overline{u'_i\, \rho'}$ is positive (positive buoyancy) or negative (negative buoyancy). The term acts only in the vertical component of the velocity fluctuation. |
| $-\frac{\overline{(u'_i\, p'){,}_i}}{\rho_0}$ | is a pressure correlation term that describes how TKE is redistributed by pressure perturbations |
| $-\overline{u'_i\, u'_j}\,\overline{e}_{ij}$ | is the mechanical production of turbulent kinetic energy |

$2\nu \cdot \left(\overline{u'_i \cdot e_{ij}'}\right)_{,j}$ represents the work of the viscous forces due to the velocity fluctuations

$-2\nu\overline{e_{ij}}'^2$ represents the viscous dissipation of the turbulent kinetic energy

## 4.4 – Closure problem

Equation (4.46) is an equation for the mean quantities $\overline{u}$ and $\overline{p}$. It contains 6 unknowns, involving turbulent fluctuations. They are nonlinear terms, act like stresses, but represent the mean momentum flux into or out of the material volume caused by the turbulent fluctuations (see Davidson 2004).

Noting that the Reynolds stresses are

$$\tau_{ij}^R = -\rho\overline{u'_i\, u'_j}$$

We can rewrite the equation (4.46) as

$$\rho\left(\overline{u} \cdot \nabla\right)\overline{u}_i = -\frac{\partial \overline{p}}{\partial x_i} + \frac{\partial}{\partial x_j}\left[\overline{\tau}_{ij} + \tau_{ij}^R\right] \tag{4.67}$$

Considering Equation (4.67) and (4.41), we obtained 4 equations and 10 unknowns: 3 mean velocity components $\overline{u}_i$, mean pressure $\overline{p}$ and 6 components of the Reynolds stress tensor $\overline{u'_i\, u'_j}$ .

When one includes more equations, one obtains even more new unknowns. The description of turbulence is not closed. Therefore by moving from a deterministic problem to a statistical description of the Navier - Stokes equation makes the system underdetermined.

To make the mathematical description of the turbulence tractable, one approach is to use only a finite number of equations, and then determine the unknown turbulence terms as functions of known parameters (closure approximation or closure assumption).

The closure approximation can be local or non-local, in the first case an unknown quantity in a point in the space is parameterized by values of quantities at the same point. In non-local closure, the unknown quantity at one point is parameterized by values of known quantities at any point in space. Neither of the methods is exact, but both appear to work well according to the particular physical situation for which they are designed.

A similar parameterization, must respect the following principles:

- have the same dimension of the unknown terms,
- have the same tensor properties,
- have the same symmetries,
- be invariant under an arbitrary transformation of coordinates system,
- be invariant under a Galilean (i.e. inertial or Newtonian) transformation,
- satisfy the same constrains and budget equations.

### 4.4.1 – Zero order local closure equations

The Zero order closure implies that no equations are used to predict the turbulence; therefore they are directly parameterized as a function of space and time.

### 4.4.2 – First order local closure equations

The first order turbulence models are probably the oldest and the easiest methods for the approximation of the equation for the mean flow into RANS (Reynolds averaged Navier – Stokes) models.

The turbulent flow of a generic quantity *A* can be related with the local gradient of its mean quantity by an expression like:

$$\overline{u'_i\, A'} = -K \frac{\partial \overline{A}}{\partial x_j} \qquad (4.67)$$

Where K is the diffusivity coefficient related to the flow and not to the property of the fluid.

The parameterizations for K should satisfy the following constrains:

- K = 0 if the turbulence is absent,
- K = 0 on the ground,
- K increases as the turbulent kinetic energy increases,
- K varies with statistic stability,
- K is non-negative.

The first of these models was developed by Boussinesq in the 1980s. He proposed a shear-stress strain-rate relationship for time averaged flows of a one dimensional nature:

$$\overline{\tau}_{xy} + \overline{\tau}^{R}_{xy} = \rho(\upsilon + \upsilon_t)\frac{\partial \overline{u}_x}{\partial y} \qquad (4.68)$$

where $\upsilon_t$ is the eddy viscosity.

The general idea of the model is that the effect of the turbulent mixing of momentum is analogous to the molecular transport of momentum.

The eddy viscosity is a property of the turbulence and Prandtl (1910) gives a formulation to estimate $\upsilon_t$ known as mixing-length model:

$$\upsilon_t = l_m V_t \tag{4.69}$$

where $l_m$ is called the mixing length and $V_t$ is a suitable measure of $|u'|$.

After several assumption (see Davidson 2004 for a complete description), the eddy viscosity could be expressed as

$$\upsilon_t = l_m{}^2 \frac{\partial \overline{u}_x}{\partial y} \quad . \tag{4.70}$$

For a jet, the Prandtl model works well, and it was found that $l_m$ is reasonably uniform and of the order of $l_m = c\delta$, where δ is the local thickness of the layer and *c* is a constant that depends on the type of the flow (figure 4.1).

One limitation of this relation is that on the centreline of the jet, $\upsilon_t = 0$ that is not verified in simple jet.

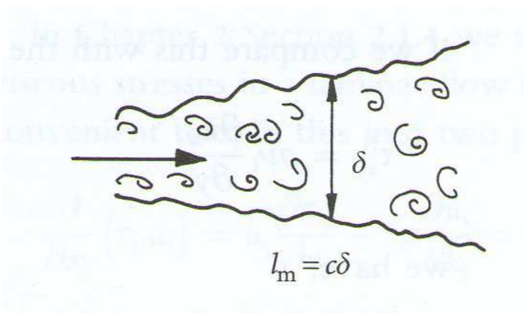


**Figure 4.1 Mixing length for a jet (Davidson 2004)**

Due to the development of the digital computer power, the complexity of this class of turbulence models was increased, developing higher order closure models. The most noteworthy efforts in the development of this class of models were performed by Donaldson and Rosenbaum (1968), Daly and Harlow (1970) and Launder et al. (1975). The latter has become the baseline second-order closure model with more relative recent contributions made by Lumley (1978), Speziale (1987), etc.

## 4.5 – Round jet

An axisymmetric round jet is characterized by $\overline{u}_x >> \overline{u}_r$ and $\partial / \partial x << \partial / \partial r$ where *x* is the stream-wise direction and r the radial direction, $\overline{u}_x$ decreases during the path, and the widening $\delta$ increases as the jet spreads. It can be demonstrated that after 30 diameters downstream, the velocity profiles depends only on the radial position *r*, the local jet width $\delta$, and the local centreline velocity.

So it is possible to adopt a self-similar form

$$\frac{\overline{u}_z(r,x)}{\overline{u}_0(x)} = f\left(\frac{r}{\delta(x)}\right) \tag{4.71}$$

where $\overline{u}_0 = \overline{u}_0(0,x)$

It is possible to make a few assumptions:

- axial gradients in the Reynolds stresses much smaller than radial gradients,
- laminar stresses negligible,
- radial components of the mean inertial forces negligible.

According to these assumptions, in polar coordinated (r, θ, x), the Navier - Stokes equations may be simplified as

$$\begin{aligned} &\rho\overline{u} \cdot \nabla\overline{u_x} = -\frac{\partial \overline{p}}{\partial x} + \frac{1}{r}\frac{\partial}{\partial r}\left[r\tau_{rx}^{R}\right] \\ &0 = -\frac{\partial \overline{p}}{\partial x} + \frac{1}{r}\frac{\partial}{\partial x}\left[r\tau_{rr}^{R}\right] - \frac{\tau_{\theta\theta}^{R}}{r} \end{aligned} \tag{4.72}$$

Integrating the second, it is possible to note that the $\frac{\partial \overline{p}}{\partial x} = 0$ in the axial equation of motion.

Due to this consideration,

$$\rho\overline{u} \cdot \nabla\overline{u_x} = \frac{1}{r}\frac{\partial}{\partial r}\left[r\rho\overline{u}_r\,\overline{u}_x\right] + \frac{\partial}{\partial x}\left[r\rho\overline{u}_x^{2}\right] = \frac{1}{r}\frac{\partial}{\partial r}\left[r\tau_{rx}^{R}\right] \tag{4.73}$$

from which it is apparent that the momentum flux

$$M = \int_0^{\infty}\left[\rho\overline{u}_x^{2}\right]2\pi dr \tag{4.74}$$

is conserved.

Using the self-similar approximation $\overline{u}_x = \overline{u}_0 f(r/\delta)$, the mass and momentum flux can be expressed as

$$\dot{m} = \rho \bar{u}_0 \delta^2 \int_0^\infty 2\pi\eta f(\eta) d\eta \quad , \tag{4.75}$$

$$M = \rho \bar{u}_0^2 \delta^2 \int_0^\infty 2\pi\eta f^2(\eta) d\eta = \text{ constant} \quad , \tag{4.76}$$

where $\eta = r / \delta$.

Now the rate of change of the centreline velocity and of the widening can be estimated using an entrainment argument.

Under this approach, the fluctuations are considered proportional to the local value of $\bar{u}_0$, so it is possible to write

$$\frac{d\dot{m}}{dx} = \alpha\rho\bar{u}_0\delta \int_0^\infty 2\pi\eta f(\eta) d\eta \quad , \tag{4.77}$$

where $\alpha$ is the entrainment coefficient.

The two corresponding equations are

$$\frac{d}{dx}\left[\bar{u}_0\delta^2\right] = \alpha\rho\bar{u}_0\delta \tag{4.78}$$

$$\bar{u}_0^{\,2}\delta^2 = \text{constant}$$

An integration between 0 and infinite gives

$$\begin{aligned} \frac{\delta}{\delta_0} &= 1 + \frac{\alpha x^*}{\delta_0} \\ \frac{\bar{u}_0}{V_0} &= \left[1 + \frac{\alpha x^*}{\delta_0}\right]^{-1} \end{aligned} \tag{4.79}$$

Where $x^*$ is measured from the start of the self-similar portion of the jet and $\delta_0$ and $V_0$ are the value of velocity and widening at $x^*=0$.

## 4.6 – Integral models

The resolution of the previous equation, also with RANS models, has a large computational cost. Other models have been developed under several assumptions, such as axisymmetric and Gaussian behaviour. They are called integral jet models (Fisher et al., 1979).

The integral models are based on the entrainment hypothesis (suggested by Morton et al., 1956) that relates the inflow velocity to the mean local one in turbulent shear flow. This hypothesis was summarized by Turner (1986) who studied the entrainment in several flow conditions.

A jet released from a round orifice entrains external fluid and mixes and dilutes with its fluid; under the entrainment hypothesis, the external fluid is entrained with a velocity $u_e$, proportional to the mean centreline velocity $u_m$:

$$u_e = \alpha \cdot u_m \quad , \tag{4.80}$$

$\alpha$ is known as the entrainment coefficient, and was found by Fischer et al. (1979) to be equal to 0.0535 for a pure jet and 0.0833 for a pure plume.

For an inclined buoyant jet in a stagnant receiving body, the assumption that was generally made is that the entrainment at the edge of the plume is proportional to some characteristic velocity at that point:

- The conservation of volume flux Q is given by:

$$\frac{dQ}{ds} = 2\pi\alpha u_m b \, . \tag{4.81}$$

- The conservation of momentum flux M:

$$\frac{dM}{ds} = \pi b^2 \frac{\Delta\rho}{\rho} g \, . \tag{4.82}$$

- The conservation of tracer mass flux C:

$$\frac{dC}{ds} = 0 \, , \tag{4.83}$$

where b is the half width of the jet, $\rho$ the density of the receiving body, and s is the stream-wise coordinate that for Negative Buoyant jet is not a straight line.

### 4.6.1 Entrainment coefficient

The entrainment coefficient $\alpha$ is variable and the experiments suggest that it takes asymptotic values $\alpha_j$ and $\alpha_p$ in the jet-like behaviour and in the plume-like behaviour respectively, and between the two values in the transition flows.

An expression was proposed by Priestley and Ball (1955), and it is based on the conservation of energy:

$$\alpha = \alpha_j - (\alpha_j - \alpha_p)\left(\frac{R(s)}{R_p}\right)^2 \tag{4.84}$$

Where *R(s)* is the local Richardson number and s is the distance from the origin along the jet axis. $R_p$ is the limiting plume Richardson number.

The local Richardson number *R(s)* in a buoyant jet is defined as:

$$R(s) = \frac{\mu(s) \cdot \beta(s)^{1/2}}{m(s)^{5/4}} \quad , \tag{4.86}$$

where $\mu(s)$, *m(s)* and $\beta(s)$ are respectively the specific mass, momentum and buoyancy fluxes at a distance *s* from the origin.

A second empirical formula proposed by List (1982) is

$$\alpha = \alpha_j \exp\left[\ln\left(\frac{\alpha_p}{\alpha_j}\right) \cdot \left(\frac{R(s)}{R_p}\right)^2\right]. \tag{4.85}$$

All of these values were determined by means of experimental analysis.

## 4.7 - Computational Fluid Dynamics models

The most common approaches for the numerical resolution of the Navier-Stokes equations are:

**Direct Numerical Simulation (DNS)**: the Navier-Stokes equations are discretized and solved, with a grid able to contain all the scales of turbulence, consequently the smallest grid size is of the order of the Kolmogorov scale $\eta \sim L/(Re)^{3/4}$. This model is so feasible only for small Reynolds numbers.

**Large Eddy Simulation (LES):** the development of this model is founded on the observation that the small scales of turbulent motion posses a more universal character than the large scales, which transport the turbulent energy. Consequently the idea is to directly solve only the large scales of turbulence; the smaller scales are modelled with another equation to represent the turbulent small scales.

The separation of the scales is achieved by filtration, performed with the use of $G(x)$ filter, that allows one to transform an arbitrary flow field quantity $F(x)$ into its filtered form $\overline{F}(x)$, which is being resolved numerically.

The filtration form may be written as a convolution, which, for a simple one-dimensional case, may be written as:

$$\overline{F}(x) = G(x) * F(x) = \int_0^\infty G(x-\xi)F(\xi)d\xi \tag{4.90}$$

The application of the (4.90) in the Navier-Stokes equations, transform them into the following form:

$$u_{i,t} + (u_i \cdot u_j)_{,j} = -\frac{\tilde{p},_i}{\rho_0} + \left[\nu(u_{i,j} + u_{j,i}) - \tau_{ij}\right]_{,j} \tag{4.91}$$

Where $\tau_{ij}$ is the sub-grid stress tensor that has to be modelled.

The majority of the present models are the viscosity based models, that utilize the Boussinesq concept (Lesier and Metais 1996), transforming the sub-grid stress tensor into:

$$\tau_{ij} = \nu_t S_{ij} + \frac{1}{3}\tau_{ij} S_{ij} \tag{4.92}$$

where $\nu_t$ is the sub-grid eddy viscosity coefficient, and $S_{ij}$ is the rate of the strain tensor of the filtered flow field.

$$S_{ij} = u_{i,j} + u_{j,i} \tag{4.93}$$

The first sub-grid closure was proposed by Smagorinsky (1963), who developed a sub-grid analogy to the mixing length model, given by:

$$v_t = (C_S \Delta)^2 |S| \tag{4.94}$$

Where $\Delta$ denotes the characteristic sub-grid length scale, $C_s$ is a constant adjusted arbitrary according to the given flow, the absolute measure of local strain is given by the formula:

$$|S| = \sqrt{2S_{ij}S_{ij}} \tag{4.95}$$

**Reynolds Averaged Navier-Stokes (RANS) equations:** the averaged version of the Navier-Stokes equations are solved, with another equation to represent all the turbulent scales (see above).

### 4.7.1 - Boundary condition

In order to solve the closed set of governing equations, explained in the previous paragraphs, it is necessary to specify appropriate initial conditions and boundary conditions.

For steady state problems there are three types of spatial boundary conditions that can be specified as follows (Ashgriz and Mostaghimi 2002):

**- Dirichlet boundary condition**:

$$\phi = f_1(x, y, z) \tag{4.86}$$

the values of the variable $\phi$ on the boundary are known constants $f_1$. This allows a simple substitution to be made to fix the boundary value. For example, for no-slip and no-penetration conditions on the solid walls, the fluid velocity is the same as the velocity of the wall.

**- Neumann boundary condition:**

$$\frac{\partial \phi}{\partial n} = f_2(x, y, z) \tag{4.87}$$

Here the derivatives of the variable on the boundary are known, this gives an extra equation, which can be used to find the value at the boundary.

For example, if the velocity does not change downstream of the flow, we can assume that the derivative of is zero at that boundary.

**- Mixed type boundary condition:**

$$a\phi + b\frac{\partial \phi}{\partial n} = f_3(x, y, z) \tag{4.88}$$

The physical boundary conditions that are commonly observed in fluid problems are briefly presented here (Ashgriz and Mostaghimi 2002).

- **Solid walls**: Many boundaries within a fluid flow domain will be solid walls, and these can be either stationary or moving walls. If the flow is laminar then the velocity components can be set to be the velocity of the wall. When the flow is turbulent, however, the situation is more complex.

**- Inlets:** At an inlet, fluid enters the domain and, therefore, its fluid velocity or pressure, or the mass flow rate may be known. Also, the fluid may have certain characteristics, such as the turbulence characteristics which need to be specified.

**- Symmetry boundaries:** When the flow is symmetrical about some plane there is no flow through the boundary and the derivatives of the variables normal to the boundary are zero.

**- Cyclic or periodic boundaries:** These boundaries come in pairs and are used to specify that the flow has the same values of the variables at equivalent positions on both of the boundaries.

**- Pressure boundary conditions:** The ability to specify a pressure condition at one or more boundaries of a computational region is an important and useful computational tool. Pressure boundaries represent such things as confined reservoirs of fluid, ambient laboratory conditions and applied pressures arising from mechanical devices. Generally, a pressure condition cannot be used at a boundary where velocities are also specified, because velocities are influenced by pressure gradients. The only exception is when pressures are necessary to specify the fluid properties, e.g., density crossing a boundary through an equation of state.

In contrast, a stagnation pressure condition assumes stagnation conditions outside the boundary so that the velocity at the boundary is zero. This assumption requires a pressure drop across the boundary for flow to enter the computational region. Since the static pressure condition says nothing about fluid velocities outside the boundary (i.e., other than it is supposed to be the same as the velocity inside the boundary) it is less specific than the stagnation pressure condition. In this sense the stagnation pressure condition is generally more physical and is recommended for most applications.

**- Outflow boundary conditions:** In many simulations there is a need to have fluid flow out of one or more boundaries of the computational region. At such "outflow" boundaries there arises the question of what constitutes a good boundary condition.

In compressible flows, when the flow speed at the outflow boundary is supersonic, it makes little difference how the boundary conditions are specified since flow disturbances cannot propagate upstream. In low speed and incompressible flows, however, disturbances introduced at an outflow boundary can have an effect on the entire computational region.

The simplest and most commonly used outflow condition is that of a “continuative" boundary. Continuative boundary conditions consist of zero normal derivatives at the boundary for all quantities. The zero-derivative condition is intended to represent a smooth continuation of the flow through the boundary.

It must be stressed that the continuative boundary condition has no physical basis; rather it is a mathematical statement that may or may not provide the desired flow behaviour. In particular, if flow is observed to enter the computational region across such a boundary, then the computations may be wrong because nothing has been specified about flow conditions existing outside the boundary.

As a general rule, a physically meaningful boundary condition, such as a specified pressure condition, should be used at out flow boundaries whenever possible. When a continuative condition is used it should be placed as far from the main flow region as is practical so that any adverse influence on the main flow will be minimal.

**- Opening boundary conditions:** If the fluid flow crosses the boundary surface in either directions an opening boundary condition needs to be utilized. All of the fluid might flow out of the domain, or into the domain, or a combination of the two might happen.

**- Free surfaces and interfaces:** If the fluid has a free surface, then the surface tension forces need to be considered. This requires utilization of the Laplace's equation which specifies the surface tension induced jump in the normal stress $p_s$ across the interface:

$$p_s = \sigma \cdot k \tag{4.89}$$

where$\sigma$ represents the liquid-air surface tension and *k* the total curvature of the interface. A boundary condition is required at the contact line, the line at which the solid, liquid and gas phases meet. It is this boundary condition which introduces into the model information regarding the wettability of the solid surface.

### 4.7.2 - Techniques for Numerical Discretization

In order to solve the governing equations of the fluid motion, the partial differential equation is written in a series of algebraic equation that the computer can be calculated.

There are various techniques for numerical discretization:

The finite difference method

**The Finite Difference Method:** In the Finite difference method, the derivatives of the variables in the equation of the fluid motion are represented through the Taylor series expansion at various points in space or time.

Consider two points, (*i+1*) and (*i-1*), a small distance $\Delta x$ from the central point, (*i*). The velocity $u_i$ can be expressed in terms of Taylor series expansion about point (*i*) as:

$$u_{i+1} = u_i + \left(\frac{\partial u}{\partial x}\right)\Delta x + \left(\frac{\partial^2 u}{\partial x^2}\right)\frac{\Delta x^2}{2} + \left(\frac{\partial^3 u}{\partial x^3}\right)\frac{\Delta x^3}{6} + ... \tag{4.96}$$

$$u_{i-1} = u_i - \left(\frac{\partial u}{\partial x}\right)\Delta x + \left(\frac{\partial^2 u}{\partial x^2}\right)\frac{\Delta x^2}{2} - \left(\frac{\partial^3 u}{\partial x^3}\right)\frac{\Delta x^3}{6} + ... \tag{4.97}$$

These equations are mathematically exact if numbers of terms are infinite and $\Delta x$ is small. Note that ignoring terms leads to a source of error in the numerical calculations (truncation error).

Looking at the (4.96) and (4.97), the first order derivative referred to a forward difference, can be formed as:

$$\left(\frac{\partial u}{\partial x}\right)_i = \frac{u_{i+1} - u_i}{\Delta x} - \left(\frac{\partial^2 u}{\partial x^2}\right)\frac{\Delta x^2}{2}. \tag{4.98}$$

the first order derivative referred to a backward difference:

$$\left(\frac{\partial u}{\partial x}\right)_i = \frac{u_i - u_{i-1}}{\Delta x} - \left(\frac{\partial^2 u}{\partial x^2}\right)\frac{\Delta x^2}{2}. \tag{4.99}$$

Similarly it is possible to obtain higher order approximation, by applying the Tailor series expansion for more points (second-order approximation with 3 point cluster, third order with 4 point, etc). For more discussion on this topic refer to Chapra et al. 1988.

**The Finite Element Method:** The finite element method (and the Finite volume Method) uses integral formulations that provide a more natural treatment of Neumann boundary condition, as well as that of discontinuous source terms due to their reduced requirements on the regularity or smoothness of the solution. Moreover, they are better suited than the finite difference method to complex geometries.

The fluid domain is divided into finite number of sub-domains (elements). A simple function (*W*) is assumed for the variation of each variable inside each element. The summation of variation of the variable in each element is used to describe the whole flow field.

**The Finite Volume Method:** The finite volume method is a special case of finite element, when the function *W* is equal to 1 everywhere in the domain. This technique was discussed in detail by Patankar (1980).

## 4.8 - Immersed boundary algorithms

In this work, the method adopted is the Immersed Boundary technique that was first used by Peskin (1972) to simulate cardiac mechanisms and associated blood flow.

The technique allows the solution of differential equations in complex geometric configurations on simple meshes by introducing forcing terms, variable in space and time, in correspondence of the regular grid of the physical location of the complex boundaries. Hence the simulations are performed on a much simpler mesh.

The basic idea consists in treating the fluid-boundary interface as a free surface and to impose over there pressure boundary conditions so that fluid particles can move only along the tangent to the boundary line.

As shown in Mittal et al. (2005), in immersed boundary algorithm for Newtonian and incompressible fluids, the Navier - Stokes equations are:

$$\begin{cases} \dfrac{Du}{Dt} = -\nabla P + \dfrac{1}{Fr^2} \cdot \tilde{\rho} \cdot \nabla \hat{z} - \dfrac{1}{\mathrm{Re}} \nu \cdot \nabla^2 u + f \\ \nabla \cdot u = 0 \\ \dfrac{DC}{Dt} = -Pe \cdot \nabla^2 C \end{cases} \quad \text{in}\, \Omega_f \qquad (4.100)$$

with

$$\vec{u} = \vec{u}_\Gamma \qquad \text{on} \qquad \Gamma_b \qquad (4.101)$$

where $\Gamma_b$ is the boundary of the solid body and $\Omega_f$ is the domain of the surrounding fluid,

and

$$Pe = \frac{U \cdot L}{D} \qquad Fr = \frac{U}{\sqrt{\dfrac{\Delta\rho}{\rho_0} g \cdot L}} \qquad \mathrm{Re} = \frac{U \cdot L}{\nu} \qquad (4.102)$$

where, apart from the nondimensional numbers already cited (Froude and Reynolds), the Peclet number represents the ratio between the advective transport rate, (in the equations (4.102): *L* is the characteristic length scale, *D* is the mass diffusion and diffusive coefficient and *U* is the velocity, $\Delta\rho$ is the difference of density from the discharged fluid and the surrounding fluid $\rho_0$, $\nu$ is the kinematic viscosity and *g* the acceleration of gravity).

The forcing terms $f = \left(\vec{f}_m, f_p\right)$ are $\vec{f}_m$ for the function applied to the momentum, and $f_p$ applied to the pressure, and can be imposed on the regular mesh.

A possible expression of the forcing terms was derived by Mohd-Yusof (1997), if Equation (4.100) is discretized in time:

$$\frac{\vec{u}^{l+1} - \vec{u}^{l}}{\Delta t} = RHS^{l+1/2} + f^{l+1/2} \qquad (4.102)$$

where $RHS^{l+1/2}$ contains the convective and viscous terms, the pressure gradients and the sub-grid terms.

Under the 4.102, the value of $f^{l+1/2}$ that leads $\vec{u}^{l+1} = V^{l+1}$ on the immersed boundary:

$$f^{l+1/2} = -RHS^{l+1/2}\Delta t + \frac{V^{l+1} - \vec{u}^{l}}{\Delta t} \tag{4.103}$$

This forcing is called direct forcing, because the velocity value is imposed directly on the immersed boundary like a boundary condition independently of the flow conditions.

# Chapter 5

# Experimental set-up

## 5.1 - Introduction

According to Avanzini et al. (2006), a diffuser is "a section of the outfall with a series of holes in the wall which spread out the untreated or treated waste water" (figure 5.1).

**Figure 5.1Photograph of a diffuser (Avanzini et al. 2006)**

Following the above definition, the experimental set-up used in the present research represents a fraction of a pipe laid down on the sea floor, which discharges the effluent from the orifices along the pipe wall.

The effluent can be lighter than the receiving body, which is usually referred as a Positive Buoyant jet (domestic wastewater treatment plants). If the effluent is denser, then it is usually called a Negative Buoyant jet (brine from desalination plants).

## 5.2 - SET - UP

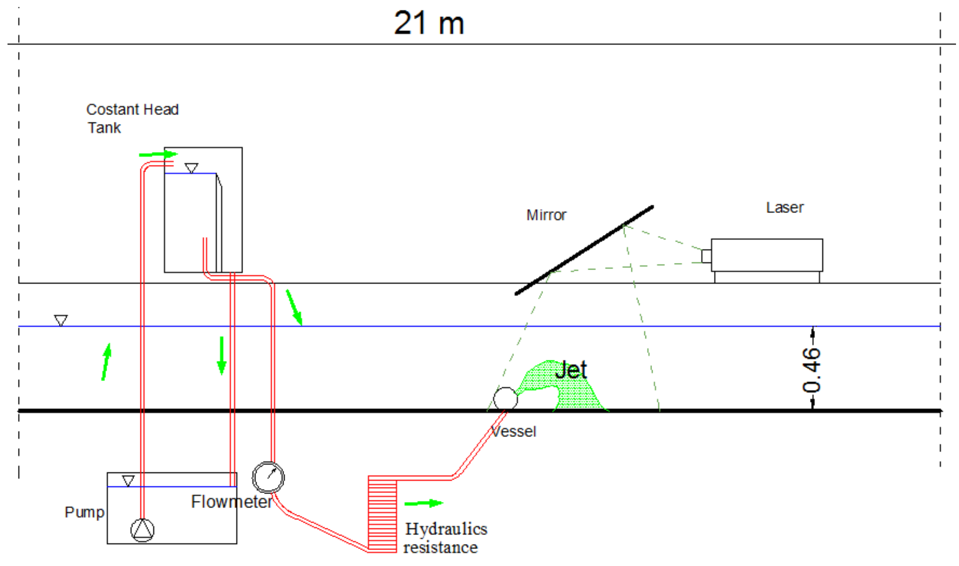


Figure 5.2Sketch of the experimental set-up

The model (shown in figure 5.2 and 5.3) consists of a 21m long and 30 cm wide flume with glass walls. It is filled with 46 cm of water (enough to avoid the interaction between the jet and the free surface) which is at rest to simulate a stagnant receiving body. It has a flat bottom to have the shortest path available for the jet dilution. The thickness of the walls is 2 cm and the flume is reinforced and supported by a steel framework.

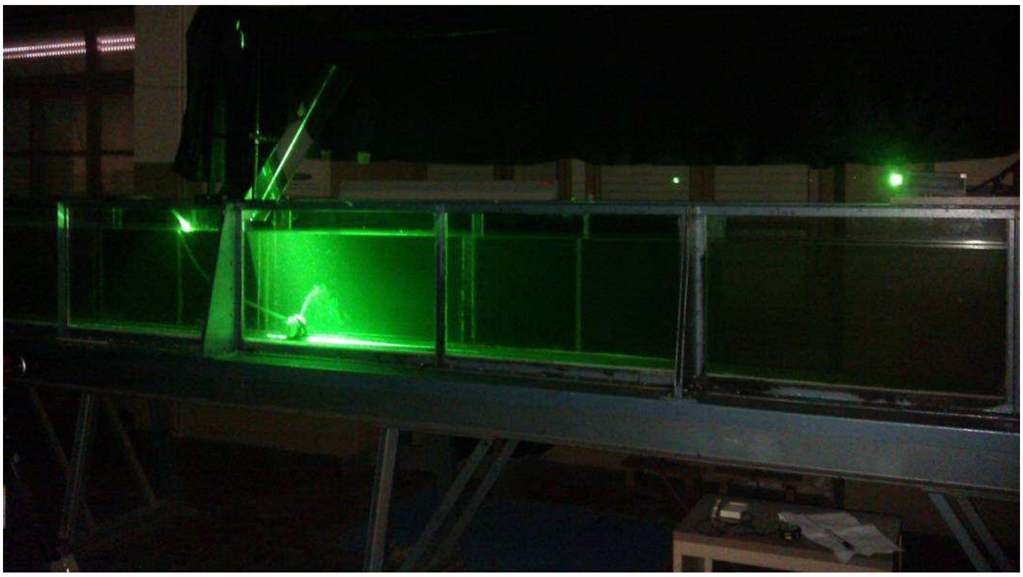

Figure 5.3 Picture of the Experimental volume

The fluid is injected through a pipe, which is connected to a constant head tank by a cylindrical vessel of 0.10 m diameter, with a sharp-edge orifice of diameter D = 4 mm on its side wall (figure 5.4 and 5.5).

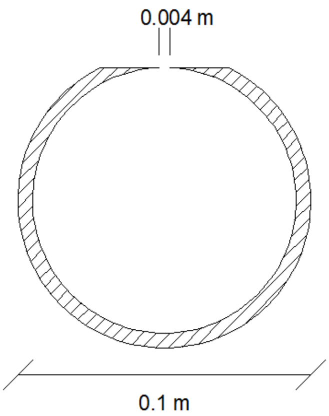


**Figure 5.4 Section of the diffuser**

The released fluid is a solution of water, sodium sulphate (to increase the density), pollen particles (around 50 μm of diameter to measure the velocity fields by Feature Tracking Velocimetry (FTV) technique (figure 5.6)), and titanium dioxide to perform Light Induced Visualization (LIV) (figure 5.7).

A separate storage tank was used to store the solution that is pumped by using a submersible pump in a constant head tank. The overflow is conveyed in a drain chamber, and then falls back in the storage tank.

**Figure 5.5 Picture of the constant head tank**

To measure the flow rate, a calibrated flow-meter was installed between the constant head tank and the diffuser. The measured data were recorded by a National Instruments data acquisition unit.

**Figure 5.6 Snapshot of a negatively buoyant jet, with a densimetric Froude number of 15 and a release angle of 65°on the horizontal, seeded with pollen particles for the FTV analysis.**

**Figure 5.7 Snapshot of a negatively buoyant jet, with a densimetric Froude number of 15 and a release angle of 65°on the horizontal, for the LIV analysis.**

# 5.3 Accessories

## 5.3.1. Flow Meter


**Figure 5.8 RAKD flow rotameter**

The flow rate was measured every 0.1 seconds with a flow rotameter (figure 5.8) connected to a computer through a National Instrument data acquisition card. The accuracy is 4%. The flow rate was recorded by linking the rotameter with a National instrument data acquisition card.

### 5.3.2. Submersible Pump

In order to pump the solution from the storage tank to the constant head tank, a submersible pump was used.

This pump allows a very low heating of the solution and provides the head strictly necessary to reach the constant head tank.

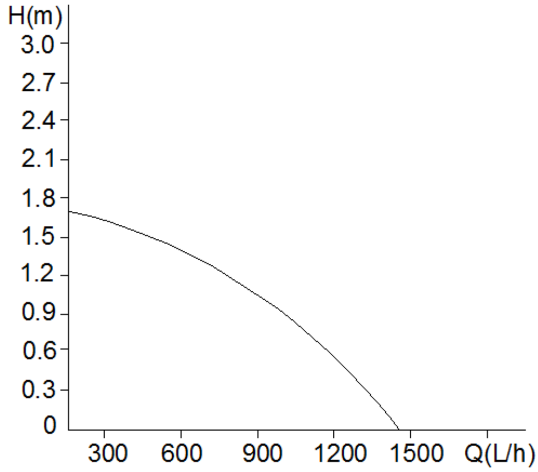


**Figure 5.9 Characteristic diagram of the pump**

This kind of pump has plastic contact surfaces, i.e. it was chosen in order to avoid corrosion.

### 5.3.3. Laser

The middle vertical section was lighted with a laser, that emits monochromatic light with high energy density, and it is conveyed into a 1 mm thick light sheet.

The power peak is 10 W and the wave length is between 501 nm - 561 nm.

The laser material consists of a semiconductor (diode), excited (pumped) by the introduction of electromagnetical energy.

The light sheet is produced by cylindrical lens.

### 5.3.4. Camera

To record the images, a Bonito High-speed High-resolution CMOS Camera was used.


Figure 5.10High speed camera

The camera runs at 386 fps at 4 Megapixel resolution (2320 x 1726 pixels) and has an ultra-fast 2 x 10-tap Camera Link that transmits the images to two frame-grabbers, which save the images in the RAM of the computer.

At the end of the recording, all the sets of pictures are saved in a solid state disk.

## 5.4 Experimental procedure

Before the experiments, the long flume and the storage tank were cleaned; the first was filled with tap water, while the second with a solution of water and sodium sulphate, approximately 24 hours before the measurements to ensure the condition of stagnant water and to avoid temperature differences. Near the discharge, the ambient fluid was seeded with tracer particles to allow the velocity measurements. A few hours before the experiment, the solution and the water of the test tank were controlled by a density meter and, if necessary, the density was corrected by adding sodium sulphate.

Subsequently, the laser sheet was aligned with the middle vertical section passing through the orifice, moving the window and/or the laser (figure 5.11). The camera focus was adjusted and a picture of a reference ruler was captured to obtain the scale factor.

The experiment was performed with Froude number ranging from 8 to 34, release angle of $\theta$ = 35°, 65° and 80°to the horizontal axis, and a Reynolds number of 1000, which was found to be larger than the critical Reynolds number by Ferrari et. al (2010).

Before each test, 1500 frames of the background were recorded; afterwards, the solution was released and, when a steady flow state was established, the phenomenon was recorded by the high speed video camera having a frequency of 400 fps, and a spatial resolution of 2280 × 1728 × 8 bit. A minimum of 4000 independent image couples were acquired.

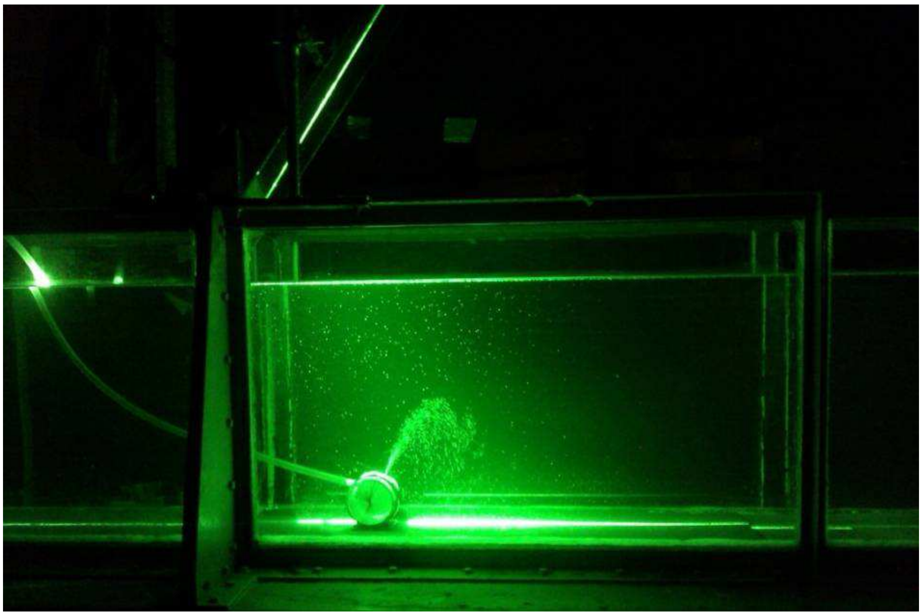

Figure 5.11 Snapshot of the jet during operation

# Chapter 6

# Image analysis algorithms for velocity detection

## 6.1 - Introduction

By means of image analysis techniques, i.e. non-intrusive techniques, it is possible to obtain quantitative information about the flow (velocity or concentration) in all the field of investigation, and not only in one point like traditional instruments (hot-wire and laser Doppler) without perturbing the flow. This allows taking measurements in flows where the presence of probes could eventually disturb the velocity field (boundary layers or high-speed flows).

To determine the velocity field, the fluid is accurately seeded with neutrally buoyant particles, which are supposed to accurately follow the motions of the fluid.

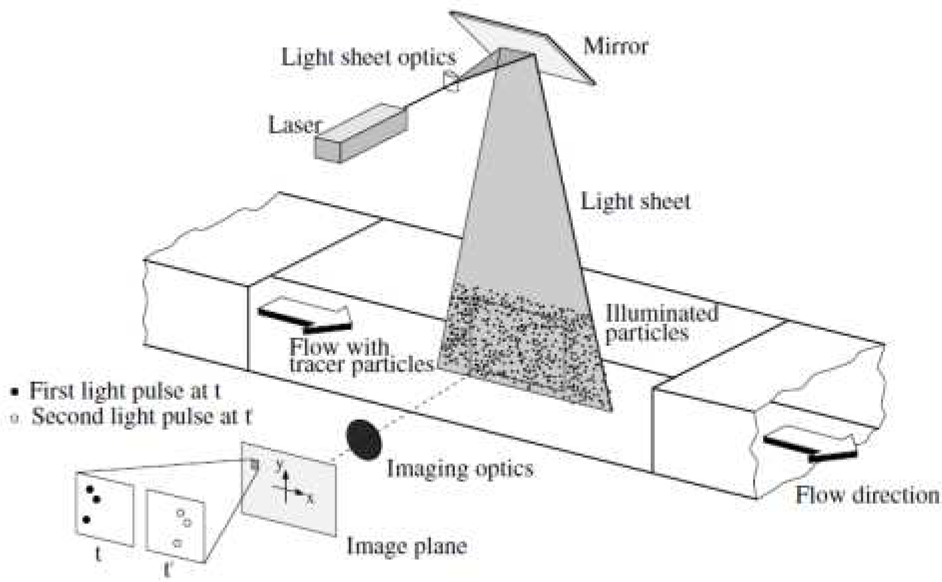


**Figure 6.1 Experimental setup necessary to implement for the Particle Image Velocimetry (Raffel et al 2007)**

## 6.2 – Image Analysis models

The experimental setup of an image analysis system (figure 6.1) consists of:

- an optical transparent test-section seeded with tracer particles,
- a light source (laser), continued or pulsed, to illuminate the test-section,
- a recording setup or a CCD camera,
- an image analysis algorithm to determine the velocity fields.

The image analysis models can be classified as: single frame methods, where the flow is captured in a single image (figure 6.2), or multi-frame method, in which every capture is recorded in a different image (figure 6.3).

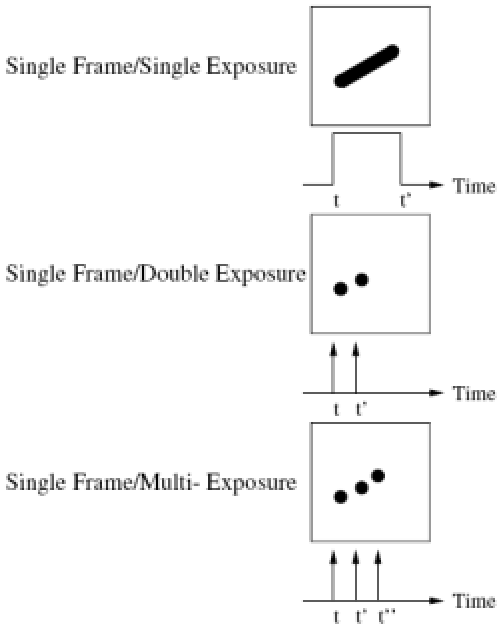


**Figure 6.2 Single–frame techniques (Raffel et al 2007)**

The first technique causes an ambiguity of the direction of the flow, because recording on the same image does not retain the information of the temporal direction. It is necessary to use pulse tagging or colour coding (by means of rotating mirror or birefringent crystal).

In single exposure techniques (figure 6.3), the shutter on the sensor opens to admit the first pulse, and the image is recorded in a first frame, then the shutter opens again to admit the second pulse, and the image is recorded in the second frame. In this case, each frame contains images from either the first pulse or the second, but not both (except for the multi-frame/double-exposure).

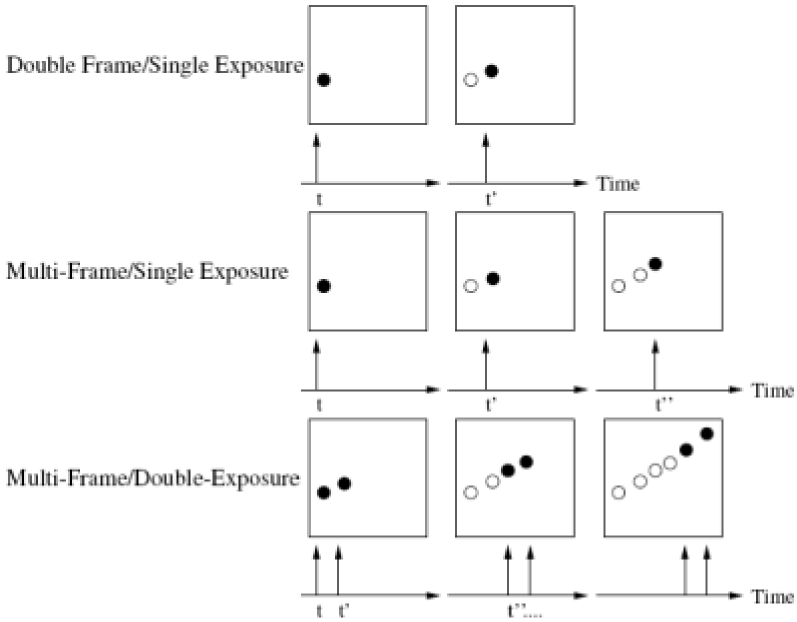


**Figure 6.3 Multi–frame techniques (Open circles indicate the particle position in the previous frames) (Raffel et al 2007)**

## 6.3 – Tracer Particles and particle image diameter

The tracer particles added to the fluid should have some requirements:

- follow exactly the motion of the fluid,

- not interact with each other,

- not alter the behaviour of the flow.

In this case, the particles are called "ideal". In practical situations, it is possible only to approximate a particle like an "ideal" one, and it is necessary not only to consider the dynamic response of the tracer, but also the scattering of light.

The importance of the optimization of the diameter of the particles is due to its connection to the error in velocity detection, i.e. a small image particle creates uncertainty in the identification of the centroid and consequently on the correlation peak centroid. Another important reason is related to the particle image intensity (I), the light energy per unit area increases quadratically with decreasing image areas.

For the identification of the diameter of the image particles, it is necessary to take their diffraction into account.

Considering a plane light waves having wavelength $\lambda$ impinge on an opaque screen containing a circular orifice of diameter $D$ and distant $z_0$, it is possible to define the Fraunofer number as:

$$F = \frac{D^2}{\lambda \cdot z_0} \qquad (6.1)$$

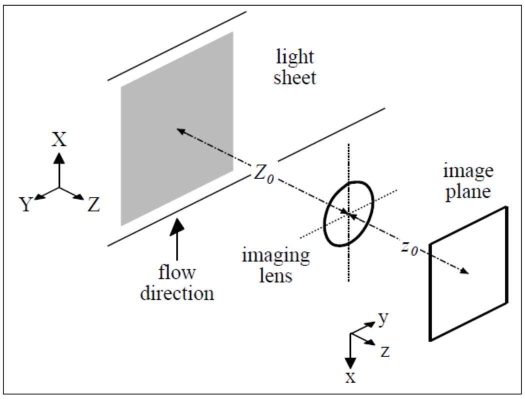


**Figure 6.4 Schematic representation of the imaging set-up in PIV (Westerweel 1993)**

If the distance of the point source is large (F<<1), a circular pattern, called "Airy disk", will be obtained for low exposure (figure 6.5).

The light intensity distribution follows the behaviour shown in the figure 6.6 and the law of

$$\frac{I(x)}{I_{\max}} = A_i\left(\frac{x}{\delta}\right), \qquad (6.2)$$

where $x$ is the distance from the centre of the aperture, $I_{max}$ is the maximum light intensity. $\delta$ is

$$\delta = \frac{\lambda}{\pi}\frac{z_0}{D}. \qquad (6.3)$$

$A_i$ is the Airy function, which is equivalent to the square of the first order Bessel function.

The diameter of the Airy disk is the smallest particle image that can be obtained in a PIV configuration. It can be shown (see Raffel et. al, 2007 for more details) that the minimum image diameter is (due to the diffraction)

$$d_{diff} = 2.44 \cdot f_{\#}(M+1) \cdot \lambda, \qquad (6.4)$$

where $f_{\#}$ is the f-number defined as the ratio between the local length $f$ and the aperture diameter $D$.$M$ is the magnification factor (the ratio of the distance between the lens and the object plane ($z_0$. and $Z_0$) and the distance between the lens and the object plane respectively).

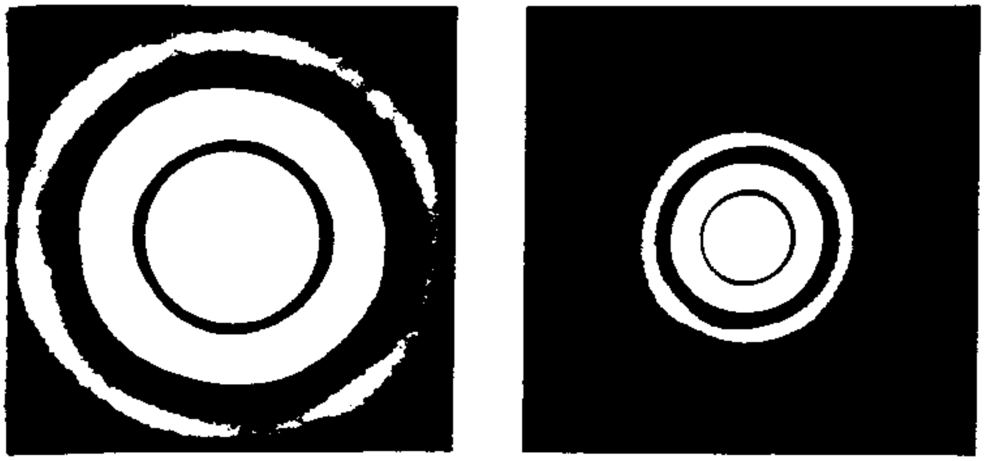

**Figure 6.5 Airy patterns for a small (left hand side) and a larger aperture (right hand side) (Raffel et al, 2007)**

The minimum particle image diameter is then calculated as

$$d_\tau = \sqrt{(M \cdot d_P)^2 + d_{diff}{}^2} \tag{6.5}$$

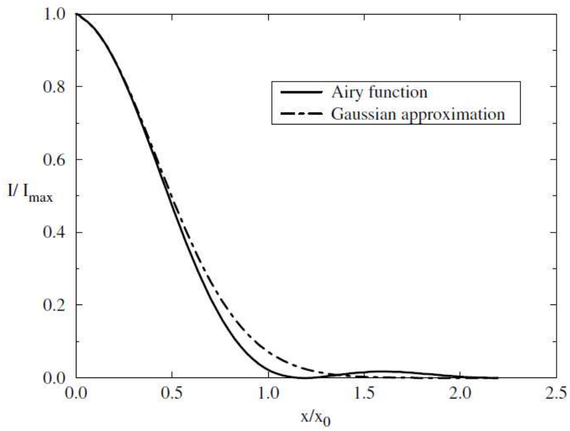


**Figure 6.6 Normalized intensity distribution of the Airy pattern and its approximation by a Gaussian bell curve (Raffel et al, 2007)**

As shown in the figure 6.6, the Airy function can be well approximated with a Gaussian function

$$\frac{I(x)}{I_{\max}} = \exp\left(-\frac{x^2}{2\sigma^2}\right), \tag{6.6}$$

where

$$\sigma = \frac{f_\#(1+M)\lambda\sqrt{2}}{\pi}. \tag{6.7}$$

Generally, in the image analysis algorithm a Gaussian distribution is used instead of the Airy function. This simplification allows remarkable reduction of the time consuming on the computing of the maximum spatial correlation, and hence on the computation of the particle displacements.

## 6.4 – Density of tracer particle images

In the literature particle density is often represented by two dimensionless parameters (Adrian and Yao, 1984): image particle density ($N_I$) and source density ($N_S$)

$$N_I = n_p \cdot \Delta z \cdot \frac{\pi}{4}\left(\frac{d_{\text{int}}}{M}\right)^2 , \tag{6.8}$$

$$N_S = n_p \cdot \Delta z \cdot \frac{\pi}{4}\left(\frac{d_I}{M}\right)^2 , \tag{6.9}$$

where $n_P$ is the number of particles, $\Delta z$ is the thickness of the light sheet, $M$ is the magnification factor, $d_I$ is the diameter of the particles and $d_{int}$ is the diameter of the interrogation area.

$N_I$ represents the ratio of the length of the particle's tracks between successive illuminations and the distances between individual particles.

The source density ($N_S$) represents whether the particle images are overlapping ($N_S$>1) or can be recognized individually ($N_S$<1).

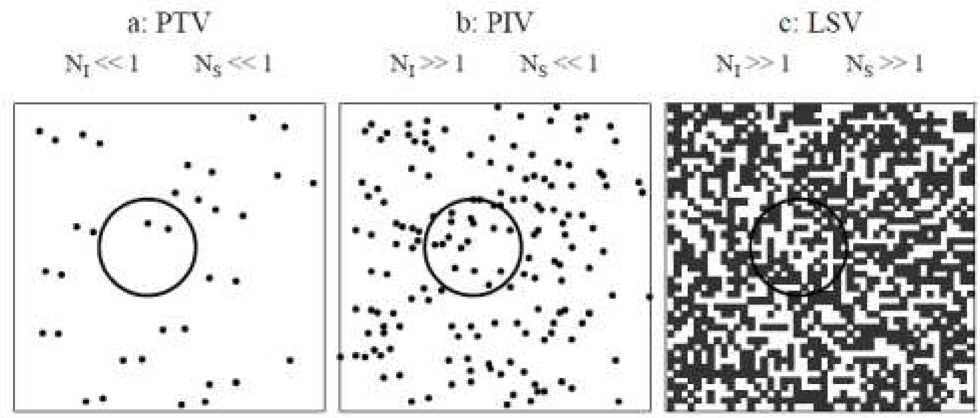


**Figure 6.7 Different image analysis techniques in relation to the different seeding density (Westerweel 1993)**

According to the value of the dimensionless parameters, it is possible to define three different models (figure 6.7):

- Particle tracking velocimetry (PTV): $N_S$<< 1, $N_I$<< 1
- Particle image velocimetry (PIV) : $N_S$<< 1, $N_I$>> 1

- Laser speckle velocimetry (LSV) : $N_S$>> 1, $N_I$>> 1

The images in PIV and LSV are analyzed in the same way; therefore it is possible to define two different procedures to extract the velocity from images. The typical assumption is that particles move between one frame to the other conserving their brightness (Falchi et al 2006).

In the PTV, the particle positions in the images are firstly identified and then the particles of the two subsequent images are associated. In PIV and LSV, a part of the first image is compared to the subsequent ones.

## 6.5 - Particle tracking velocimetry (PTV)

In PTV the average distance between two different particles is much larger than the mean displacement in two subsequent frames.

If the particles are illuminated by two subsequent flashes of light, each particle produces two images on the same film. The velocity is obtained by dividing the distance of the two images by the time difference between the two flashes.

To detect the position of the particles: the process is based on applying one or more thresholds on the images. The particles appear as connected sets of bright pixels, as the particle position, usually, is associated the barycentre of these pixels (if the result of the threshold is a binary image) or its grey scale centre of mass (if the threshold save all the values above it).

Another method sometimes used for particle detection is to fit a Gaussian intensity distribution of the particle image and to calculate its centre as the mean value of the Gaussian. Both of these methods have sub-pixel accuracy. Grey scale centre of mass and Gaussian fit work on the assumption, true only on ideal particle images that the position of the particle centre corresponds to the position of the maximum in the image intensity distribution.

To link positions of particles at time *t+1* that matches certain criteria with those at time *t*, the tracking procedure is obviously different if one has knowledge of the previous motion of the particle or not: in the first case, the earlier information can be used to predict a new position of the particle at time *t+1* and look for particle positions in the search area around this position; in the second case, no prevision can be done and the search radius has to be of the same order of the maximum presumed displacement. Particle tracking is so carried on by looking for temporal series of particle locations that fulfil the criteria of: distance between two successive locations less than a given parameter; difference between two successive displacements less than a second given parameter. While the first condition corresponds to a known/assumed maximum velocity in the investigated flow, the second is equivalent to an assumed maximum acceleration. This last criterion can be relative to the turbulent parameter of the flow. In the case of an ambiguity due to the presence of more than one particle in the search area, a solution can be to assume that the time interval between images is small enough to use a minimum variation criterion; as a consequence, the particle closer to the predicted position is supposed to represent the continuation of the trajectory. If a linear prediction is used, this corresponds to validate the trajectory with minimum acceleration.

There are a few limitations in the method.

Consider a square domain of D × D pixels having length L. The field is seeded with particles of diameter $d_p$ and three times exposed at time intervals of Δt (figure 6.8)

The direction of the velocity coincides with the trajectory; the module is computed dividing the distance between the first and the third position for 2·Δt where Δt is the time interval between the two expositions. In the multi-exposed images, it is not possible to determine the direction of the velocity, but it is to infer by the general direction of the flow, that is supposed to be known a priori. The minimum displacement detectable is L/D, consequently, the minimum velocity that is possible to be detected is

$$v_{\min} = \frac{L}{D \cdot \Delta t} \quad . \tag{6.10}$$

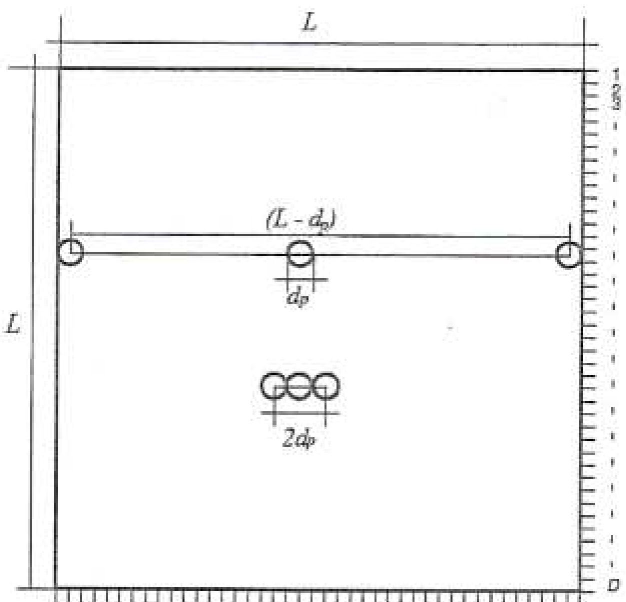


**Figure 6.8 Field of investigation (Querzoli 1995).**

The maximum velocity that is possible to be detected is the velocity in which the particle covers the entire length of the field (L):

$$v_{\max} = \frac{\left(L - d_p\right)}{2 \cdot \Delta t}. \tag{6.11}$$

In this algorithm, it is easy to identify particle-image pairs, however it is not possible to determine the local velocity in any arbitrary position, but only where the particles are present.

## 6.6 Particle image velocimetry (PIV)

### 6.6.1 Optical considerations

In the Particle Image Velocimetry it is still possible to identify individual particles ($N_S$<<1). In correlation-based PIV the interrogation window contains a sufficient number of particles to determine the local average of the flow velocity.

As shown in Raffel et al. (2007), for infinite small geometric particle images, the particle image intensity distribution (intensity profile) is given by the point spread function of the imaging lens τ(x) that is assumed to be Gaussian:

$$\tau(x) = \frac{8\tau_0}{\pi d_\tau^{\,2}} \exp\left( -\frac{8|x|^2}{d_\tau^{\,2}} \right). \tag{6.12}$$

Therefore, the image intensity field can be expressed as the convolution product of *τ(x)* with the geometric image of the tracer particle at position $x_i$. To describe the geometric part of the particle image, the Dirac delta-function is used

$$I = I(x,\Gamma) = \tau(x) * \sum_{i=1}^{N} V_0(X_i)\delta(x - x_i), \tag{6.13}$$

where $V_0(X_i)$ is the transfer function giving the light energy of the image of an individual particle, *i* inside the interrogation volume and its conversion into an electronic signal or optical transmissivity.

Equation 6.13 can be alternatively written as (see Raffel et al. 2007 for a deeper explanation):

$$I(x,\Gamma) = \sum_{i=1}^{N} V_0(X_i)\tau(x - x_i). \tag{6.14}$$

The image is divided into interrogation windows, and the correlation function is computed for each one, determining one displacement vector per window (figure 6.9). The interrogation window is generally square-shaped and sufficiently small to assume the direction and velocity of the particles to be uniform.

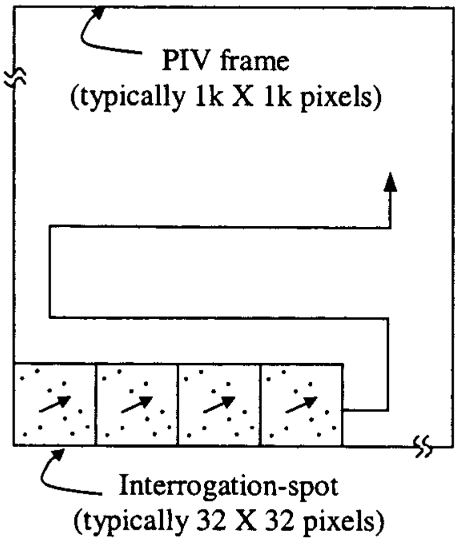


**Figure 6.9 Correlation-based PIV (Prasad 2000)**

The determination of the average particle's displacement is obtained by calculation of the auto-correlation or the spatial cross-correlation of the particle images.

### 6.6.2 Autocorrelation and multi-exposed images

The auto-correlation, R(S), is used in case of single-frame/double-exposure, and for an intensity pattern, I(X), of an interrogation window, **Ω**. It is given by

$$R(S)=\int_{\Omega} I(X)I(X+S)dX \tag{6.12}$$

The calculation of Equation (6.12) is excessively expensive; therefore the auto-correlation is computed using two-dimensional Fast Fourier Transform (FFT) of the digitized intensity pattern:

$$R(S) = I(X)\star I(X) = I(X)*I(-X), \tag{6.13}$$

where $\star$ is the correlation operator and * is the convolution operator.

Using the convolution theorem:

$$F\{R(S)\}=F\{I(X)\}\cdot F^*\{I(X)\}=\left|F\{I(X)\}\right|^2, \tag{6.14}$$

where *F* is the Fourier transform. Therefore,

$$R(S)=F^{-1}\left\{\left|F\{I(X)\}\right|^2\right\}. \tag{6.15}$$

In Figure 6.10a a computer generated 64 × 64 interrogation window is shown (Prasad, 2000); it is evident that some particles overlap, and others are truncated. The subsequent auto-correlation field (figure 6.10b) displays the tallest peak in the origin, that corresponds to the self-correlation peak, and two smaller peaks ($S^+$ and $S^-$), the location of the signal peak with respect to the self-correlation peak provides the x and y components of the displacement.

The auto-correlation function is rotationally symmetric, therefore the presence of the two smaller peaks, and the signal located at $S^+$ ($S_x$ and $S_y$), is replicated identically at $S^-$ ($-S_x$ and $-S_y$) leading a directional ambiguity of the velocity vector. This can be tolerated if the direction of the flow is known a priori, otherwise the use of particular schemes is necessary to solve general flows; for example translating the flow field (or the camera), or using oscillating mirrors, etc.

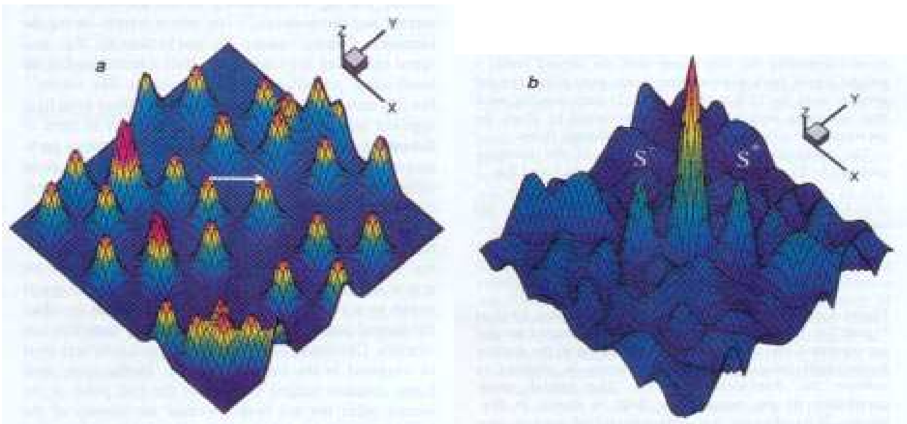


**Figure 6.10 Spatial auto-correlation of I (a) Particle image field; (b) Auto-correlation field (Prasad 2000)**

From figure 6.10b it is evident that the maximum velocity, which is possible to identify, is the half dimension of the interrogation window. Actually, due to the signal-to-noise ratio (SNR) it begins to degrade for particle displacement bigger than 1/4 of the interrogation window size, due to the inplane loss-of-pairs (see Prasad (2000) for a deeper explanation).

### 6.6.3 Cross-correlation and single-exposed images

The preferred choice is to use a multi-frame/single-exposure recording technique. In this case each frame contains images from only one pulse; therefore the process of cross-correlating of the two frames contains only one peak, without directional ambiguity.

The cross-correlation function, *C(S)*, of the Intensity patterns, $I_1(X)$ and $I_2(X)$, of two interrogation windows 1 and 2, is:

$$C(S) = \int_{\Omega} I_1(X) I_2(X+S)\, dX \,. \tag{6.16}$$

It can be shown that, using FFT

$$C(S) = F^{-1}\{F\{I_1(X)\} \cdot F^*\{I_2(X)\}\}. \tag{6.17}$$

As shown in the figure 6.11, the first and the second images are separated into two different frames (a and b), the spatial cross-correlation (c) shows the disappearing of the self-correlation peak, and consequently the duplicate signal peak. Another benefit is an improvement in the SNR compared to the auto-correlation.

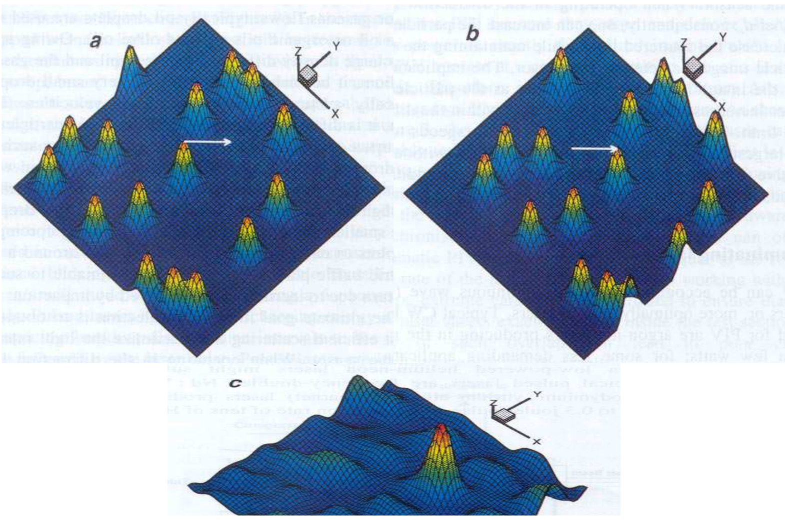


**Figure 6.11 Spatial cross-correlation between $I_1$ and $I_2$ (a) Particle image field 1; (b) Particle image field 2; (c) Cross-correlation field (Prasad 2000)**

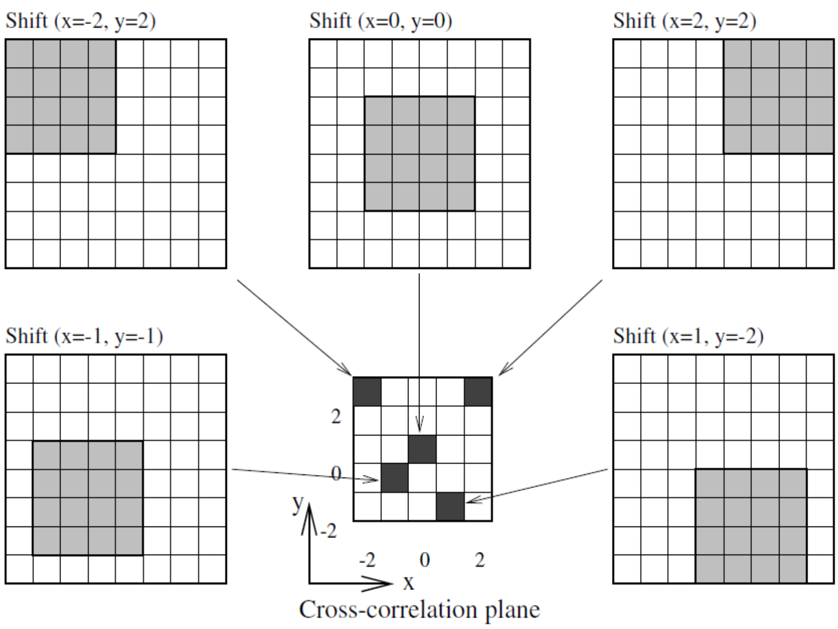


**Figure 6.12 Example of the formation of the correlation plane by direct cross-correlation (Raffel et al. 2007)**

One of the most used schemes for the displacement detection, as shown graphically in the figures 6.12 and 6.13, is to shift around the template $I_1$ in the sample $I_2$. For each sample shift, one cross-correlation value is produced. Therefore, the cross-correlation measures a sort of degree of match between the two samples; the highest value can be used as a direct estimator to determine the particle image displacement.

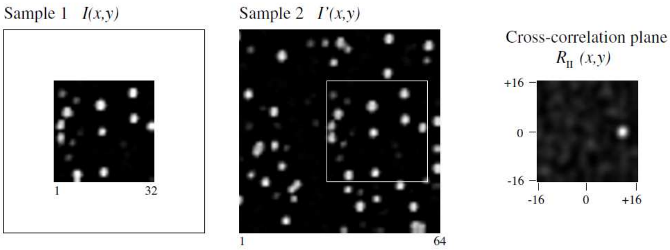


**Figure 6.13 Example of the formation of the correlation plane by direct cross-correlation, for real data, correlating a smaller template I (32 × 32 pixel), with a larger template I' (64 × 64 pixel) (Raffel et al. 2007)**

### 6.6.4 Displacement estimation

For the determination of the location of the correlation peak (and consequently of the displacement), a variety of methods were used in the past.

The centre of gravity method (ratio of the first order and zero-th order moment) is frequently used, but requires a threshold which separates the correlation peak from the background noise. In this method, the presence of a local maximum is not assumed, and it works well where more values contribute to the moment calculation, but in some cases, separating the noise and the peak is not easy.

The displacement Δx in the x direction and Δy in the y direction, for a discrete peak located at $x_0$, $y0$ is:

$$\Delta x = \frac{\sum_{i,j}\left(x_{i,j} - x_0\right)R_{(i,j)}}{\sum_{i,j} R_{(i,j)}}, \tag{6.17}$$

$$\Delta y = \frac{\sum_{i,j}\left(y_{i,j} - y_0\right)R_{(i,j)}}{\sum_{i,j} R_{(i,j)}}. \tag{6.18}$$

A more robust method is to fit the correlation data to some function using only three adjoining values to estimate a component of displacement. The most common of these three-point estimators is the Gaussian peak, because the Gaussian intensity distribution approximates well the Airy function (see section 6.6.1).

$$f(x) = C \cdot \exp\left[\frac{-(x_0 - x)^2}{k}\right], \tag{6.19}$$

$$\Delta x = \frac{\ln R_{(i-1,j)} - \ln R_{(i+1,j)}}{2\ln R_{(i-1,j)} - 4\ln R_{(i,j)} + 2\ln R_{(i+1,j)}},$$

$$\Delta y = \frac{\ln R_{(i,j-1)} - \ln R_{(i,j+1)}}{2\ln R_{(i,j-1)} - 4\ln R_{(i,j)} + 2\ln R_{(i,j+1)}}.$$

This estimator works well for rather narrow correlation peaks formed from little particle images (2-3 pixel diameter range) (see Raffel et al. (2007) for the explanation).

### 6.6.5 Optimization consideration

As shown in Kean et al. (1991), to optimize the performance for multi-pulsed system, the following criteria are recommended:

- number of particle images per interrogation window more than 15;
- the in-plane displacement $|\Delta x| d_I \leq 0.25$ ($d_I$ is the dimension of the interrogation window);
- the out-of-plane motion $|w|\Delta t/\Delta z_0 \leq 0.25$ (where $\Delta z_0$ is the thickness of the light sheet);
- the velocity gradient in each interrogation window, less than 5% of the mean velocity

## 6.7 – Feature Tracking Velocimetry Algorithm

### 6.7.1 Introduction

The algorithm used in this work for the velocity detection in NBJs is a novel algorithm, called Feature Tracking Velocimetry (FTV).

The investigated jets are characterized by inhomogeneous seeding density (due to the difficulty of uniformly disperse tracers in the environmental fluid and effluent), high velocity gradient (in particular in the jet-ambient interface), and high out-of-plane velocities, therefore it is necessary for an algorithm to be more robust. It can be accurate where other techniques produce significant errors. It is less sensitive to the appearance and disappearance of particles, and to the density of insemination (from the PTV to the PIV levels).

As recalled in the previous section, PIV algorithms calculate velocity fields comparing windows of successive frames on a regular grid using the cross-correlation to measure the degree of matching. The idea of FTV is to compare windows only where the motion detection may be successful, that is where there are high luminosity gradients.

In particular, the procedure consists of:

1. identification of the features using the Harris Corner detection (figure 6.15, 6.16), a corner is a region with high luminosity gradients along the x and y direction (Harris & Stephens, 1988);
2. ordering of the features according to their cornerness (i.e. the value of the Harris formula);
3. selection of the first N features and computation of velocity comparing a window centred with the $i^{th}$ feature ($W_t$) with windows ($W_{t+1}$) with a range of displacements, ($d_i$, $d_j$) in the next frame;
4. for each displacement, a measure of the dissimilarity, $d(d_i, d_j)$, between $W_t$ and $W_{t+1}(d_i, d_j)$ is computed using the Lorentzian estimator; the velocity is obtained as the displacement minimizing the dissimilarity;
5. eventually, samples are validated by means of algorithm based on Gaussian filtering of first neighbours (defined by the Delaunay triangulations), and simulated annealing.

### 6.7.2 Harris-Corner detector

The Harris corner detector was used to identify the luminosity gradients, related to the presence of particles. The knowledge a priori of the particle's position allows the computation of the displacements only where particles are present, allowing a reduction of the computational costs and the presence of spurious vector due to the absence of particle images.

Considering the intensity variation for a shift Δx and Δy, the Harris corner formula is

$$E(x,y) = \sum_{x,y} w(x,y)\left[I(x+\Delta x, y+\Delta y) - I(x,y)\right]^2 , \qquad (6.20)$$

where *I(.,.)* is the image function and *W(x,y)* is the window function, that can be median or Gaussian.

In the FTV algorithm, *w(x,y)* is assumed to be a Gaussian function (see section 6.3), with dimensions related to the diameter of the image particle.

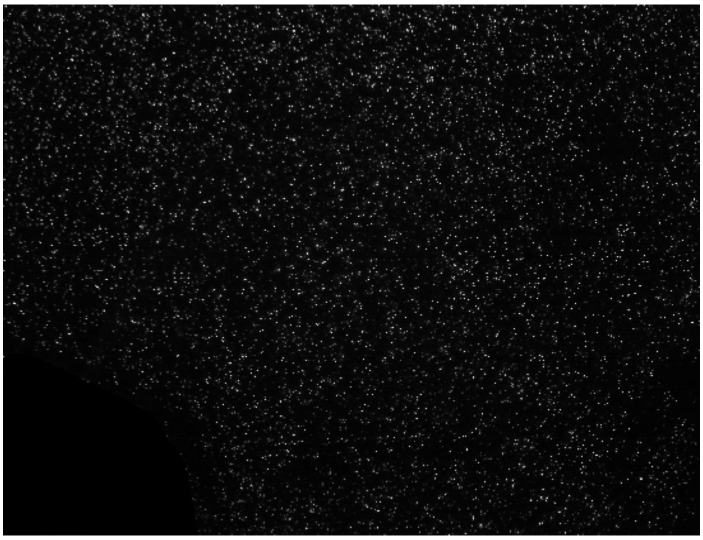

**Figure 6.14 Snapshot of a negatively buoyant jet, with a densimetric Froude number of 15 and inclination of 65°, seeded with pollen particles.**

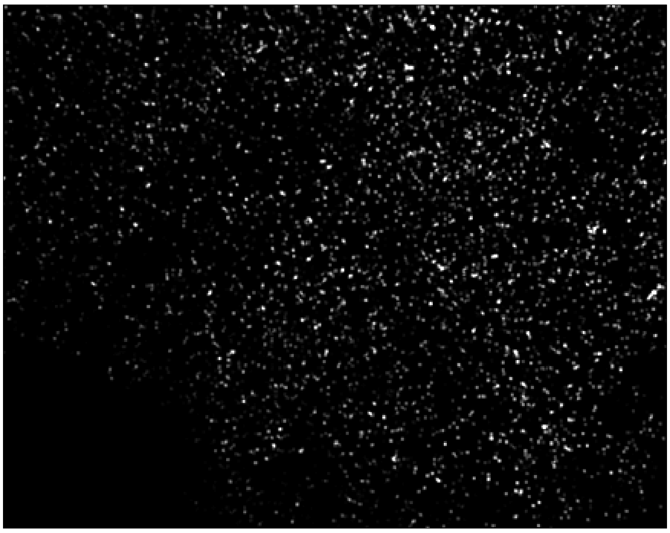

**Figure 6.15 Corner metric in the figure 6.14**

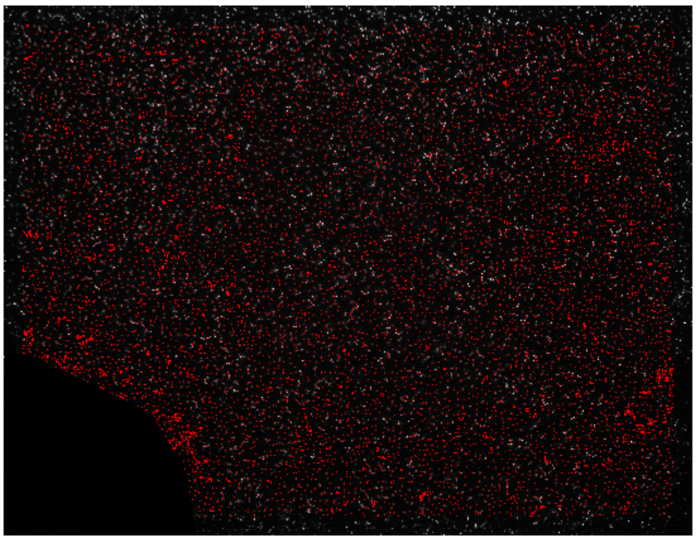

**Figure 6.15 Corner point (red point) in the figure 6.14**

### 6.7.3 Dissimilarity Measure

Differently from the classical PIV that uses cross-correlation to determine the displacements, the Lorentzian Estimator is used in the Feature Tracking Velocimetry algorithm:

$$\rho(\Delta) = \ln\left(1 + \left(\frac{\Delta}{\sigma_e}\right)^2\right), \qquad (6.25)$$

where $\sigma_e$ is a tuned parameter that corresponds to the expected standard deviation of the pixel-intensity differences, $\Delta$ corresponds to the pixel intensity difference for a given displacement.

The Lorentzian estimator is a robust estimator introduced in the computer vision by Black and Anandan (1991) and in fluid velocimetry by Falchi et al. (2006). The importance of this estimator is that, while comparing the interrogation windows of two successive images, it gives more importance to the similar pixels, while too much different pixels are rejected (for example due to the appearance or disappearance of particles). This is due, as shown in figure 6.16, to the lower growth of the Lorentzian estimator with respect to the pixel intensity difference compared to a quadratic estimator.

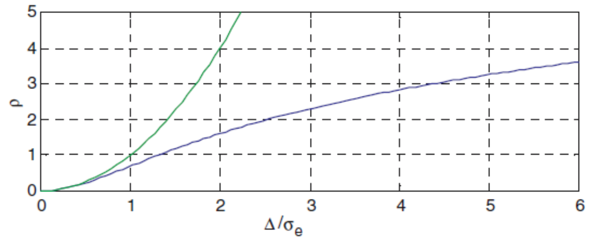


**Figure 6.16 Quadratic (green) estimator $\rho(\Delta) = (\Delta/\sigma_e)^2$, and Lorentzian estimator (blue) $\rho(\Delta) = \ln(1+\Delta/\sigma_e)^2$ (Falchi et al. 2006)**

## 6.8 – Validation of the data

As focused in Falchi et al. (2006), the out-layers are always present in the image velocimetry for different reasons. For example:

- appearance and disappearance of particles that enter or exit the interrogation window or the illuminated plane,
- noise due to the camera, and the image compression,
- variation of particle luminosity due to the non-uniform illumination,
- violation of the motion model due to large velocity gradient within the interrogation window,

- presence of scale of motion smaller than the thickness of the light sheet, so the particles appear to move differently in the interrogation window since they are at different depth.

The validation processes consists of the identification and rejection of the spurious vectors from the data set, there are different algorithms for their identification, and the most important ones are described in the following:

**Dynamic Mean Value Operator:** The magnitude of each velocity vector *u(i,j)* is compared individually with the average of the nearest neighbours $\mu_U(i,j)$. The velocity vector will be rejected if the absolute difference of magnitude between the vector and the average vector of the first N neighbours is above a certain threshold $\varepsilon$.

$$|\mu_U(i,j) - u(i,j)| < \varepsilon \,, \tag{6.26}$$

where

$$\mu_U(i,j) = \frac{1}{N}\sum_{n=1}^{N} u(n) \,,$$

$$\varepsilon = C_1 + C_2 \sigma_U(i,j) \,,$$

$$\sigma^2{}_U(i,j) = \frac{1}{N}\sum_{n=1}^{N} \left(\mu_U(i,j) - u(n)\right)^2 \,.$$

$C_1$ and $C_2$ are constants and $N$ is the number of the closest neighbours.

**Vector Difference Test:** In this method, the magnitude of a particular vector to each of its neighbours is compared.

$$|u_{diff,n}| = |u(n) - u(i,j)| < \varepsilon \,. \tag{6.27}$$

In this method the case where $|u_{diff,n}| > \varepsilon$ is counted and if this number is higher than a threshold ($\varepsilon$), the vector is classified as spurious.

**Median Test:** In this case all the neighbours velocity vectors are sorted linearly according to their magnitude and, the central value in this order is the median value (u(med)), (Westerweel 1993). The vector is valid if:

$$|u(med) - u(i,j)| < \varepsilon \,. \tag{6.28}$$

It is possible to consider the normalized value as well (Westerweel and Scarano 2005):

$$\frac{|u(med) - u(i,j)|}{r_{med} + \varepsilon_0} < \varepsilon \,, \tag{6.29}$$

where $r_{med}$ is the median value of the residual $r_i = |U_i - U_{med}|$, and $e_0$ is a value set around 0.1 - 0.2 pixel, and takes the remaining fluctuation obtained from correlation analysis into account.

### 6.8.1 Validation of the data in the FTV algorithm

In the FTV algorithm, the samples are validated with the following algorithm based on Gaussian filtering of first neighbour (defined by the Delaunay triangulations), and simulated annealing:

a. for each set of sparse velocity samples, the Delaunay triangulation is computed;

b. for each sample, an interpolation of the value of the first neighbour (following the Delaunay triangulation) is computed using a Gaussian weighted average;

c. the difference between the velocity sample and the interpolated value is computed for every sample;

d. if the measured sample giving the larger difference exceeds a given threshold (a multiple of the standard deviation of the first neighbour, obtained with a Delaunay triangulation), this measured sample is substituted with the interpolation of its neighbours (figure 6.17) and the steps 2-4 are repeated until all differences are below the threshold.

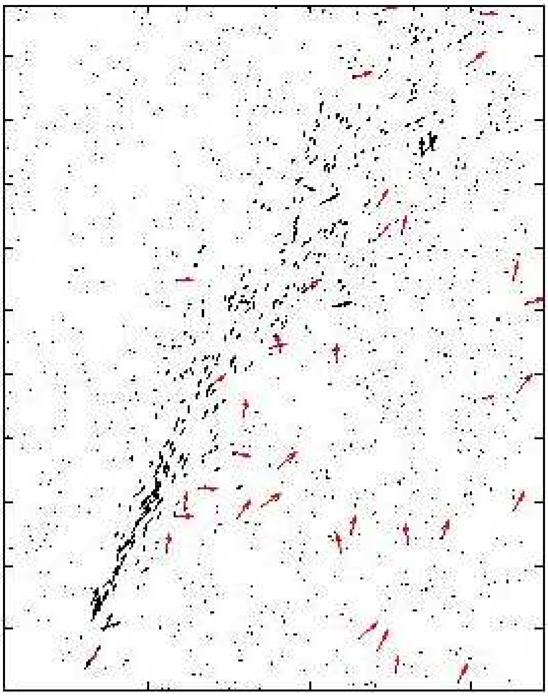

**Figure 6.17 Validation of the data in the model, the black arrows represent the validated vector, the red arrows the spurious vectors.**

## 6.9 – Validation of the Algorithm

The validation of the algorithm is performed using synthetic images comparing the velocity fields obtained with the FTV under different particles/features detection methods.

The validation was performed using the synthetic images of Okamoto et al. (2000), for a 2D wall shear flow.

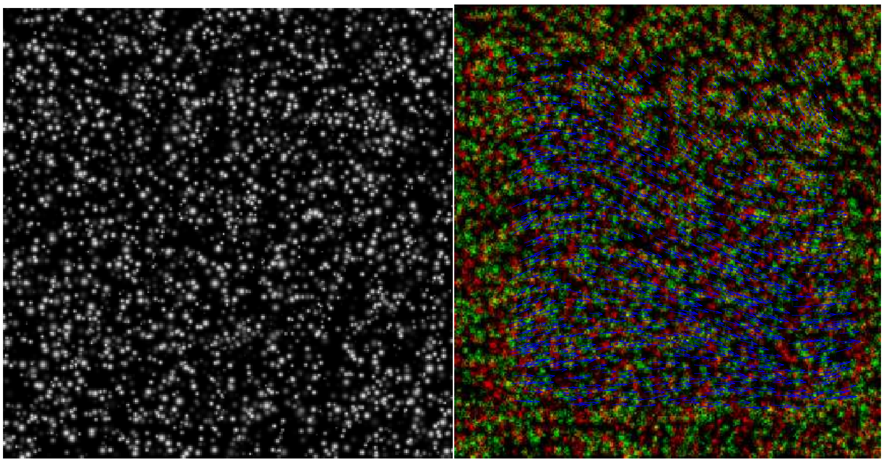

**Figure 6.17 Case 1: (Left) Image of a 2D wall shear flow ; (Right) particle position at time "t" (red), particle position at "t + $\Delta$t" with the corresponding velocity vector (blue), computed using FTV.**

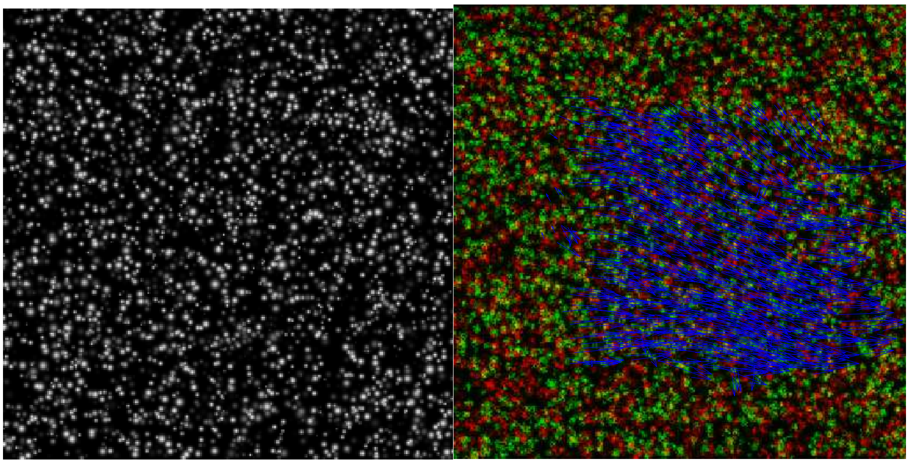

**Figure 6.18 Case 2: (Left)Image of a 2D wall shear flow, in case of large displacement; (Right) particle position at time "t" (red), particle position at "t + $\Delta$t" with the corresponding velocity vector (blue), computed using FTV.**

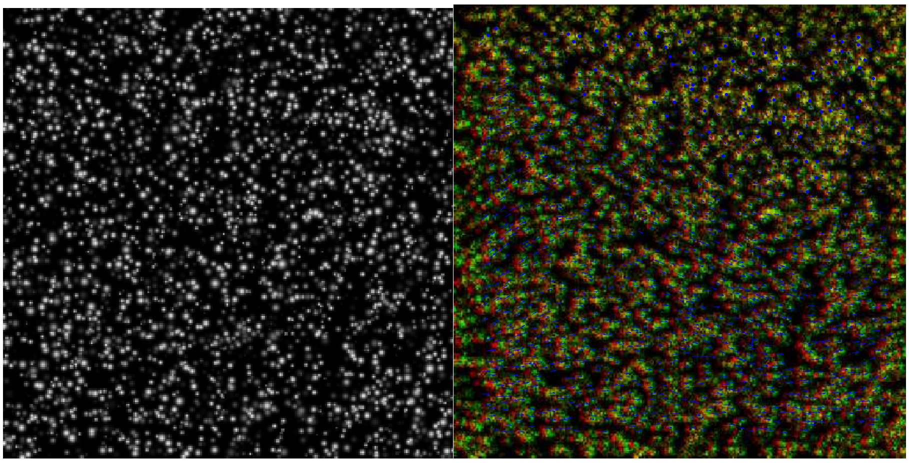

**Figure 6.19 Case 3: (Left)Image of a 2D wall shear flow, in case of small displacement; (Right) particle position at time "t" (red), particle position at "t + Δt" with the corresponding velocity vector (blue), computed using FTV.**

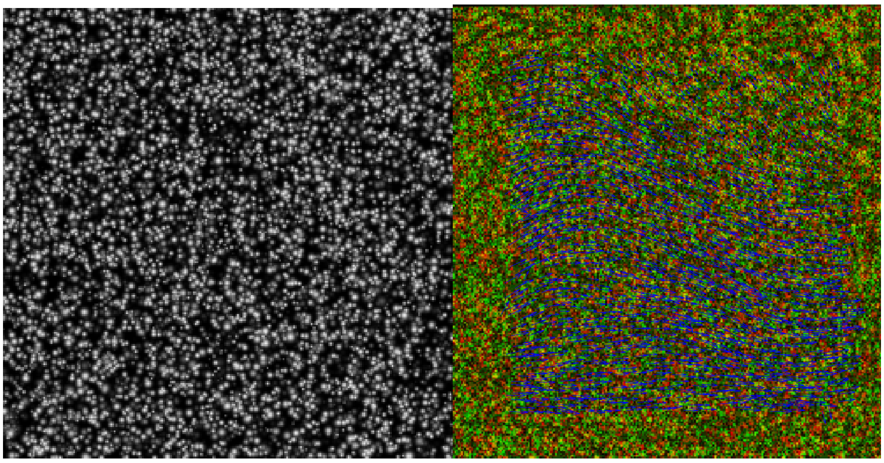

**Figure 6.20 Case 4: (Left)Image of a 2D wall shear flow, in case of high density; (Right) particle position at time "t" (red), particle position at "t + Δt" with the corresponding velocity vector (blue), computed using FTV.**

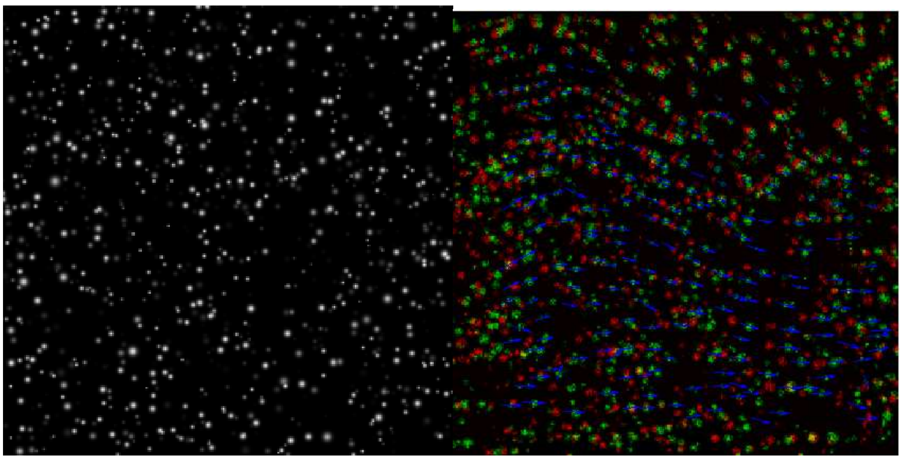

**Figure 6.21 Case 5: (Left)Image of a 2D wall shear flow, in case of low density; (Right) particle position at time "t" (red), particle position at "t + Δt" with the corresponding velocity vector (blue), computed using FTV.**

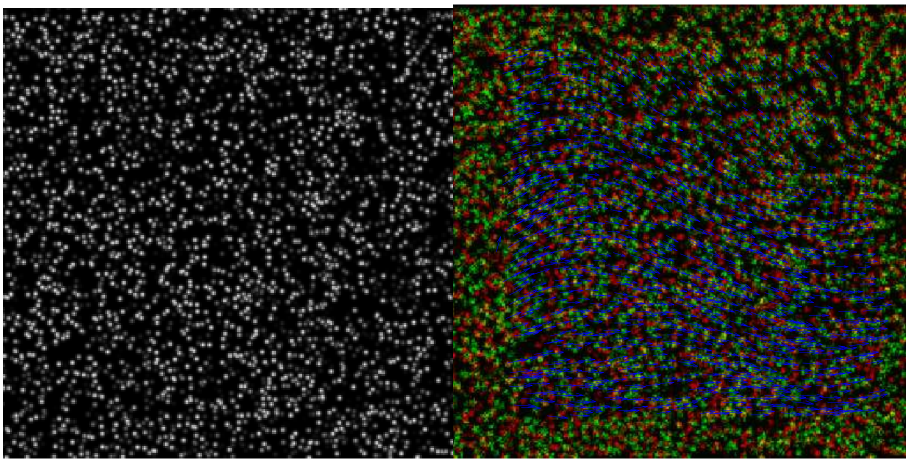

**Figure 6.22 Case 6: (Left)Image of a 2D wall shear flow, in case of constant particle size; (Right) particle position at time "t" (red), particle position at "t + $\Delta$t" with the corresponding velocity vector (blue), computed using FTV.**

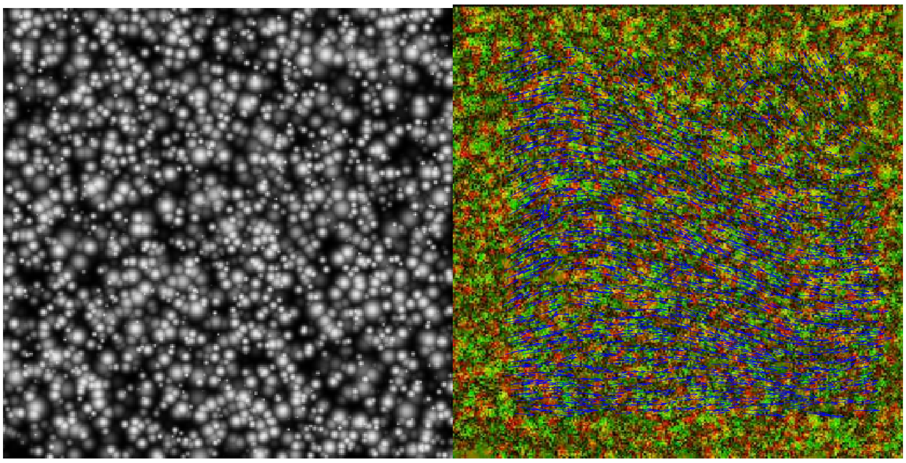

**Figure 6.23 Case 7: (Left)Image of a 2D wall shear flow, in case of high particle size; (Right) particle position at time "t" (red), particle position at "t + $\Delta$t" with the corresponding velocity vector (blue), computed using FTV.**

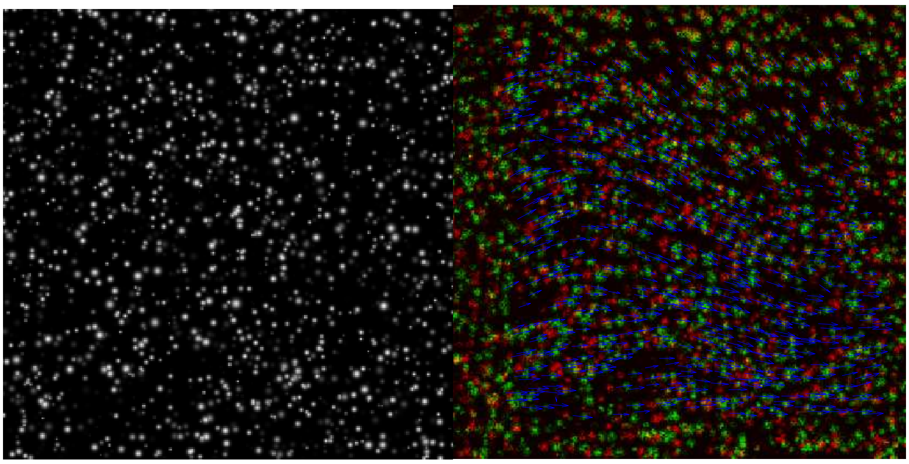

**Figure 6.24 Case 8: (Left)Image of a 2D wall shear flow, in case of large out of plane velocity; (Right) particle position at time "t" (red), particle position at "t + $\Delta$t" with the corresponding velocity vector (blue), computed using FTV.**

Under this first validation, it can be noticed (table 9.1) that the mean velocity and the maximum velocity show appreciable results for all the cases, for sparse or dense particles, where a PTV or PIV techniques are currently used, and in case of different velocity or particle dimension. The standard deviation is considerably different due to the presence of a boundary where it is not possible to estimate the velocity.

**Table 9.1 Test cases**

| No | Density | Synthetic images | | | FTV | | | N particles |
|---|---|---|---|---|---|---|---|---|
| | | Vmean | Vmax | Std | Vmean | Vmax | Std | |
| **1** | Reference | 7.5 | 15.0 | 3.0 | 7.4252 | 14.4726 | 2.6629 | 4000 |
| **2** | Large displacement | 22.0 | 45.0 | 9.0 | 22.2247 | 44.6797 | 8.8760 | 4000 |
| **3** | Small Displacement | 2.5 | 5.1 | 1.0 | 2.5091 | 5.1125 | 0.9738 | 4000 |
| **4** | Dense particle | 7.4 | 15.0 | 3.0 | 7.3955 | 15.1551 | 2.8922 | 10000 |
| **5** | Sparse particle | 7.4 | 15.0 | 3.0 | 7.4053 | 14.3002 | 2.6613 | 1000 |
| **6** | Constant particle size | 7.5 | 15.0 | 3.0 | 7.5262 | 15.0661 | 2.6530 | 4000 |
| **7** | Large particle size | 7.5 | 15.0 | 3.0 | 7.5304 | 14.8454 | 2.7807 | 4000 |
| **8** | Large out-of-plane velocity | 7.5 | 15.0 | 3.0 | 7.5054 | 14.9683 | 2.7184 | 4000 |

## 6.9.1 Analytical Approach

In the second validation a geometrical analytical structure was used (of which the exact velocity is known) after the insemination of the field to determine the motion particles.

The particles have a Gaussian intensity distribution and random position.

The potential function used is

$$f = \sin^2\left(x^2 + y^2\right). \tag{6.30}$$

The corresponding velocities consequently are

$$u = \frac{df}{dy} \qquad v = -\frac{df}{dx} \tag{6.31}$$

After the extrapolation of the synthetic images, the velocity field was determined through the FTV algorithm and the error (the deviation from the velocity field used to generate the images) was computed as

$$error = \frac{\left|U_{real}(i,j) - U(i,j)\right|}{U_{real}}, \tag{6.32}$$

where $U_{real}$ is the intensity velocity obtained by the potential function, and U is the velocity obtained with the FTV algorithm.

During the image generation, a Gaussian noise of controlled amplitude and selected standard deviation was added to the images to analyze the sensibility of the measurement accuracy. The particle's dimension and the particle density were also varied.

In the figure 6.25, the normalized deviation from the real velocities of a field generated by the potential function (6.30), with 500, 1000, 1500, 2000, 2500 and 3000 particles are shown, the x-axis represents the standard deviation of the Gaussian noise. According to this simulation, the FTV model is not very sensitive to the noise level and to the particles density.

In Figure 6.26 the dependence of the prediction error in function of the particle dimension is shown. The image generation was conducted without adding noise. It is evident that error increases with the particles dimension, so the model finds difficulty when two or more particles tend to collapse into the other.

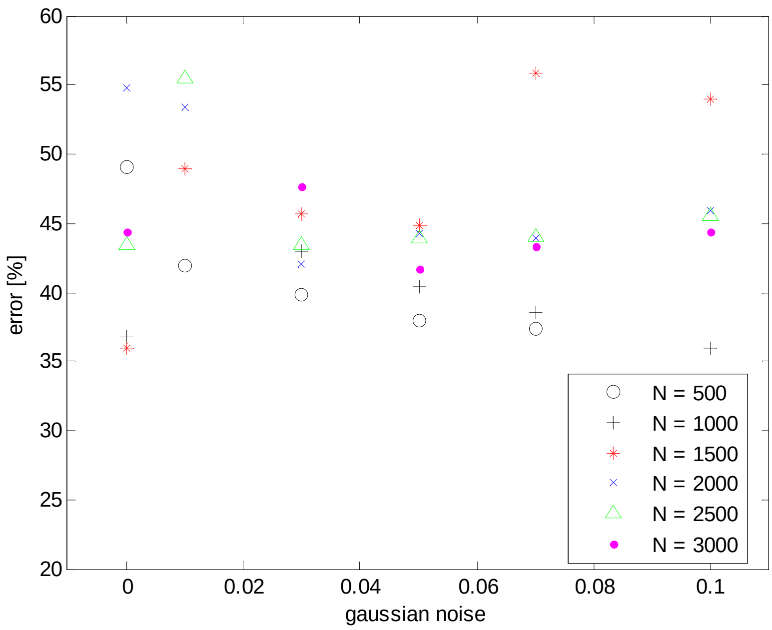


**Figure 6.25 Deviation from the real velocities of a field generated by the potential function (6.30), with different particles density (500, 1000, 1500, 2000, 2500 and 3000 particles), the x-axis is the standard deviation of the Gaussian noise.**

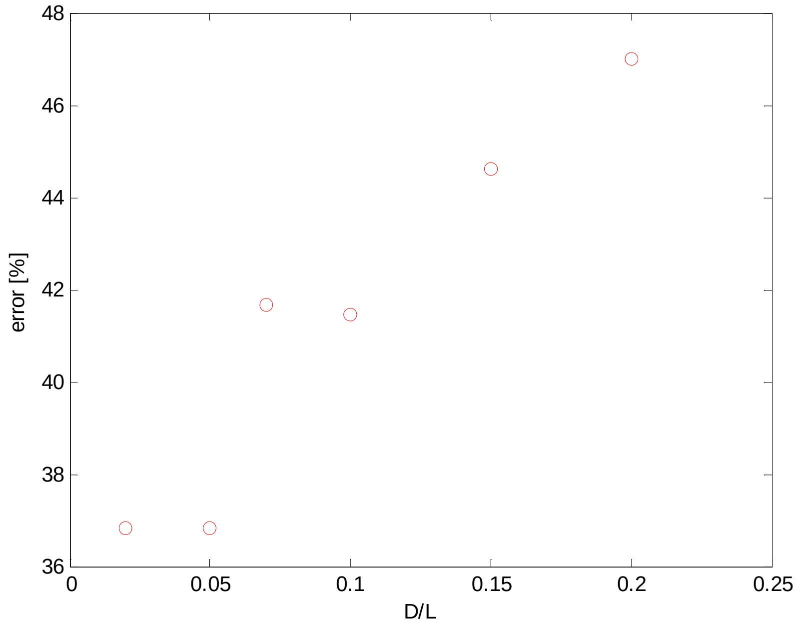


**Figure 6.26 Deviation from the real velocities of a field generated by the potential function (6.30), without any noise, at different particles dimension (D/L).**

# Chapter 7

# Experimental Results

## 7.1 - Experimental determination of Vena Contracta

### 7.1.1. Introduction

When a jet is discharged from a circular orifice, e.g. from a tank or a vessel, the experimental observation indicates that the shape of the resulting jet at the exit is not cylindrical, i.e. it is due to streamlines have to bend toward the exit area before they can converge into the exit orifice(figure 7.1).

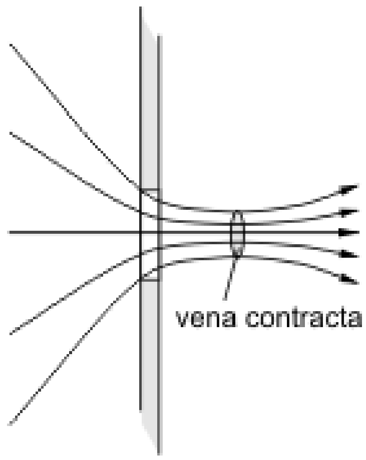


Figure 7.1 Streamlines at the exit of a vessel

Vena contracta is the point of the jet where the cross sectional area is the smallest and consequently, the velocity reaches its maximum. The ratio between the jet cross sectional area at the vena contracta and the area of the orifice is called contraction coefficient.

As shown by Hsiao et al 2010, the dynamic in jets release from sharp-edged orifice is more complex than in jets issued from a smooth contraction nozzle or contoured jets, because the exit flow has an inward radial component, which results from the vena contracta effect, and a considerable unsteadiness, due to the upstream separation. The authors conducted a study about planar jets, with sharp-edged and right-angle orifice plane by using hot-wire technique and smoke flow visualization. They found that the vena contracta effect depends on the Reynolds number and on the geometric configuration of the orifice exit and in particular it is more prominent at lower jet exit velocities and in the sharp-edged orifice plane jet.

In this work, the determination of the contraction coefficient is performed by using Light Induced Visualization for the determination of the concentration levels. A relation between the distance of the vena contracta from the origin, the value of the contraction coefficient and the Reynolds number is also obtained.

### 7.1.2. Light Induced Visualization

The light that the human eye can perceive is bounded by a narrow spectrum of wavelength, ranging between 400 and 700 nm. The Laser Induced Fluorescence (LIF) is a spectroscopic method used to study the concentration fields inside a flow. Usually the applied dye is Fluoresceine, a salt that can be excited at a wavelength of 490 nm (cyan) and emits wavelengths between 520 and530 nm (it peaks at 521 nm), therefore in the region of the green component of the light.

**Figure 7.2 Instantaneous image LIF investigation for a jet with Fr = 15 and $\theta$ = 65° and Re = 1000 (Ferrari et al. 2010)**

If the excitation energy is locally uniform, then the emitted light intensity will be linearly related to the dye concentration. Then, with a simple calibration the emitted light intensity can be directly converted to dye concentration.

**Figure 7.3 Instantaneous image used for the LIV investigation for a jet with Fr = 15 and  = 65° and Re = 1500**

To identify the contraction coefficient in the experiments discussed below, it was not possible to use fluoresceine due to the application of a green laser. It can be excited by Argon-Ion, Blue-Green laser which predominantly emits wavelengths of 488 (blue) and 514 (green) nm. Another chemical substance was used instead: Titanium dioxide that emits in all the visible spectra. For this reason, a more appropriate name for the employed technique is Light Induced Visualization.

### 7.1.3. Results

In this section the results obtained for the determination of the contraction coefficient of the sharp-edged orifice nozzle used in this work are presented. Also the relation between the Reynolds number and the position of the vena contracta from the origin, and the value of the contraction coefficient are determined.

In figure 7.4 a snapshot of a simple jet at Re = 1000 is shown. The presence of vena contracta is evident. It appears before the onset of the Kelvin - Helmholtz structures.

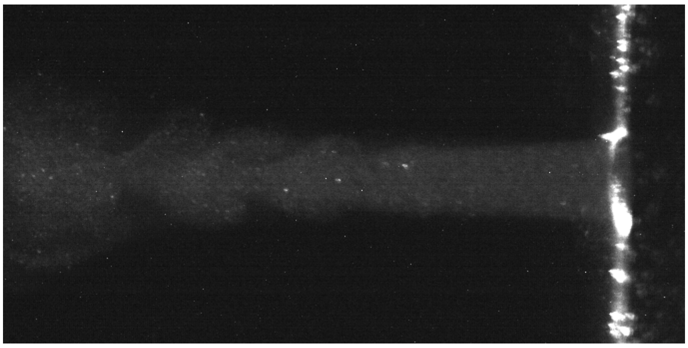

**Figure 7.4 Instantaneous image, of a Simple jet, with Re = 2000**

In figure 7.5 the widening is shown, defined as the position where the concentration reaches the value of $C_C/e$. ($C_C$ is the concentration value on the jet axis.)

Is it possible to note how the behavior of the vena contracta is different for different Reynolds numbers and consequently the deformation of the jet; this behavior is possibly due to the curvature of the diffuser that creates an additional radial component of the flow.

For low Reynolds numbers, the jet starts with a widening similar to the nozzle and then, after approximately 1 diameter, the jet tends to decrease its widening due to the radial velocity component. For Re = 1500, the contraction is larger and starts immediately at the outlet, with an expansion rate higher than the previous case. For Re = 2000, the contraction rate is higher than the two previous cases, but due to the onset of the Kelvin - Helmholtz structures, the expansion rate is higher and the jet reaches a widening equal to the diameter of the jet at approximately 4 diameter.

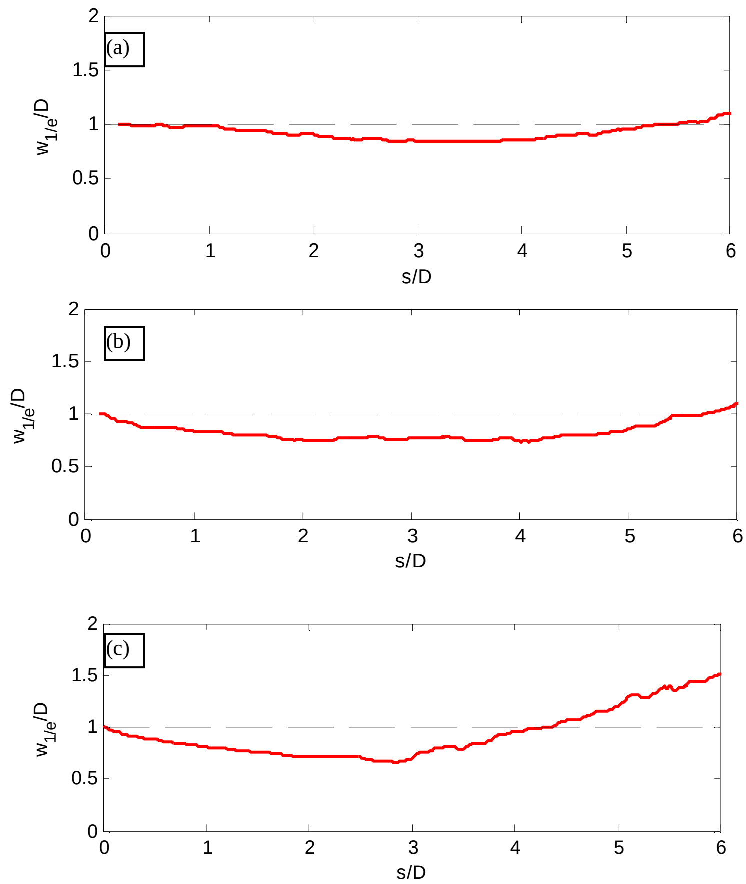


**Figure 7.5 Up: Widening in the near filed, of Simple Jets with Re = 1000 (a), Re = 1500 (b) and Re = 2000 (c),**

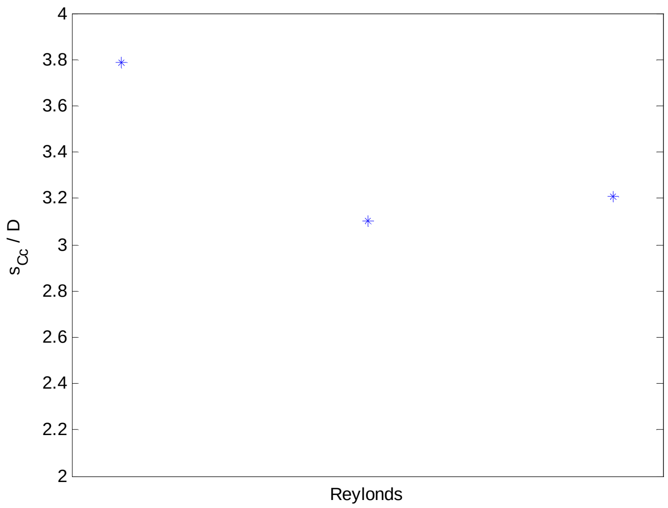


**Figure 7.6 Dependence of the position of the Vena contracta with respect to the Reynolds number; the blue asterisks are the experimental values**

In figure 7.6 the dependence of the position of the vena contracta is shown for low Reynolds number. The definition of the position is not straightforward because the widening is approximately the same for a few diameters. In order to have a unique definition, the values were not calculated by using the instantaneous pictures but by using the mean concentration fields. It was found that the distance is inversely proportional to the Reynolds number.

In figure 7.7 the dependence of the contraction coefficient in function of the Reynolds number is shown and, as above, the values decrease for increasing Reynolds numbers.

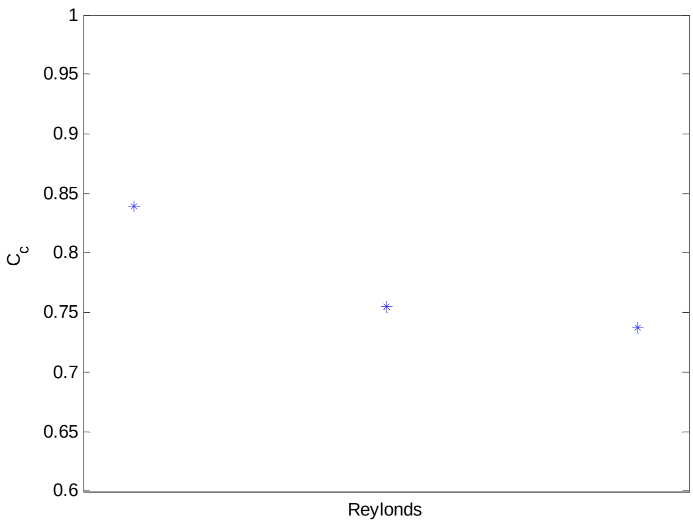


**Figure 7.7 Dependence of the contraction coefficient with respect to the Reynolds number; the blue asterisks are the experimental values**

## 7.2 - Experimental Results for Inclined Negatively Buoyant jets

### 7.2.1 Introduction

When a Negative Buoyant Jet is discharged upwards, the release has an ascending trajectory, in which buoyancy opposes the vertical component of momentum. At some distance, the vertical component of the momentum reduces to zero and the jet reaches its maximum height. From this point the buoyancy forces prevail, the jet descends and impacts the bottom, with an additional dilution due to turbulent phenomena and flow expansion. In the present study two different fields are recorded due to the large range of velocities (from 30 cm/sec near the diffuser to 0.1 cm/s at the end of the jet, or approximately 0 in the surrounding fluid): a full field with an acquisition frequency of 200 Hz (to investigate the entire range of velocity), but admitting the loss of a few particles near the diffuser, and a near field (with an acquisition frequency of 400 Hz) to investigate the behavior near the nozzle.

### 7.2.2 General Observation

The mean velocity fields for Negatively buoyant jets (NBJs) are shown with Re = 1000, θ = 65°, Fr = 8, and Fr = 15, and a Simple Jet (SJ) with the same Reynolds number, normalized by the maximum exit velocity $U_{max.}$, for the full field, in figures from 7.8 to 7.10, and, for the near field, in figure 7.11. In each plot the magenta line represents the jet axis, defined as the locus of maximum velocities. As apparent in the observation of the velocity fields, the NBJs cover a very short initial distance, where they maintain a width similar to the diameter of the orifice, and after a length of few diameters their width grows due to the onset of the Kelvin-Helmholtz instability.

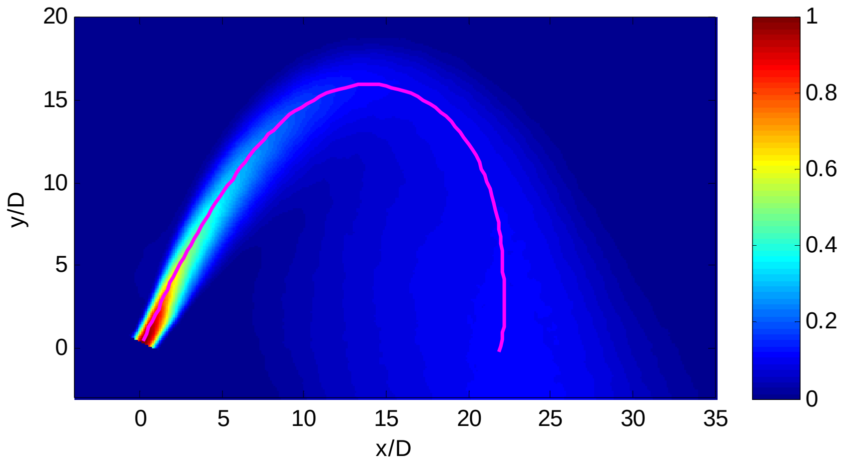


**Figure 7.8 Map of the non-dimensional mean velocity $U/U_{max}$ in the far field ($U_{max}$ is the maximum velocity at the outlet) for an NBJ with θ = 65°, Re = 1000, Fr = 8; the magenta line is the jet axis (defined as the locus of maximum intensity velocity)**

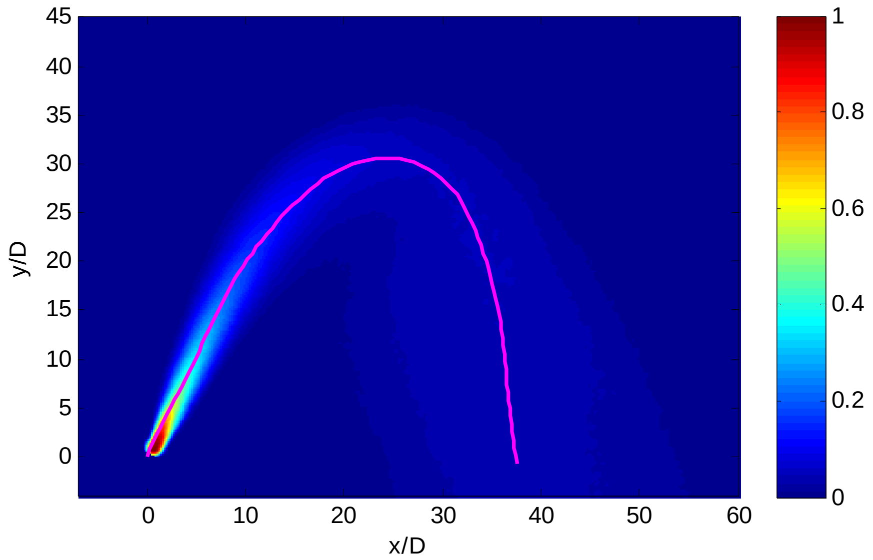


**Figure 7.9 Map of the non-dimensional mean velocity $U/U_{max}$ in the far field ($U_{max}$ is the maximum velocity at the outlet) for an NBJ with $\theta$ = 65°, Re = 1000, Fr = 15; the magenta line is the jet axis (defined as the locus of maximum intensity velocity)**

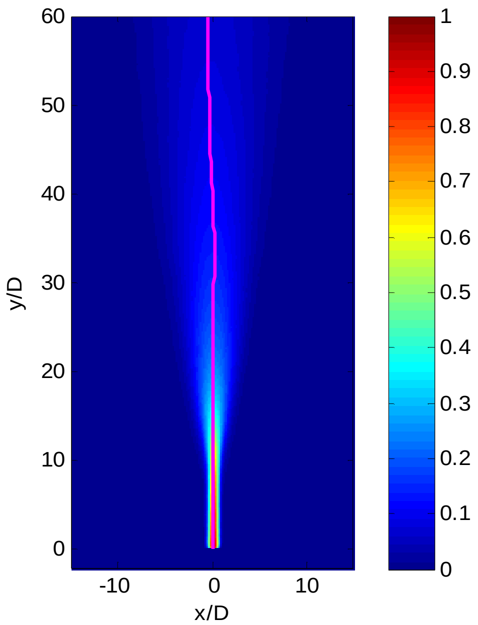


**Figure 7.10 Map of the non-dimensional mean velocity $U/U_{max}$ in the far field ($U_{max}$ is the maximum velocity at the outlet) for a SJ jet with Re = 1000; the magenta line is the jet axis (defined as the locus of maximum intensity velocity)**

The mean velocity fields show a compact jet core near the jet origin, while, at a distance of few diameters from the orifice, the different stratifications in the upper and lower region of the jet (stable the former and unstable the latter) cause an apparent asymmetric development of the NBJs, which widen more in the lower region, where the evolution of the Kelvin-Helmholtz billows is favored by an unstable stratification. From another point of view, it is possible to state that the velocity core and, consequently, the NBJ axis tend to be closer to the upper boundary of the jet than to the lower one, as the detachment of descending plumes tends to erode the velocity core more in the lower region than in the upper one. This lack of symmetry is enhanced for the heavier jet (Fr = 8), whose axis bends at shorter non-dimensional distances, s/D, from the origin with respect to the lighter one (Fr = 15), (s/D is the non dimensional abscissa measured stream-wise along the axis from the origin). Simple jet is Gaussian and axisymmetric, so this behavior is not apparent.

In Figure 7.12 the profiles of the radial velocity are shown (which are orthogonal to the jet axis), normalized by the axial velocity ($U_C$), and computed for different s/D, furthermore compared for the same run of the figure 7.8, 7.10 and 7.11.

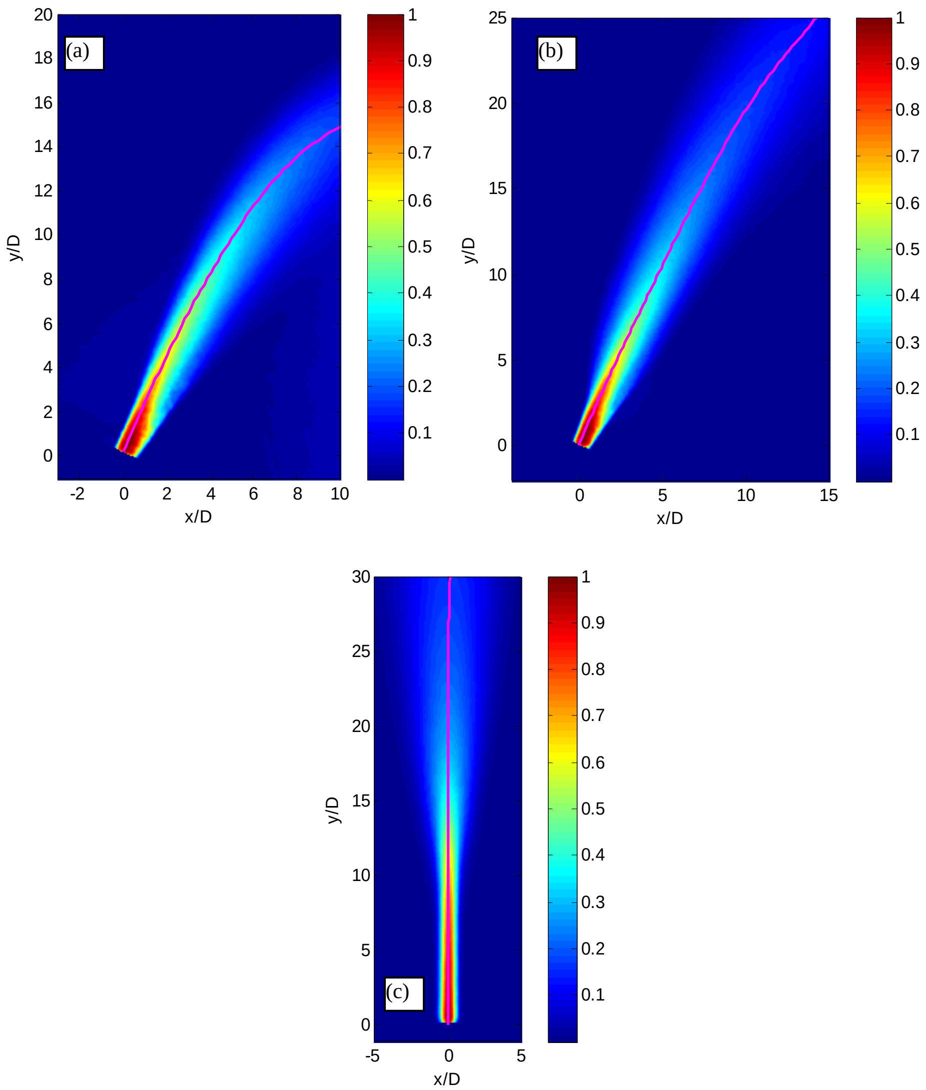


**Figure 7.11 Map of the non-dimensional mean velocity $U/U_{max}$ in the near field ($U_{max}$ is the maximum velocity at the outlet) for NBJs with Re = 1000, and Fr = 8 (a), Fr = 15 (a) and a Simple Jet (c); the magenta line is the jet axis (defined as the locus of maximum intensity velocity)**

The plot shows that the profiles are not symmetric even for small distances from the origin; this behavior is more evident at larger distances from the origin and in the lower boundary, where the detachment of the plume-like structures causes larger widening. In the upper boundary, on the contrary, the local stable stratification permits to the Kelvin-Helmholtz instability to develop completely and the profile maintains a bell shape. The widening increases with the Froude number. On the contrary, the velocity profiles of the SJ preserve their symmetry and the widening is more pronounced only far away from the diffuser, due to the onset of the Kelvin-Helmholtz instabilities.

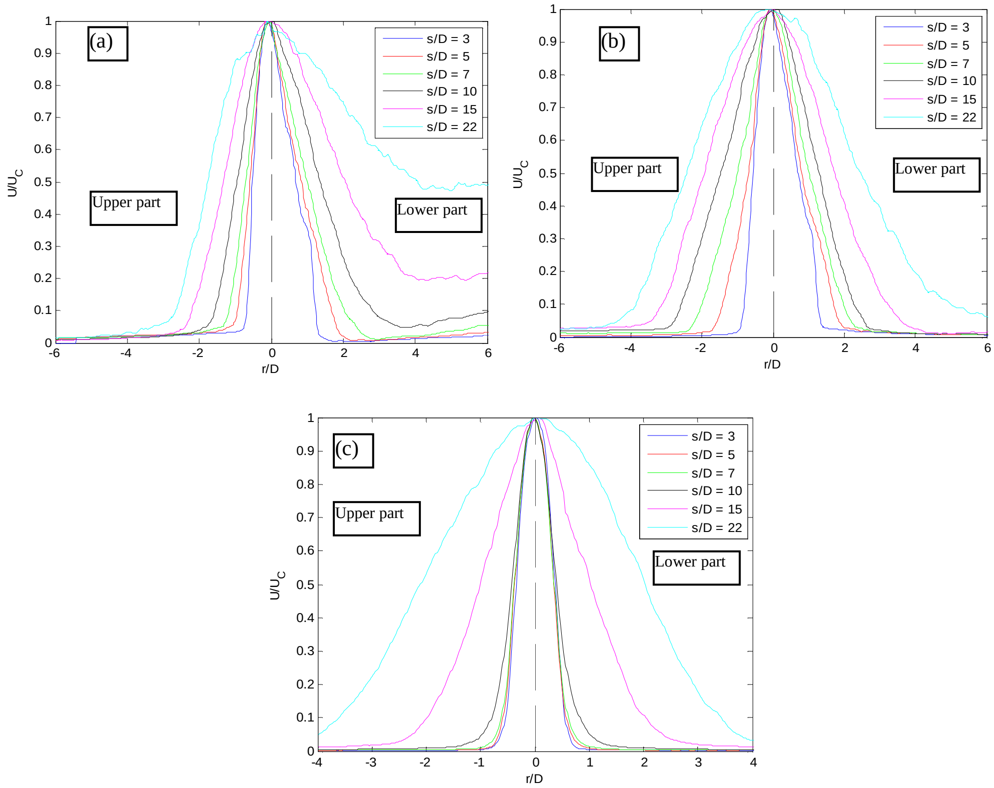


**Figure 7.12 (a) Velocity profiles orthogonal to the jet axis normalized by the maximum axial velocity, for NBJs with Re = 1000, and Fr = 8 (a), Fr = 15 (a) and a Simple Jet with Re = 1000 (c).**

### 7.2.3 Widening and Velocity decay

In order to highlight the role of the densimetric Froude number in the behavior of NBJs, in Figure 7.13, the widening of two NBJs with Re = 1000, θ = 65° and two different Fr (8 in red and 15 in blue) is measured along the axis and plotted versus s/D, together with the SJ data (Fr =∞) by Quinn (2006), issued from a sharp edged orifice (black stars) and from a contoured nozzle (black rhombi). The widening is defined, for each s/D, as the distance $r_{1/2}$ between the two points, in the upper and lower region, where the velocity assumes a value which is half of the axial velocity. This plot highlights the role of the buoyancy, as the Reynolds number is the same for the two NBJs. It is noticeable that both NBJs widen more rapidly than simple jets and that their widening rate, after the initial stage (from s/D ≅ 6), is larger than the simple jets ones. In order to measure this widening rate, which is relevant as it is proportional to the entrainment and so to the dilution, the data for each case (starting from the point where the widening rate becomes substantially constant) have been fitted by least mean square with a straight line. Note that the widening rate of the NBJs (measured by the inclination *m* of the straight line) is larger than that of the simple jets.

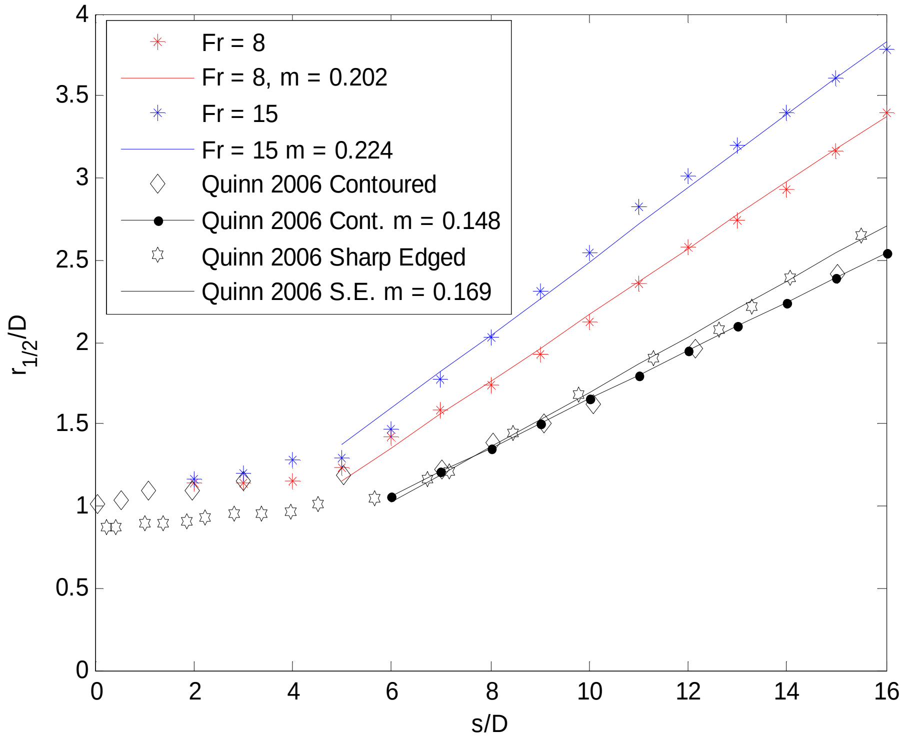


**Figure 7.13 Widening of NBJs with Re = 1000, θ = 65°, Fr = 8 (red) and 15 (blue) and of two simple jets (Quinn 2006]; sharp-edged orifice: black stars; contoured orifice: black rhombi); s/D is the abscissa measured stream-wise along the axis from the origin; the straight lines are the best fits in a least mean square sense; the coefficient m in the legend indicates the slope of the straight lines.**

Figure 7.14 shows the mean centerline velocity decay $U_C/U_0$ versus the non-dimensional axial coordinate s/D for the same two NBJs (colored asterisks) and for the simple jets studied by Quinn (2006), issuing from a sharp-edged (black stars) and a contoured (black rhombi) orifice. The NBJ centerline velocity values have a similar trend compared to the sharp-edged orifice simple jets, starting with values larger than one due to the vena contracta effect. Nonetheless, the NBJ velocity decay is larger, due to their more pronounced widening with respect to the simple jet one. For the same reason, the obtained trend is steeper for Fr = 8 with respect to Fr = 15. Figure 7.14 also displays the decay of the velocity computed on the profiles perpendicular to the jet axis, at a position orthogonal to the axis non-dimensional distance from the axis, r/D, equal to the half widening of a simple jet (simple jet values used for this computations are taken from Quinn 2006) for the lower (triangles) and upper (squares) regions of the NBJs.

The highest velocities are located in the lower boundary, with a sudden decrease at around s/D = 4, which corresponds to the region where the inner core of velocity tends to move toward the upper region. The velocity at the upper boundary is almost constant until about s/D = 6, after it follows a more gradual decay. Moreover, the velocities of the lighter NBJ (Fr = 15) are always higher than the ones of the heavier (Fr = 8): this is due to the fact that these values have been measured at the same orthogonal distance from the axis and, consequently, the values of the lighter NBJ (which widens more, see Figure 7.13) are closer to the high velocity core than the values of the heavier one.

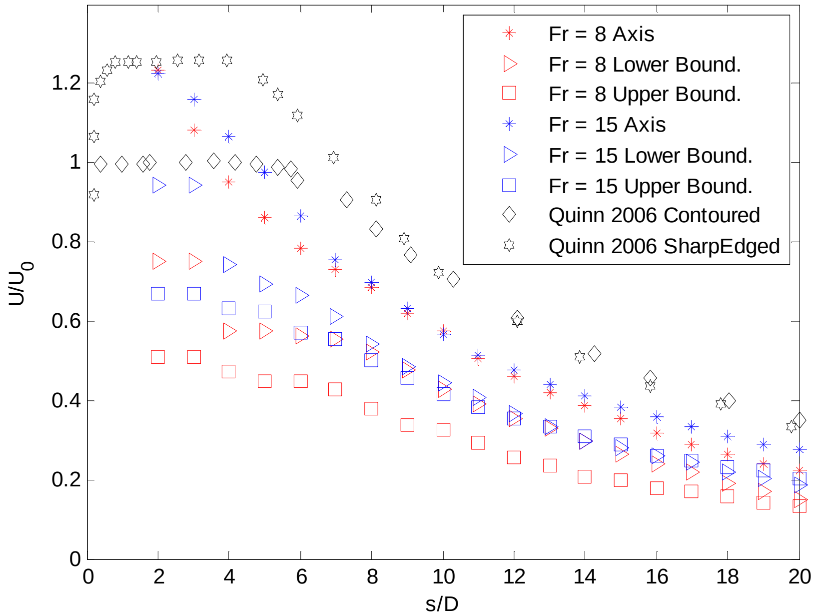


**Figure 7.14 Stream-wise non-dimensional mean velocity decay $U/U_0$ along the axis (asterisks) and in the upper (squares) and lower (triangles) region of the near-field of an NBJ with Re = 1000, θ = 65°and different Fr (red: 8, blue: 15), and of two simple jets (Quinn 2006; sharp-edged orifice: black stars; contoured orifice: black rhombi); the upper and lower boundary decays are measured in correspondence to the widening of a simple jet.**

### 7.2.4 Turbulent Kinetic Energy

As discussed in the Chapter 4, the Turbulent Kinetic Energy (TKE) can be defined as follows:

$$TKE = \frac{1}{2}\left(\overline{u'_x{}^2} + \overline{u'_y{}^2} + \overline{u'_z{}^2}\right) , \qquad (7.2)$$

where $u'_x$, $u'_y$ and $u'_z$ are the velocity fluctuations along the x, y and z axis, and the overbars represent an ensemble average. In this work, only the x and y component can be detected.

In Figure 7.15 the TKE fields are presented (non-dimensionalized by $U_{max}^2$, for the two NBJs and for a Simple Jet considered in previous section); the jet axes are represented with a pink line. The plots display similar and asymmetric behavior close to the jet origin, TKE values are low but, few diameters far from the origin, the onset of the Kelvin Helmholtz instability causes a sudden TKE increase. There are two high value regions at the jet sides; the one located at the lower boundary occurs nearer to the orifice, is shorter and is more intense with respect to the one located in the upper boundary which, in turn, presents lower but more persistent values. As s/D increases, the lower TKE peak region is deflected toward the jet axis and the two peaks tend to merge into a single peak; going further, TKE tends to rapidly decrease as the NBJs become wider. The Simple jet contrariwise is symmetric, and with the high TKE levels persisting longer than NBJs, due to the absence of buoyancy forces.

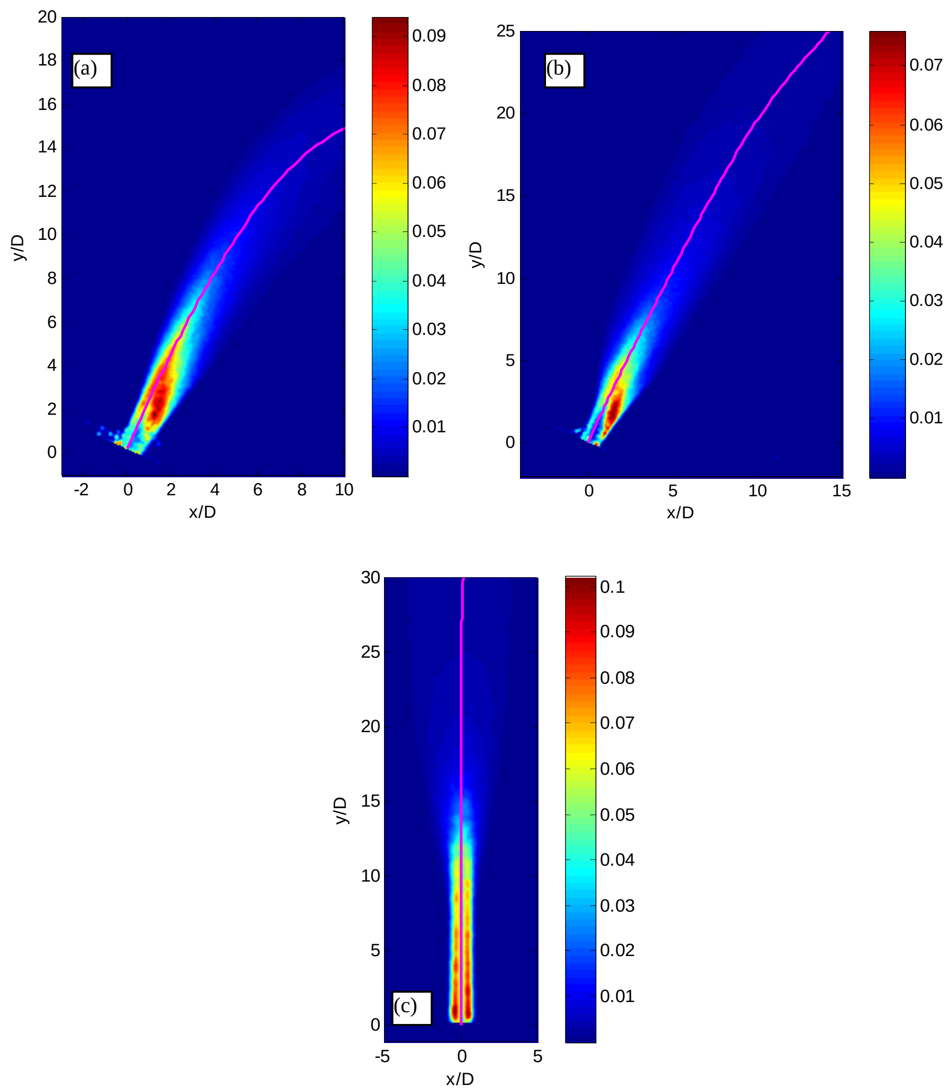


**Figure 7.15 Map of the non-dimensional mean turbulent kinetic energy (TKE), normalized with $U^2_{MAX}$, for a jet having (a) Fr=8, Re=1000 and inclination 65° (b) Fr=15, Re=1000 and inclination 65° (c) Vertical Simple jet with Re = 1000. The pink line represents the jet axis (defined as the locus of maximum intensity velocity)**

Figure 7.16 shows the TKE profiles computed at different distances s/D, the lack of symmetry between the lower and the upper part of the jet is apparent. This axially non-symmetric behaviour implies that the usual integral equations for simple jets and plumes, developed under the hypothesis of axisymmetry, cannot provide precise results.

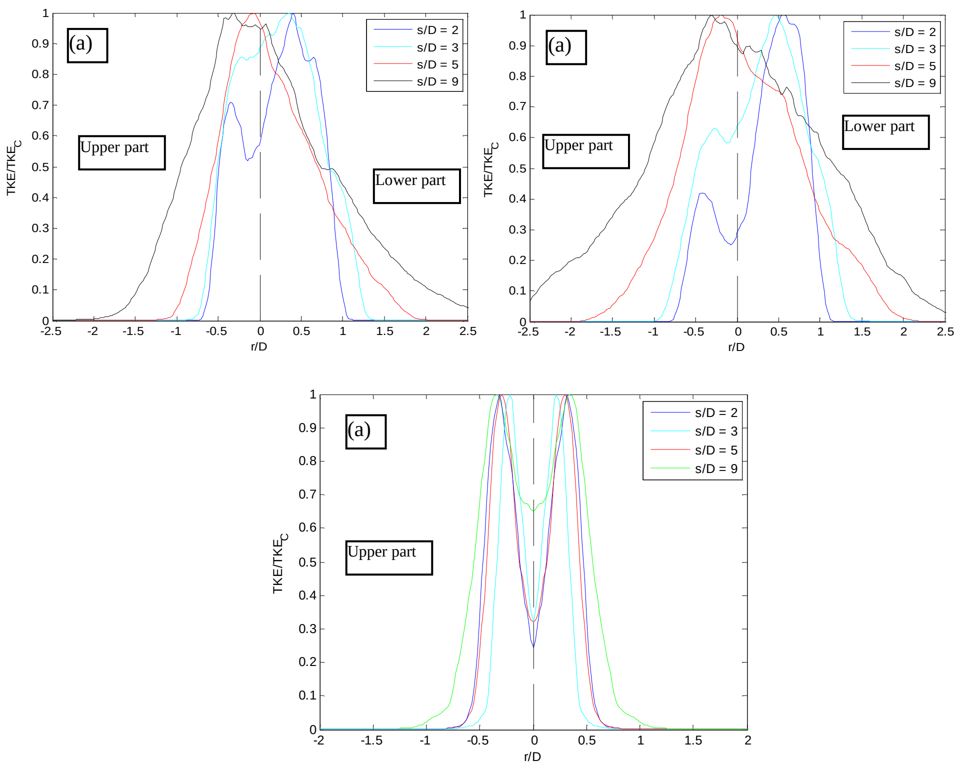


**Figure 7.16 (a) TKE spanwise profiles, for a jet having (a) Fr=8, Re=1000 and inclination 65° (b) Fr=15, Re=1000 and inclination 65° (c) Vertical Simple jet with Re = 1000.**

In order to highlight the differences between the upper and lower region of NBJs in Figure 7.17, the stream-wise decay of $TKE_{MAX}$ (the maxima of $TKE/U_{max}^2$ , where $U_{max}$ is the maximum velocity at the exit of the orifice) was computed on sections orthogonal to the jet axis in the upper (triangles and squares) and lower (asterisks and rhombi) region of the near-field of the two NBJs with Fr = 8 (red symbols) and Fr = 15 (black symbols) and at the boundary of a simple jet (which is, of course, symmetric) with the same Re (green circles) are plotted versus s/D. All the curves have a similar trend, with an initial growth, a peak and a following decrease. The values in the lower region tend to be higher than the ones in the upper region, until around s/D = 6, where the upper region curve collapses into the lower region one. These higher values in the lower region are due to the local unstable stratification, with more intense velocity fluctuations due to the different directions of local momentum and buoyancy. The simple jet values tend to initially stay between the upper region and the lower region values, but showing a smoother trend, with a less pronounced peak, to then collapse, after around 10 diameters from the origin, to the NBJ values.

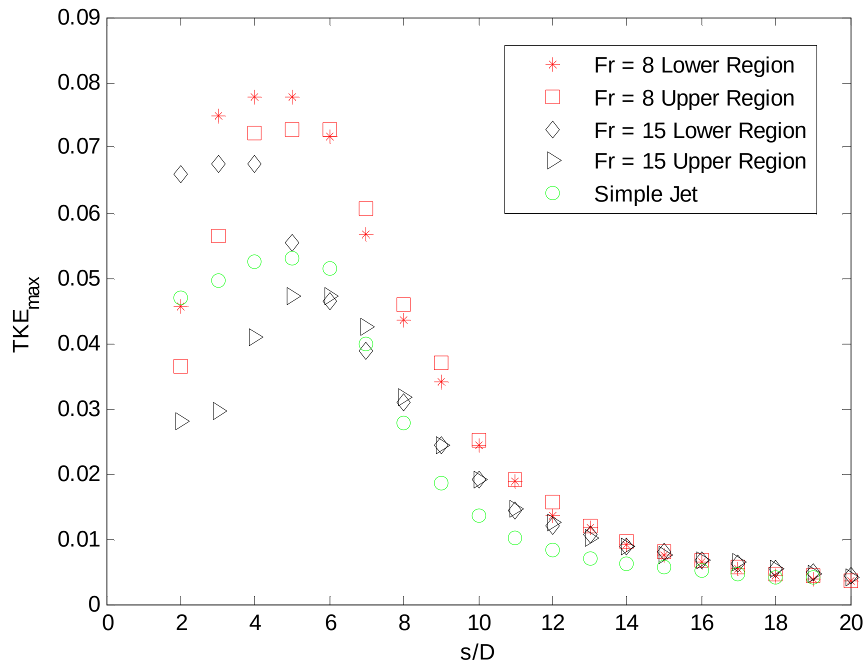


**Figure 7.17 Stream-wise decay of the maximum non-dimensional Turbulent Kinetic Energy $TKE/U_{max}^2$ in the upper (triangles) and lower (asterisks) region of the near-field of an NBJ with Re = 1000, θ = 65°and different Fr (red: 8, blue: 15) and of a simple jet with the same Re (green squares).**

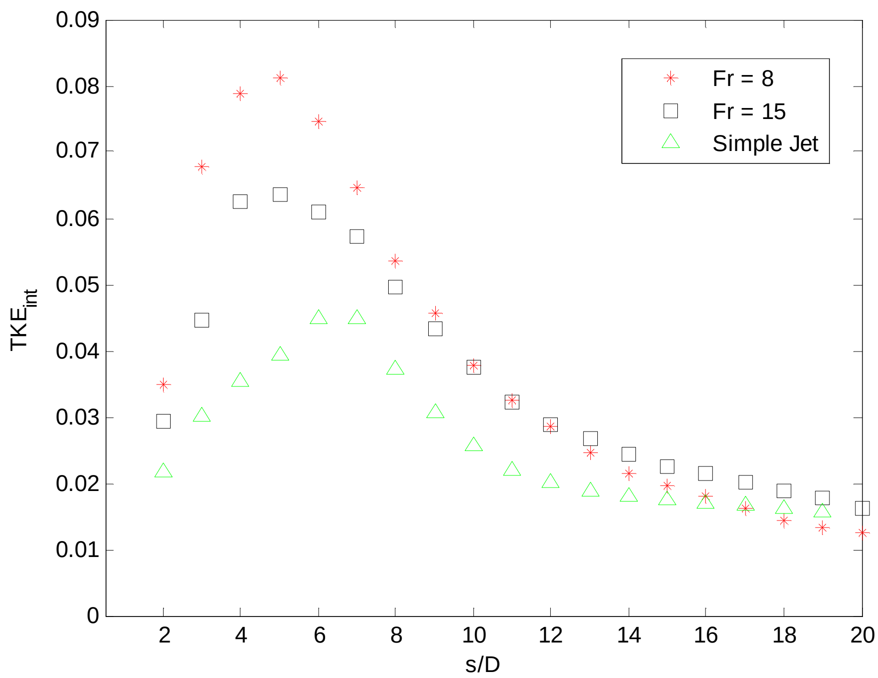


**Figure 7.18 Streamwise decay of the integral non-dimensional Turbulent Kinetic Energy $TKE/U_{max}^2$ in the near-field of an NBJ with Re = 1000, θ = 65°and different Fr (red: 8, blue: 15) and of a simple jets with the same Re (green).**

In Figure 7.18 the stream-wise decay of $TKE_{INT}$ (the integral non-dimensional Turbulent Kinetic Energy $TKE/U_{max}^2$) in the near-field of two NBJs with Fr = 8 (red asterisks) Fr = 15 (black squares) and of a simple jets with the same Re (green asterisks) are plotted along the jet axis; the integral being computed on profiles orthogonal to the jet axis, up to the half velocity jet widening above defined. The influence of Fr on this parameter is more evident: NBJ values start always higher than simple jet ones, with a more pronounced peak (with a higher value for the lower Fr which tends to decrease as Fr increases). The peak for the simple jet is found more stream-wise if compared to the NBJ ones.

In Figure 7.19, $TKE_{INT}$ is separately measured at the upper (red squares Fr=8, black triangles Fr=15) and lower (red asterisks Fr=8, black rhombi Fr=15) region of the two NBJs with Fr = 8 (red) and Fr = 15 (black) and at the boundary of a simple jet with the same Re (green circles) and plotted versus s/D; the integrals are computed on profiles orthogonal to the jet axis, up to the half velocity jet widening, only from the axis upwards or downwards. Considerations similar to those drawn for figure 7.17 can be done, with higher values in the lower region than in the upper one that finally collapse, the simple jet values in the middle between the upper and lower region values and an asymptotic value for the simple jet similar to the NBJ ones.

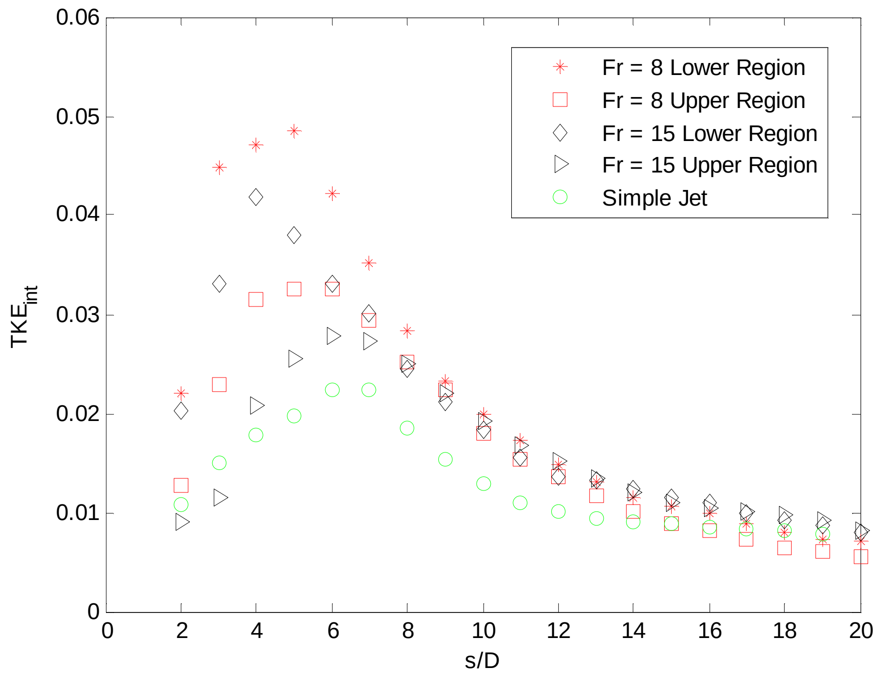


**Figure 7.19 Streamwise decay of the integral non-dimensional Turbulent Kinetic Energy $TKE/U_{max}^2$ in the upper (triangles) and lower (asterisks) region of the near-field of an NBJ with Re = 1000, θ = 65°and different Fr (red: 8, blue: 15 and of a simple jet with the same Re (green squares).**

### 7.2.5 Maximum Reynolds Stresses

The Reynolds stress tensor (RSS) is a real-valued symmetrical tensor in a suitable coordinate system. Referring to the RSS without the minus sign (thus, not following the general convention of considering tensile stresses as positive) the RSS can be expressed as:

$$T = \rho \overline{u_i u_k} = \begin{bmatrix} \sigma_1 & 0 & 0 \\ 0 & \sigma_2 & 0 \\ 0 & 0 & \sigma_3 \end{bmatrix}, \tag{7.3}$$

with $\sigma_1$, $\sigma_2$ and $\sigma_3$ usually ordered as: $\sigma_1 > \sigma_2 > \sigma_3$. They are representing the principal normal stresses, in the coordinate system $(\xi, \eta, \zeta)$, whose axes are termed principal axes, generally not coincident with the generic system (x,y,z). This coordinate system is composed of the Reynolds tensor's eigenvectors directions, and accordingly $\sigma_1$, $\sigma_2$ and $\sigma_3$ are the tensor's eigenvalues.

In 2 dimensions (see Malvern 1969), the Reynolds stress tensor can be expressed as:

$$T = \rho \overline{u' v'} = \rho \begin{bmatrix} \overline{u}^2 & \overline{uv} \\ \overline{uv} & \overline{v^2} \end{bmatrix}, \tag{7.4}$$

where $\rho$ is the density of the flow; u', v' represent the velocity fluctuations in the two orthogonal direction.

Equation (7.4) can then be reformulated as:

$$\sigma^2 - \left(\rho \overline{u}^2 + \rho \overline{v}^2\right)\sigma - \rho^2 \left(\overline{uv}\right)^2 = 0\,. \tag{7.5}$$

Starting from the solutions of the eigenvalues equation:

$$\sigma = \frac{1}{2}\left(\rho \overline{u}^2 + \rho \overline{v}^2\right) \pm \frac{1}{2}\sqrt{\left(\rho \overline{u}^2 + \rho \overline{v}^2\right)^2 - 4\rho^2 \left(\overline{uv}\right)^2}\,. \tag{7.6}$$

The semi difference of Equation (7.6) is the maximal Reynolds stress, whose direction is not aligned with the coordinate system, and can be computed in terms of the measured velocity components. It is expressed as:

$$\tau_{R\max} = \rho \sqrt{\frac{1}{4}\left(\overline{u^2} + \overline{v^2}\right)^2 - \left(\overline{u'v'}\right)^2}\,. \tag{7.7}$$

The determination of the maximum Reynolds shear stress is useful because it is related to the formation of the turbulent structures, and consequently to entrainment.

Figure 7.20 shows the map of the maximum Reynolds stress for experiments performed with a release angle of 65°. They exhibit a similar behavior to TKE fields. Low values are observed in the central jet region, while two high value regions are present at the jet borders, with the maximum in the upper boundary, where the Kelvin – Helmholtz (KH) structures develop and rapidly break, due to the buoyancy contrasting their growth. For high Re, the values are higher but rapidly decay; conversely, with a low Reynolds these values are smaller, but more persistent.

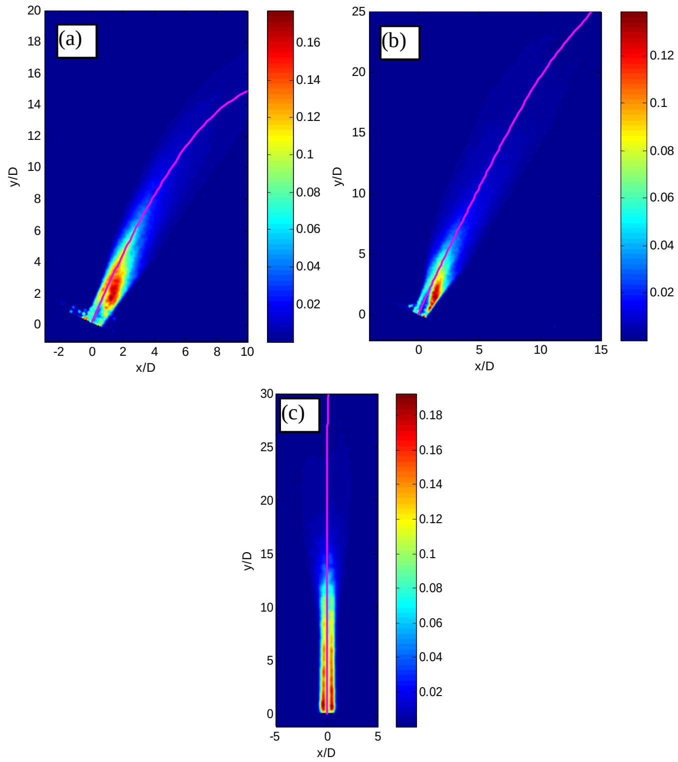

**Figure 7.20 (a) Map of the non-dimensional maximum turbulent Reynolds stresses ($t_{Rmax}$), normalized with $U^2_{MAX}$, for a jet having (a) Fr=8, Re=100 and inclination 65° (b) Fr=15, Re=1000 and inclination 65° (c) Vertical Simple jet with Re = 1000. The pink line represents the jet axis (defined as the locus of maximum intensity velocity)**

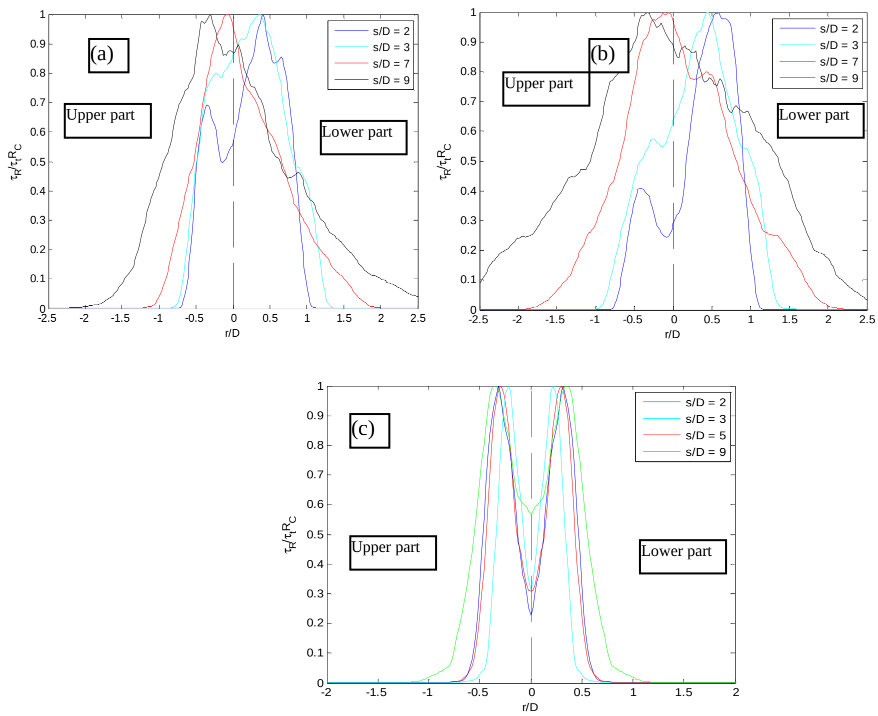


**Figure 7.21 (a) $Tau_{Rmax}$ spanwise profiles, for a jet having (a) Fr=8, Re=1000 and inclination 65° (b) Fr=15, Re=1000 and inclination 65° (c) Vertical Simple jet with Re = 1000.**

This behavior is better explained from the analysis of the non-dimensional spanwise profiles computed at different distances from the outlet and displayed in figure 7.21. Lower values near the orifice are not visible due to the normalization, but the non axisymmetric behavior is evident near the orifice, furthermore the resymmetrization of the Reynolds stresses it is evident, with the movement of the peak toward the axis.

### 7.2.6 RMS velocities

To highlight the ability in reaching high turbulent fluctuations, and consequently mixing in the flow, the spanwise and streamwise turbulence intensities are shown in figure 7.22 for two NBJs with Fr = 8 (red symbols), Fr = 15 (blue symbols) and for a simple jet (SJ), at Re = 1000. Note that the peaks, and therefore the distance where the mixing reaches the centreline, are located at the end of the Zone of Flow Established (ZFE). For the NBJs, it is approximately at s/D = 4 and it is closer to the orifice than for the SJ, with the turbulent intensity inversely proportional to the Froude number.

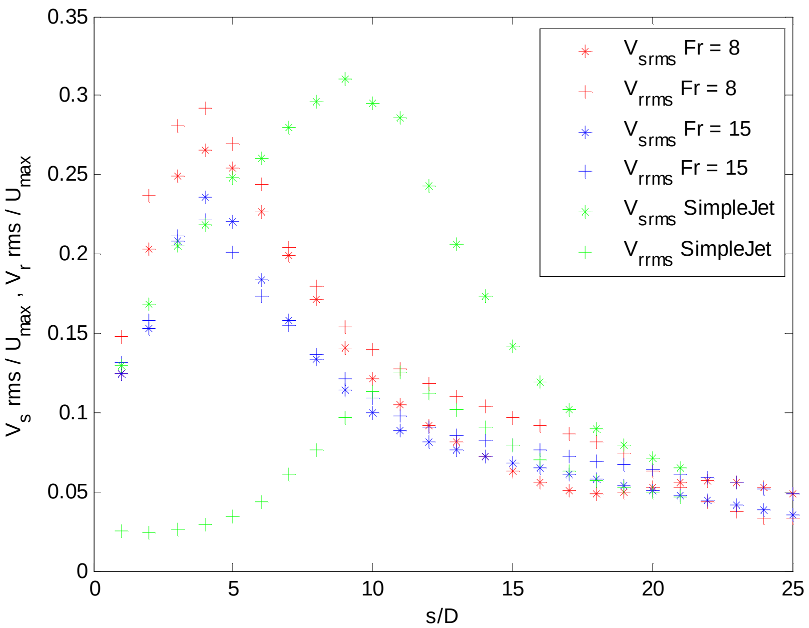


**Figure 7.22 Streamwise (asterisks) and spanwise (crosses) distribution of turbulence intensity for two NBJs with Re = 1000, θ = 65° and Fr = 8 (red symbols), Fr = 15 (blue symbols) and a Simple jet with Re = 1000**

For the SJ the peak is further away, approximately at s/D = 10. Another important result is that NBJs exhibit similar streamwise and spanwise values of turbulence intensities due to the production of TKE in the vertical (spanwise) direction by the buoyancy forces. The isotropic behaviour is reflected in figure 7.23, in which the ratio between streamwise and spanwise turbulence intensities is shown. This is a common method to evaluate the large scale anisotropy of turbulence; in the figure this ratio is equal to 1 for NBJs (like for an ideal isotropic flow), instead for the circular simple jet, the asymptotic value is close to 1.3 (found also by Antonia et al. 2004) and the local value remains larger till s/D = 10, due to the presence of the compact core, that ends at this position, in which the spanwise velocities stay lower than the streamwise.

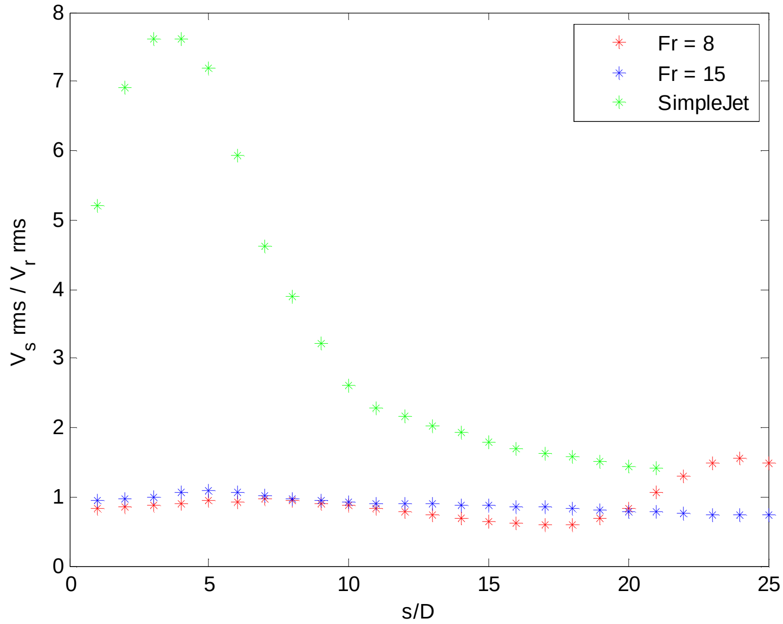


**Figure 7.23 Centerline evolution of streamwise to spanwise turbulence intensity ratio for two NBJs with Re = 1000, θ = 65° and Fr = 8 (red symbols), Fr = 15 (blue symbols) and a Simple jet with Re = 1000**

In figure 7.24 the Reynolds stress spanwise profiles are shown for the same axial interval for the two NBJs (Fr = 8 and Fr = 15) and for a SJ($-V_s'V_r'$), where $V'_S$ is the streamwise fluctuation velocity, and $V'_R$ the spanwise velocity fluctuation), projected along the jet axis. The behaviour of NBJs and SJ is different. The SJ is axis-symmetric, therefore along the axis the stresses (the total, the Reynolds and the viscous stresses) are vanishing. For the NBJs the values are different from zero and the shear stresses have positive values due to the buoyancy forces that act in a different direction compared to that of the momentum. This behaviour is better highlighted in figure 7.25, where the Reynolds shear stress along the axis is shown for the same two NBJs and for the SJ discussed above; for the NBJs, the peak is approximately at s/D = 4 and the values are inversely proportional to the Froude number; on the contrary, for the SJ the centreline value of the Reynolds Shear stress is equal to zero; note also that the behaviour of the three jets is the same at s/D = 15, where the jets are fully turbulent.

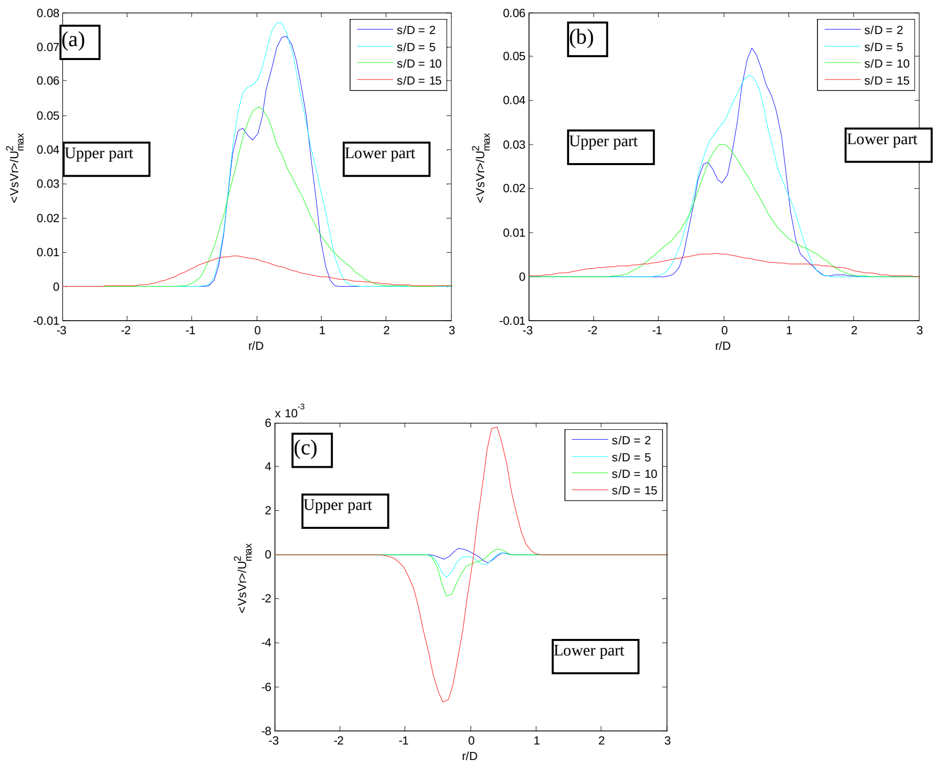


**Figure 7.24 Reynolds stress profiles normalized with $U^2_{max}$ ($U_{max}$ is the maximum exit velocity), different s/D are shown in the legend for two NBJs with Re = 1000 and inclination of 65° an (a) Fr = 8, (b) Fr = 15 and a Simple jet (c) with the same Reynolds number.**

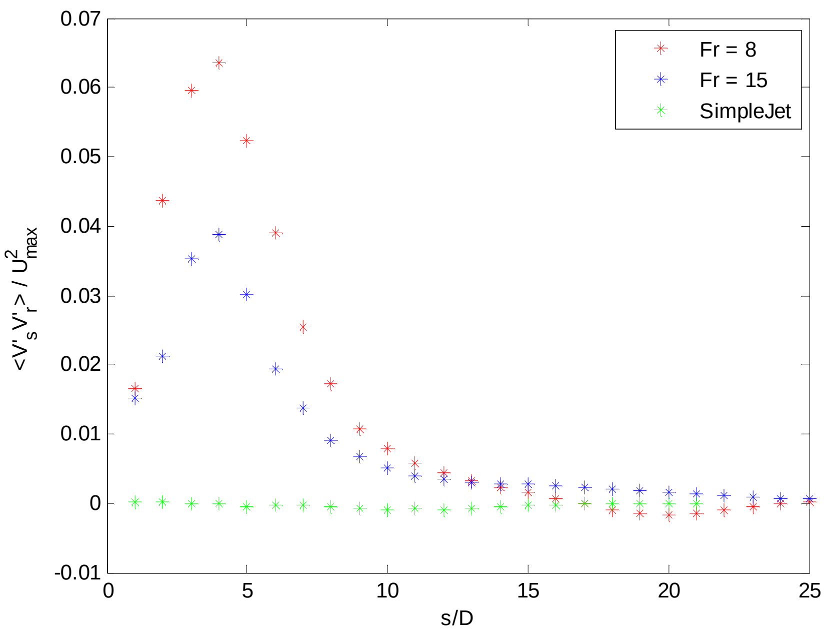


**Figure 7.25 Reynolds shear stress along the axis for two NBJs with Re = 1000, θ = 65° and Fr = 8 (red symbols), Fr = 15 (blue symbols) and a Simple jet with Re = 1000 normalized $U^2_{max}$ ($U_{max}$ is the maximum exit velocity)**

### 7.2.7 Higher order Statistics

To investigate the mixing at small scale level, in figure 7.26 the skewness is shown in the streamwise direction for the two NBJs with Re = 1000, inclination of 65°, Fr = 8 and Fr = 15, and for the SJ with same Reynolds number. The minimum for the SJ is near s/D = 2; instead, for the NBJs, the minimum is at the outlet of the orifice; further away the skewness values tend to the isotropic one (= 0), closer to the orifice for NBJs than for SJ.

Therefore the flow is strongly oriented for the NBJs approximately up to S/D = 5, and for SJ up to s/D = 10. After that the turbulence is isotropic due to the viscous dissipation, with a Gaussian distribution of the fluctuations.

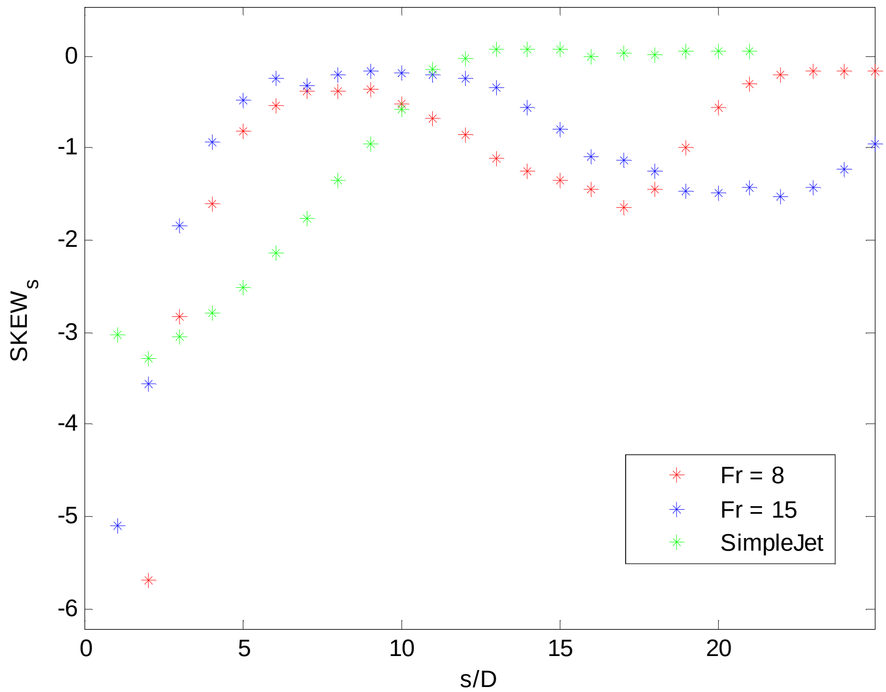


**Figure 7.26 Evolution of skewness at the centerline in the streamwise direction, for two NBJs with Re = 1000, θ = 65° and Fr = 8 (red symbols), Fr = 15 (blue symbols) and a Simple jet with Re = 1000**

## 7.3 - Influence of the Inclination in Negatively Buoyant jets

### 7.3.1 Introduction

In this section three different NBJs are presented with Fr = 15, Re = 1000 at different inclinations: θ = 85°, θ = 65°,  θ = 35°. These three inclinations are the most relevant ones in this type of release, because at inclinations larger than 75 the re-entrainment phenomenon tends to appear due to the proximity of the uprising and descending jet branches. The latter influences the jet trajectory, bending it and causing a reduction of both the maximum height and distance where the entrainment of external fluid reaches the jet axis (Ferrari et al. 2010).

The inclination of 65° to the horizontal axis is close to 63, which Zeitoun et al. (1970) found to be the "optimal" angle that produces the longest trajectory and consequently the highest dilution. 35° is the minimum angle, which is necessary for discharge in shallow water (as shown by Shao et al. (2010)), where a more vertical inclination can interact with the surface, but the Coanda effect (the tendency of the fluid to be attracted by the nearby bottom) is not negligible.

### 7.3.2 Widening and Velocity decay

To show the different behavior obtained by varying the discharge inclination, in Figure 7.27, the widening of three NBJs with Re = 1000, θ = 35°, 65° and 85° is measured along the axis and plotted versus s/D, together with the SJ data by Quinn (2006), issuing from a sharp edged orifice (black stars) and from a contoured nozzle (black rhombi). The widening is defined for each s/D as the non-dimensional orthogonal distance $r_{1/2}/D$ between the two points, in the upper and lower region, where the velocity assumes a value which is half of the axial velocity. The plot highlights the role of the discharge inclination for the three NBJs. It is noticeable that all NBJs widen more than the SJ but a relevant difference between the three NBJs is not evident.

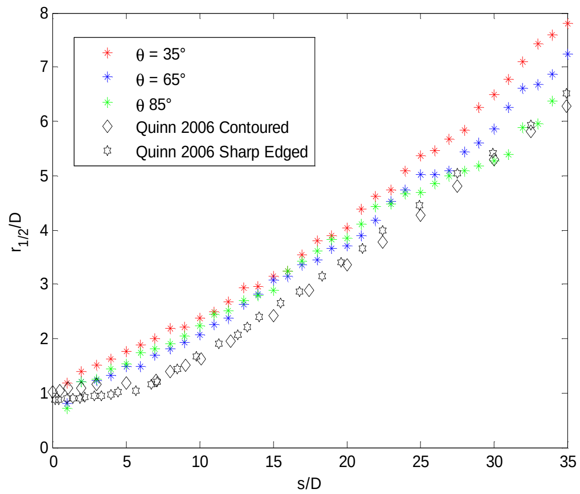


**Figure 7.27 Widening of NBJs with Re = 1000, Fr = 15 and θ = 35° (red), θ = 65° (blue), andθ = 85° (green), and of two simple jets (Quinn 2006]; sharp-edged orifice: black stars; contoured orifice: black rhombi); s/D is the abscissa measured stream-wise along the axis from the origin.**

Figure 7.28 shows the mean centerline velocity decay $U_C/U_0$ versus the non-dimensional axial coordinate s/D for the three NBJs (colored asterisks) and for the simple jets studied by Quinn (2006), issuing from a sharp-edged (black stars) and a contoured (black rhombi) orifice. The centerline NBJ velocity has an initial value larger than one, like the sharp-edged orifice, but the decay is more pronounced, due to the larger widening with respect to the simple jet. In this figure a relevant difference is not present between inclinations, but only between s/D = 6 ÷ 10. The velocity decay is slightly different, probably due to the interaction with the bottom when $\theta$=35°, and the development of re-entrainment (the mixing of the jet with its own fluid) for the $\theta$=85°.

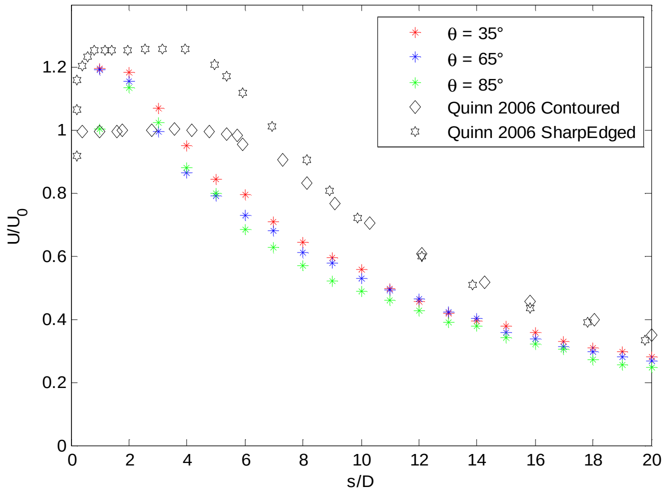


**Figure 7.28 Stream-wise non-dimensional mean velocity decay $U/U_0$ along the axis (asterisks) with Re = 1000, Fr = 15 and $\theta$ = 35° (red), $\theta$ = 65° (blue), $\theta$ = 85° (green), and of two simple jets (Quinn 2006), sharp-edged orifice: black stars; contoured orifice: black rhombi).**

### 7.3.3 Turbulent Kinetic Energy

In the second order statistics, the different behaviour obtained by varying the angle of discharge is apparent in Figure 7.29, where the streamwise decay of $TKE_{INT}$ is plotted as a function of the streamwise distance; the integral is computed on profiles orthogonal to the jet axis, up to the half velocity jet widening defined above. The influence of the inclination on this parameter is apparent: the distance of the peak and the peak value decreases as the inclination increases. Farther from the orifice the behavior is asymptotic.

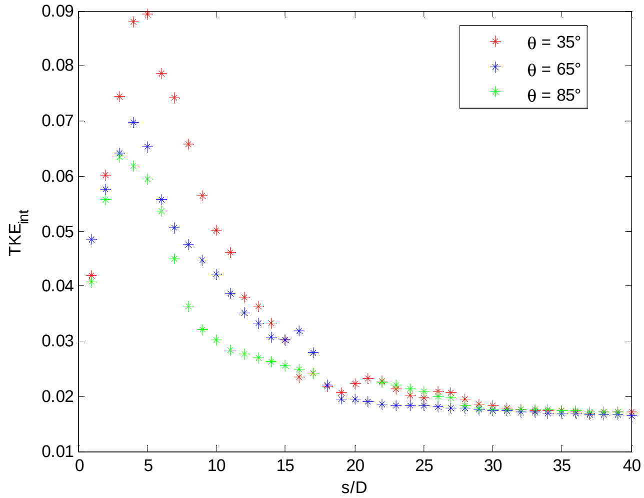


**Figure 7.29 Streamwise decay of the integral non-dimensional Turbulent Kinetic Energy $TKE/U_{max}^2$ in the near-field of an NBJ with Re = 1000, Fr = 15 and $\theta$ = 35° (red), $\theta$ = 65° (blue), $\theta$ = 85° (green).**

# Chapter 8

# CFD Simulations

## 8.1 - Introduction

The use of Computational Fluid Dynamics (CFD) codes and, in particular, of Direct Numerical Simulation (DNS) was encouraged by the constant growth of the power of modern computers. The numerical computation allows the analysis of complex phenomena in 3 dimensions, where experimental measurements are hard to obtain.

The algorithm used in this research was developed by Professor Roberto Verzicco of the University of Tor Vergata in Rome, and it is based on Immersed Boundary model (Iaccarino and Verzicco 2003).

The basic procedure of these models consists of the discretization of the Navier - Stokes equations, to obtain a discrete set of algebraic relations, valid in the grid nodes. The first difficulty is building a smooth surface mesh, adapted to the particular flow simulated (body conforming grid), and to the solid surface. A regular and smoothed mesh increases the reliability of the results, but making a grid of high quality can require more time than the laboratory simulation.

The problems related to the generation of the mesh, in this work, and in general in the Immersed Boundary algorithms were bypassed because this technique allows the use of regular Cartesian-like meshes even in the presence of complex geometries. Furthermore, the effect of the presence of the object into the flow was simply included in the equations introducing appropriate forcing terms in the governing equations, variable in space and, if necessary, also in time.

In this chapter, a preliminary numerical investigation of NBJs conducted prior the experimental studies will be discussed. Being extremely time consuming, the tuning of the parameter was made, but a deeper investigation of NBJs was not possible so far.

## 8.2 - The Model

The algorithm used in this research is an Immersed boundary algorithm. The model allows the resolution of the Navier-Stokes and the tracer conservation equations for the passive scalar, with Direct Numeric Simulation (DNS), Large Eddy Simulation (LES) and Reynolds Averaged Navier Stokes (RANS) models (Iaccarino and Verzicco 2003).

After the preliminary tuning a direct simulation was preferred to solve the Navier-Stokes equation, and a LES model for the tracer conservation equation, using a Smagorinsky method (see chapter 4).

The algorithm has many advantages:

- accurate and reliable discretization schemes and turbulence models;

- a computational geometry model to locate the object into the grid and to transfer information between the mesh and the object surface;

- a mesh enrichment approach to increase the grid resolution in the vicinity of the immersed surface.

The Navier-Stokes equations are solved by a fractional step method with the pressure in the first step. The time advancement of the solution is obtained by a Runge-Kutta 3$^{rd}$ order low storage scheme. The Poisson equation for the pressure is solved directly introducing Fast Fourier Transform in the azimuthal and vertical directions.

All variables are calculated in a staggered grid, cylindrical in the x (span-wise) direction, Cartesian in the y (cross-stream) and in the z directions (stream-wise). The number of nodes in the cylindrical coordinate must be compatible with the Fast Fourier transform ($2^n \cdot 3^m \cdot 5^p + 1$).

## 8.3 - Simulation Condition

A typical set-up was simulated which was also used in the laboratory experiments, i.e. the release was through a cylindrical vessel 20 cm long, 10 cm in diameter and sharp-edged orifice of diameter 0.4 cm, the discharge inclination was 65°.The released liquid is a denser effluent with Fr of 8, 15 and 24. The mesh is scattered, the parameter simulated are summarized in the table 8.1.

The boundary condition of the box was set to the no-slip condition at the upper boundary and to the free-slip condition at the lower boundary. The inflow condition was set at the vertical boundary in corresponding the diffuser (figure

8.1). The flow rate in the boundary was imposed to obtain unitary value at the exit of the diffuser.

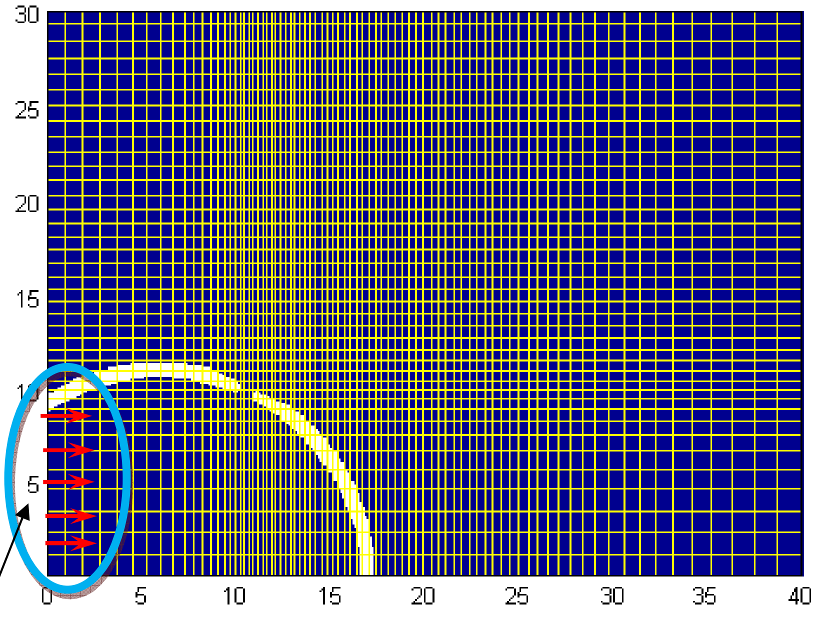


**Figure 8.1 Staggered grid for the simulation of a jet with Fr = 8, q = 65°, Re = 1000 and Pe = 1000. The yellow lines represent a portion of field of 10×10 nodes.**

**Table 8.1**

| Test | Froude | Reynolds | Peclet | Dimension of the field Normalized with D | Resolution | Nodes |
|---|---|---|---|---|---|---|
| 1 | 8 | 1000 | 1000 | 65×55 ×20 | 466×316 ×151 | $22\times10^6$ |
| 2 | 8 | 2000 | 1000 | 65×55 ×20 | 466×316 ×151 | $22\times10^6$ |
| 3 | 8 | 5000 | 1000 | 65×55 ×20 | 466×316 ×151 | $22\times10^6$ |
| 4 | 8 | 10000 | 1000 | 65×55 ×20 | 466×316 ×151 | $22\times10^6$ |
| 5 | 8 | 1000 | 2000 | 65×55 ×20 | 466×316 ×151 | $22\times10^6$ |
| 6 | 15 | 1000 | 1000 | 85×65 ×20 | 512×323 ×151 | $25\times10^6$ |
| 7 | 24 | 1000 | 1000 | 95×70 ×20 | 551×343 ×151 | $29\times10^6$ |

In the model, the format used to describe the solid mesh is the Stereo-LiThografy (STL), where the surface is represented trough a sequence of triangles. In the figure 8.2, a snapshot of the STL-file used is represented.

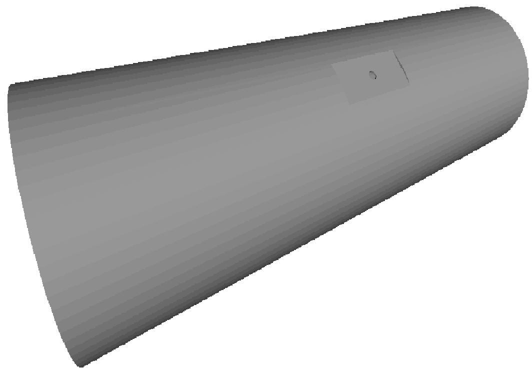

**Figure 8.2 Snapshot of the STL file of the diffuser**

## 8.4 - Results

The output of the model is three dimensional velocity field, concentration field, pressure and vorticity field. In figure 8.3 the middle vertical section of the mean concentration fields is shown for two NBJs with Fr = 8 and Fr = 15.

In the figure 8.4, the mean velocity fields are shown for the same jets.

Note that the behaviour of the jet is quite similar to one obtained by experiments, i.e. the buoyant jet starts with a diameter similar to the nozzle, and then its widening increases due to the Kelvin-Helmholtz structures.

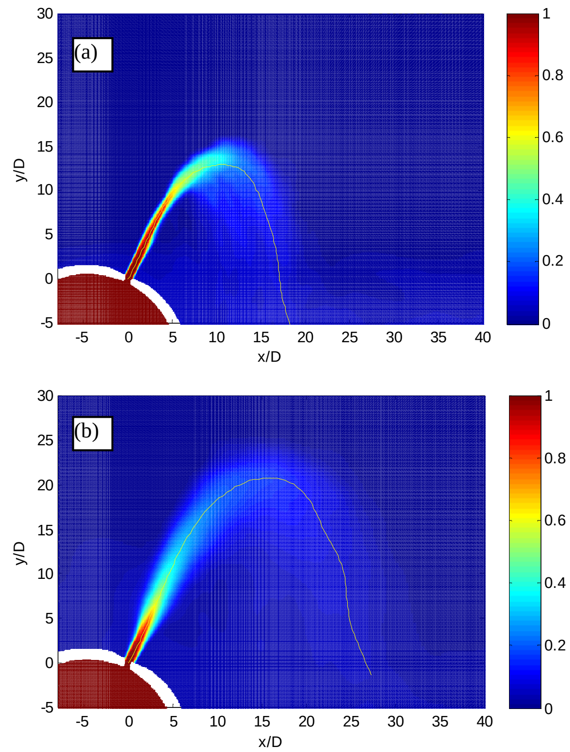


**Figure 8.3 Map of the non-dimensional mean concentration $C/C_0$ ($C_0$ is the outflow concentration) for a NBJ and with (a) Re = 1000, Fr = 8, θ = 65°, Pe = 1000; (b) Re = 1000, Fr = 15, θ = 65°, Pe = 1000; the yellow line is the jet axis (defined as the locus of maximum intensity concentration)**

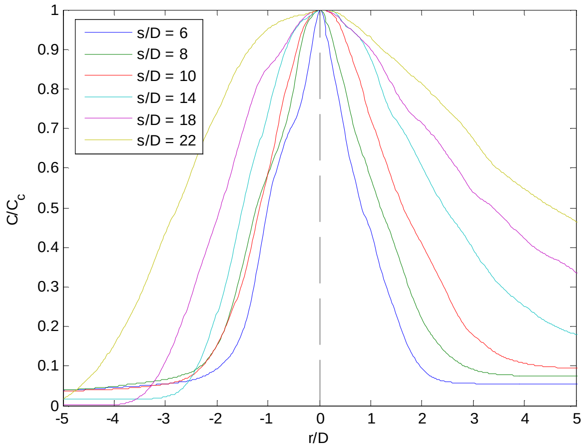


**Figure 8.4 Non-dimensional concentration profile C/C$_C$ (C$_C$ is the maximum axial concentration) for a jet with θ = 65°, Fr = 15, Re = 1000 e Pe = 1000; r/D is the orthogonal distance from the jet axis, and s/D is the distance from the origin along the jet axis.**

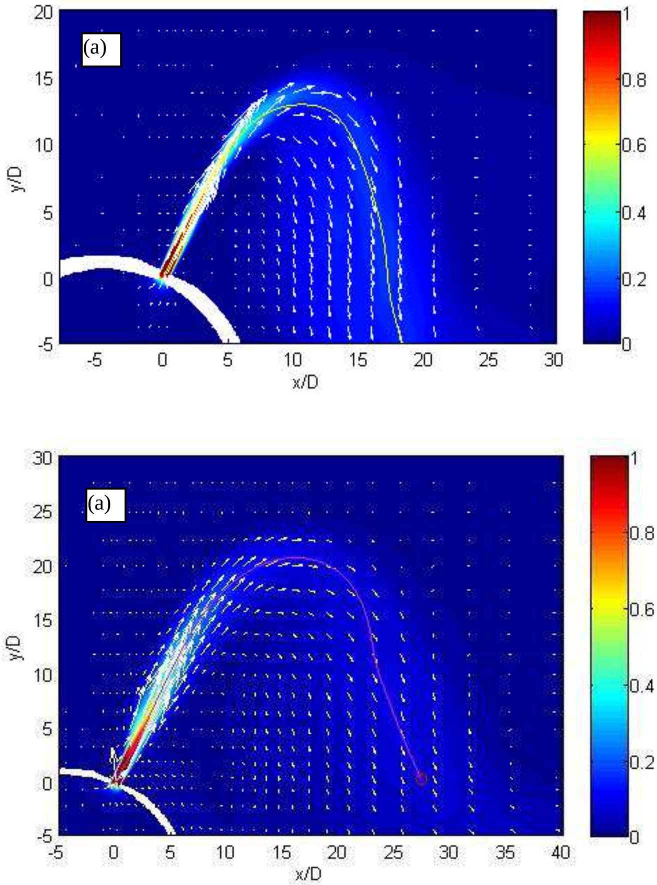


**Figure 8.5 Map of the non-dimensional mean velocity U/U$_0$ (U$_0$ is the maximum velocity at the outlet) for a NBJ with (a) Re = 1000, Fr = 8, θ = 65°, Pe = 1000; and (b) Re = 1000, Fr = 15, θ = 65°, Pe = 1000; the coloured line is the jet axis (defined as the locus of maximum intensity concentration)**

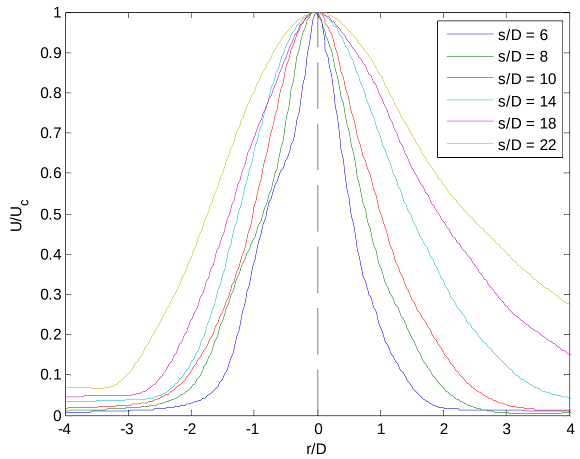


**Figure 8.6 Non-dimensional velocity profile $U/U_0$ ($U_0$ is the maximum axial velocity) for NBJ with $\theta$ = 65°, Fr = 15, Re = 1000 e Pe = 1000; r/D is the orthogonal distance from the jet axis, and s/D is the distance from the origin along the jet axis.**

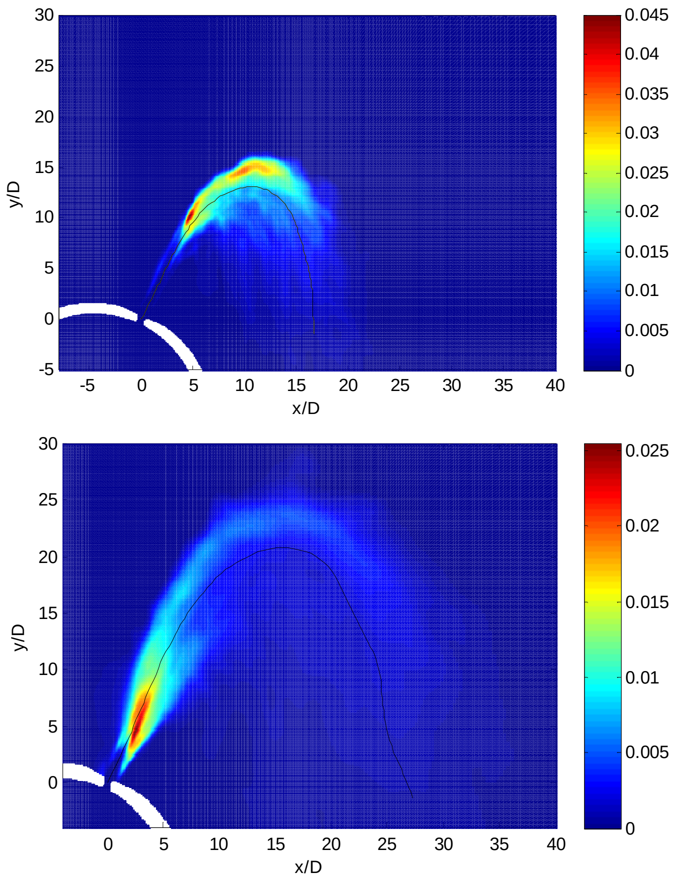


**Figure 8.7 Map of the non-dimensional standard deviation for the concentration field, $C'/C_0^2$ ($C_0$ is the maximum concentration at the outlet) for NBJ with (a) Re = 1000, Fr = 8, $\theta$ = 65°, Pe = 1000; and (b) Re = 1000, Fr = 15, $\theta$ = 65°, Pe = 1000; the black line is the jet axis (defined as the locus of maximum intensity concentration)**

The asymmetric behaviour between the upper and the lower boundary, already shown in the experimental results, can be seen in the concentration (figure 8.4) and velocity (figure 8.6) profiles, and tends to increase with the distance from the orifice.

Although the numerical NBJ with Fr = 15 is trustworthy, a laminar behaviour persists with Fr = 8. Figure 8.7 shows the standard deviation for the concentration fields. In the jet at Fr = 15, the vortical structures start close to the outlet and in the jet at Fr = 8, they start farther when the jet tends to bend. This is observed only in laminar jets, where the turbulence can be generated only by the buoyancy forces.

Figure 8.8 shows the vorticity field for the same jets as before. Note the presence of the vortical rings close to the nozzle in both jets. This fact indicates that the laminar condition in the lower Froude number is not due to the lack of vorticity, but to the absence of turbulence (possibly to the insufficient forcing perturbations).

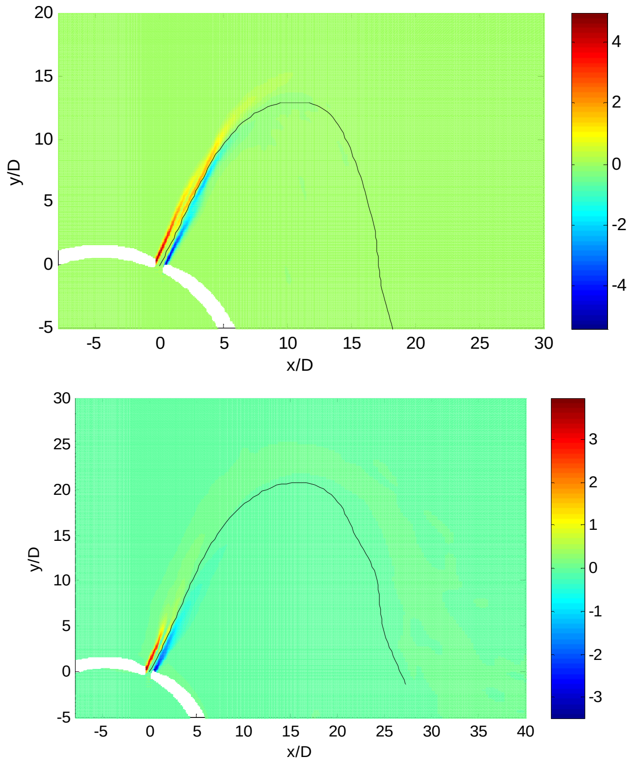


**Figure 8.8 Map of the non-dimensional mean vorticity for a NBJ with (a) Re = 1000, Fr = 8, θ = 65°, Pe = 1000; and (b) Re = 1000, Fr = 15, θ = 65°, Pe = 1000; the black line is the jet axis (defined as the locus of maximum intensity concentration)**

In Figure 8.9, the non-dimensionalized TKE fields are presented for the two simulated NBJs (non-dimensionalized by the square of the maximum velocity ($U_{max}^2$)).The plots display asymmetric behaviour close to the jet origin, similarly to the experimental results: TKE values are low but, the onset of the Kelvin Helmholtz instability causes a sudden TKE increase at few diameters downstream from the origin.

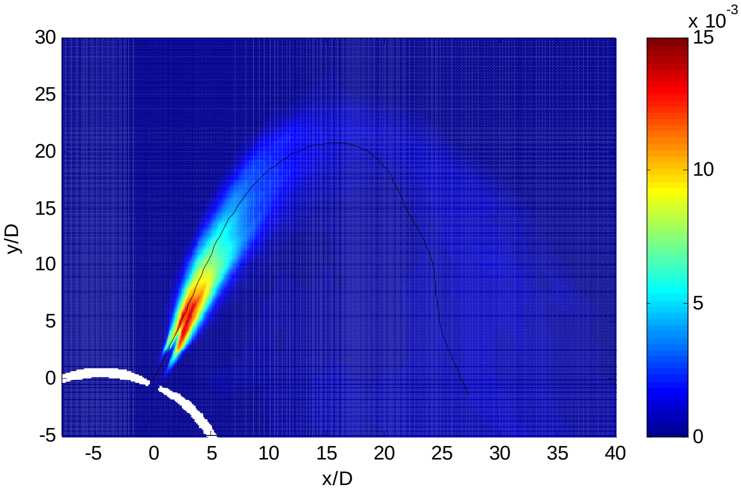


**Figure 8.9 Map of the non-dimensional TKE for NBJ with (a) Re = 1000, Fr = 8, θ = 65°, Pe = 1000; and (b) Re = 1000, Fr = 15, θ = 65°, Pe = 1000; the black line is the jet axis (defined as the locus of maximum intensity of velocity)**

The TKE profiles show the presence of two peaks at the jet sides. The one located at the lower boundary occurs closer to the orifice and tends to disappears earlier. As s/D increases, the lower TKE peak region is deflected towards the jet axis and the peaks tend to merge into a single one. Going further downstream, the TKE tends to rapidly decrease as the NBJs become wider.

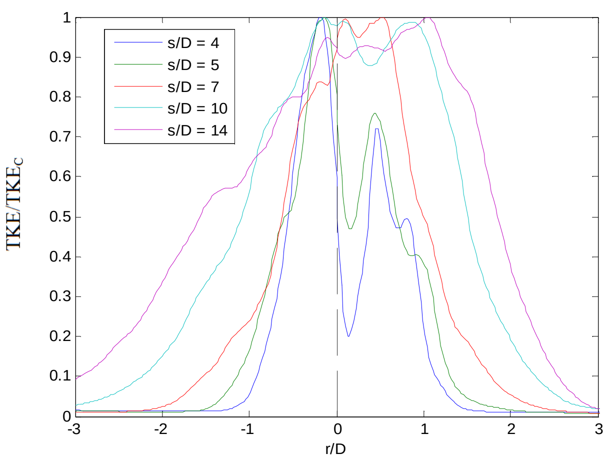


**Figure 8.10 TKE profiles orthogonal to the jet axis of a jet having Fr = 15, Re = 1000, Pe = 1000 and inclination 65°.**

Figure 8.11shows the velocity decay of the results obtained by the numerical simulation, and in the corresponding experimental tests. The results are compared with the empirical law given by Fisher et al 1979:

$$U_C \approx 7M_0^{1/2} \cdot s^{-1}. \qquad (8.5)$$

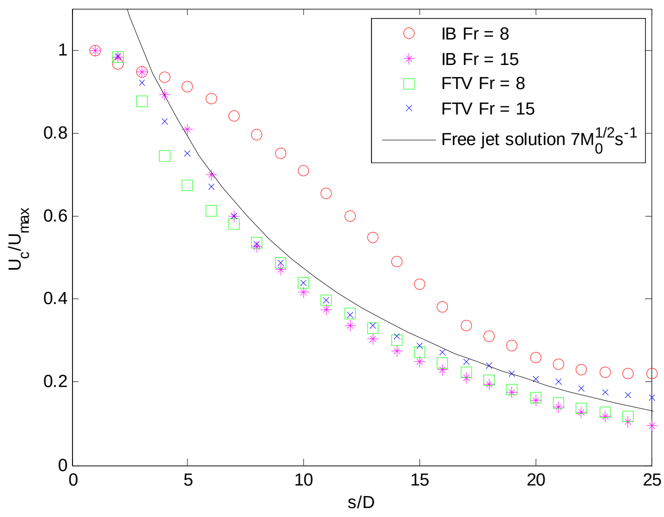


**Figure 8.11 Jet centreline velocity decay for an angle of 65°, for numerical jets with Fr = 8 (red circles) and Fr = 15 (magenta asterisks) and for experimental jets with Fr = 8 (green squares) and Fr = 15 (blue crosses). The continuous line is the equation of the velocity decay for simple jet (Fischer et al. 1979)**

It is noticeable that the behaviour of the numerical jet with Fr = 15 is quite similar to that of the experimental jets and of the Fisher law. The numerical jet with Fr = 8 instead remains in a laminar condition up to 7 D with a lower velocity decay, then a sudden decay is apparent higher than the other jets. In the last part, the behaviour is asymptotic, and the jets follow similar trend.

In figure 8.12 the widening of the jets is defined for each s/D (the non-dimensional orthogonal distance $r_{1/2}/D$ between the two points) in the upper and lower regions, where the velocity assumes a value which is half of the axial velocity.

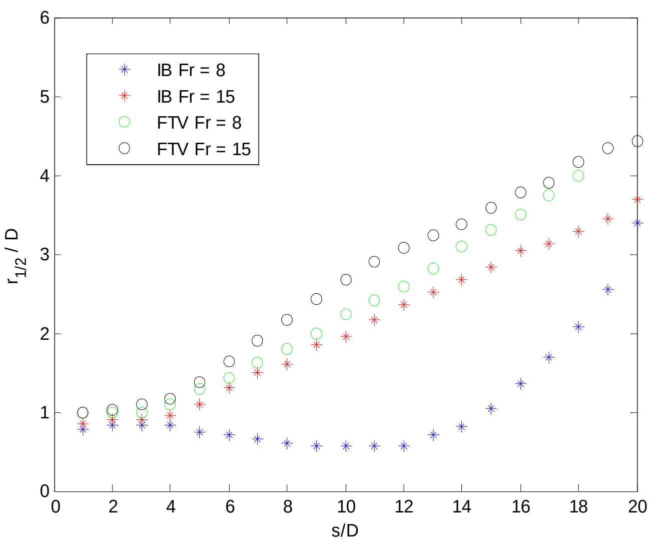


**Figure 8.12 Widening of NBJs with Re = 1000, inclination of 65°, for numerical simulation with Fr = 8 (blue asterisks), and Fr = 15 (red asterisks) and for experimental tests with Fr = 8 (green circles) and Fr = 15 (black circles).**

Note that near the diffuser the widening of the numerical prediction and the one of the experimental results is quite similar. Further downstream the difference tends to get higher. Similar conclusions can be drawn for the case of Fr = 8.The behaviour is typical for laminar jets, i.e. a compact velocity core is present as long as buoyancy forces do not destroy stability.NBJ with Fr = 15 has a quite similar trend in the both cases, but the widening is a little underestimated.

## 8.6 - Conclusion

The model can simulate the behaviour of the jet near the diffuser (approximately up to 20 D) with a good approximation. However, as it is explained in section 2.3.2 as well, numerical models tend to underestimate the maximum height and the dilution levels of the jet (like many other CFD simulations conducted in the past).

Note that the flow tends to be excessively stable even though the applied Peclet and the Reynolds numbers are the same for the two NBJs (Fr = 8 and Fr = 15). The NBJ at Fr = 8 is found to be laminar.

# Chapter 9

# Conclusions

## 9.1 - Conclusions

Negatively buoyant jet flows (NBJs) are generated, when a fluid is ejected upwards into a less dense surrounding fluid with a source of buoyancy and momentum. This kind of flows are frequently used in practical applications and in the last years they have been increasingly popular, for example, to disperse brine or generic pollutant into the sea from desalination, or treatment plants.

Typically, this kind of effluent is characterized by an elevated concentration of the same elemental components of the environmental fluid; therefore an intense dilution in the near field is required, so that the release should not be dangerous for the marine ecosystem.

Numerous studies have analyzed the concentration fields and the geometrical characteristics of NBJs, but very few works focused on the velocity fields, and consequently on turbulence inside the flow.

In the present study the near field behaviour of inclined negatively buoyant jets was simulated in a laboratory model and analyzed by means of Feature Tracking Velocimetry (FTV). FTV is a novel algorithm which is able to measure the velocity field. It is less sensitive to the appearance and disappearance of particles and to high velocity gradients than classical Particle Image Velocimetry (PIV). The algorithm is suitable in the presence of different seeding densities, where other techniques produce significant errors. Therefore, it is particularly appropriate for NBJs characterized by a large out-of-plane velocity, and high seeding density difference in the interface jet-surrounding fluid.

The simulation conditions were Re = 1000, a value that Ferrari et al. (2010) found larger than the critical Reynolds for the same apparatus. Two Froude numbers, Fr = 8 and 15, and three inclinations to the horizontal of 35°, 65° and 85° have been investigated. These three inclinations are relevant because they are characterized by three different behaviours: 35° is an angle where the

Coanda effect is not negligible, but it is an inclination necessary for the discharge in shallow water, where a more vertical inclination can interact with the surface (Shao et al., 2010). The inclination of 65° to the horizontal is close to 63°, which Zeitoun et al. (1970) found as the "optimal" angle to reach the maximum dilution. With an inclination of 85°, the re-entrainment phenomenon tends to appear due to the proximity between the uprising and descending jet branches of the jet flow (Ferrari et al. 2010). A vertical, simple jet with Re = 1000, was also investigated for comparison with NBJs.

The purpose of this thesis has been to increase the knowledge of the behaviour of NBJs. Progress has been made in understanding their fluid dynamics behaviour, and in particular the relative importance between buoyancy and momentum through the experimental investigation and the numerical simulations carried out in this work.

In particular, first order statistics were analyzed to determine the general behaviour of NBJs. Second and third order velocity statistics of NBJs were analyzed and compared to corresponding SJ ones to determine the effects of the buoyancy, and the non-axis-symmetric behaviour.

Results have highlighted substantial differences between buoyant and simple jets, both in terms of velocity (jet widening and axial velocity decay) and TKE (maxima and integral values) fields. In particular, NBJs widen more than simple jets and their widening rate, after the initial stage, is larger than in simple jets. Furthermore, the NBJ centreline velocity decay is larger due to their more pronounced widening with respect to the simple jet one. For the same reason, the obtained trend is steeper for Fr = 8 with respect to Fr = 15.

Moreover, the TKE in the lower region of the jet tends to be higher. These higher values in the lower region are due to the local unstable stratification, with more intense velocity fluctuations due to the different directions of local momentum and buoyancy.

Looking at the fluctuations of the velocities on the jet axis, another important observation is that, NBJs have an isotropic behaviour due to the buoyancy forces. This is evident in particular in the ratio between the stream-wise and the span-wise turbulence intensities. Another difference observed concerns the Reynolds stresses at the centreline, for simple jets are equal to zero, for NBJs, due to the buoyancy forces that act in a different direction compared to that of the momentum, the values are different from zero and the Reynolds stresses stay positive.

The skewness in the stream-wise direction was calculated. The values tend to be isotropic, closer to the orifice for NBJs than for SJ.

The influence of the inclination in NBJs is more relevant only in the second order statistics; in particular in the integral stream-wise decay of TKE. The position of the peak does not change, but the values are larger for smaller inclination.

Finally, a preliminary Computational Fluid Dynamics (CFD) investigation of NBJs has been conducted using an Immersed Boundary algorithm. The model can simulate the behaviour of the jet near the diffuser with reasonable approximation, but tends to underestimate the maximum height of the jet and the dilution levels. It is noticeable that the model tends to overestimate the stabilizing influence of the buoyancy forces and consequently allowing a laminar behaviour to the NBJ with Fr=8.

# Bibliography


- Abraham G.: 1967 "Jets diffusion in stagnant ambient fluid" Delft Hydraulic Laboratory publication, No 29
- Adrian R.J., Yao C.S.: 1984 "Development of pulsed laser velocimetry for measurement of turbulent flow" Proc. Symp. Turb. University of Missoury, Rolla
- Adrian R.J.: 1991 "Particle-imaging techniques for experimental fluid mechanics", Annual Review of Fluid Mechanics, 261-303
- Ahmad N., Baddour R.E.: 2012 "Dilution and penetration of vertical negatively buoyant thermal jets" J. Hydraul. Eng. 1061
- Antonia R.A., Burattini P.: 2004 "Small-scale turbulence: how universal is it?" In: Proc. of 15th Australasian Fluid Mechanics Conference, Sidney, Australia
- Apsley, D: 2013 "Introduction to CFD". SPRING 2014.
- Ashgriz N., J Mostaghimi: 2002 “An Introduction to Computational Fluid Dynamics” in Chapter 20 in Fluid Flow Handbook. McGraw Hill Publishing.
- Avanzini C.: 2006 "An outline of common practical problems and solutions in the diffuser design" In: Avanzini, C (Ed.): Proceedings of MWWD & IEMES 2006, Antalya (Turkey), 6-10/11 2006
- Baines, W.D., Turner, J.S., Campbell, J.H.: 1990 "Turbulent fountains in a open chamber" J. Fluid Mech. 212, 557-592
- Bergthorson J. M., Dimotakis P. E.: 2006 "Particle velocimetry in high-gradient/highcurvature flows" Experiments in Fluids, 41 (2), 255-263
- Black, M. J. and Anandan, P.: 1991 "Robust dynamic motion estimation over time", Proc. Computer Vision and Pattern Recognition, CVPR-91, Maui, Hawaii, June 1991, pp. 296-302.
- Bloomfield L.J., Kerr R.C.: 2002 "Inclined turbulent fountains" J. Fluid Mech. , 451, pp. 283-294
- Blumberg A.F., Ji Z.G., Ziegler C.K.: 1996 "Modeling outfall plume behavior using far field circulation model" J. Hydraulic Engineering 122(11), 610-616
- Bousanquet C.H., Horb G., Thring M.W., 1961 "The effect of density differences on the path jets" Proc. of the Royal Society of London, Series A., 263 (1314), pp. 340-352
- Boussinesque J., 1903 "Theorie analytique de la chaleur" Vol. 2 Gauthier-Villars

- Campbell, I.H., Turner, J.S.: 1989 "Fountains in magma chambers" J. Petrol. 30 885-923
- Caruso, G., Naviglio, A., Principi, P., Ruffini, E.: 2001 "High-energy efficiency desalination projects using a ful titanium desalination unit and a solar pond as the heat supply" Desalination 136, 199-212
- Cenedese A., Querzoli G.: 2005 "On the structure of a laminar buoyant jet released horizontally" J. Hydraulic Res. 43 (1) , 71-85
- Chapra, S.C., Canale, R.P.: 1988 "Numerical Methods for Engineers", McGraw-Hill, New York, 1988.
- Cipollina, A., Brucato, A., Grisafi, F., Nicosia, S.: 2005 "Bench Scale investigation of inclined dense jets" Hydraulic Eng. 131(11) , 1017-1022
- Cressewell R.W., Szczepura R.T.: 1993 "Experimental investigation into a turbulent jet with negative buoyancy" Phys. Fluids 5 (11) 2865 - 2878
- Cuthbertson A.J.S., Malcangio D., Davies P.A., Mossa M.: 2006 "The influence of a localised region of turbulence on the structural development of a turbuent, round, buoyant jet", Fluid Dynamics Research
- Daly B. J., Harlow F. H.: 1970 "Transport Equations in Turbulence" Physics of Fluids, Vol. 13, pp. 2634-2649.
- Dalziel S.B.: 1992 "Decay of rotating turbulence: some particle tracking experiments", Applied Scientific Research, 49, 217-244
- Davidson P.A.: 2004 "Turbulence - An introduction for scientists and engineers" Oxford Univeristy Press
- Donaldson C. DuP, Rosenbaum H.: 1968 "Calculation of the Turbulent Shear Flows Through Closure of the Reynolds Equations by Invariant Modeling" ARAP Report No. 127, Aeronautical Research Associates of Princeton, Princeton, NJ
- Doneker R.L., Jirka G.H. 1999 Discussion of "Mixing in Inclined Dense Jets" J. of Hydraulic Reearch, 125 pp. 317-318
- Falchi M., Querzoli G., Romano G.P.: 2006 "Robust evaluation of the dissimilarity between interrogation windows in image velocimetry" Experiments in Fluids 41 279-293
- Fan L.N., Brooks N.H.: 1969, "Numerical solution of turbulent buoyant jet problems" Report No KH-R-18, W.M. Keck Laboratory, California Institute of Technology, Pasadena
- Ferrari S., Querzoli G.: 2004 "Sea discharge of Brine from desalination Plants: A Laboratory Model of Negatively Buoyant Jets" proc. MWWD 2004 - The 3rd International Conference on Marine Waste Water Disposal and Marine Environment, Catania Italy
- Ferrari S., Querzoli G.: 2010 "Mixing and re-entrainment in a negatively buoyant jet" J. Hydraulic Research 48(5) 632-640

- Ferrari S., Querzoli G.: 2011 "Effect of Stable and Unstable Stratification on Negatively Buoyant Jets" Proceedings of 7th Int. Symp. on Stratified Flows, Rome, Italy, August 22 – 26, 2011.
- Fisher H. B., List E.J., Koh R.C.Y., Imberger J., Brooks N.H.: 1979 “Mixing in Inland and Coastal Waters” Academic Press, New York
- Frick, W.E.: (1984) "Non-empirical closure of the plume equations" Atmospheric Environment 18 (4), 653-662
- Harris C., Stephens M.: 1988, "A combined corner ans edge detector", Proc. of Fourth Alvey Vision Conference
- Heinz S., Bergstedt L., Mrosla E.: 1975, "Flow establishment and initial entrainment of heated water surface jets" St. Anthony Falls Hydraulic Laboratory, 152
- Hsiao F.B, Lim Y.C., Huang J.M.: 2010 "On the near-field flow structure and mode behavior for the right-angle and sharp-edged orifice jet" Experimental Thermal and Fluid Science 34, 1282-1289
- Hwang R.R., Chiang T.P.: 1995 "Numerical simulation of vertical forced plume in a crossflow of stably stratified fluid" J. Fluid Eng. 117, 696-705
- Hwang R.R., Chiang T.P., Yang W.C.: 1995 "Effect of ambient stratification on buoyant jets in crossflow" J. of Engineering Mechanics, 121, 865-872
- Iaccarino G., Verzicco R: 2003 “Immersed boundary technique for turbulent flow simulation” Appl. Mech Rev., 56(3)
- James W.P., Vergara I, Kim K: 1983 "Dilution of dense vertical jet" Environ Eng 109 (6), 1273-1283
- Jirka G.H.: 2004 "Integral Model for Turbulent Buoyant Jets in Unbounded Stratified Flows. Part. I: Single Round Jet" Environmental Fluid Mechanics, 4(11), 1-56
- Jirka G.H.: 2008 "Improved discharge configurations for brine effluents from desalination plants" J. of Hydraulic Engineering, 134(1) 116-120
- Kaminski, E., Tait, S., Carazzo, G.: 2005 "Turbulent entrainment in jets with arbitrary buoyancy" J. Fluid Mech. 526, 361–376.
- Kaye N. B., Hunt G. R.: 2006 "Weak fountains" Journal of Fluid Mechanics 558, 319-328
- Kean R.D., Adrian R.J. : 1991, "Optimization of Particle image velocimeters. II Multiple pulsed system" Measurement Science and Technology, Volume 2 963
- Kikkert G.A.: 2006 "Buoyant jets with Two and Three- dimensional Trajectories" PhD thesis, University of Canterbury, Christchurch, New Zeland
- Kikkert, G.A., Davidson, M.J., Nokes, R.I.: 2007 "Inclined Negatively Buoyant Discharges" Hydraulic Engineering. 133(5), 545-554
- Kleppe J.A. , Olin J.G., Menon R.K.: 2000 “Point Velocity Measurement” CRC Press LLC

- Koh, R.C.Y., Brooks, N.H.: 1975 "Fluid mechanics of wastewater disposal in the ocean" Ann. Rev. Fluid Mech. 7, 187-211
- Lai C.C.K., Lee J.H.W.: 2012 "Mixing of inclined dense jets in stationary ambient" J. of Hydro-environment Research 6 (2012) 9-28
- Lane-Serff, G.F., Linden, P.F., Hillen, M.: 1993 "Forced angled plumes" J.Hazardous Mat. 33, 75-99
- Launder B. E., Reece G. J., Rodi W.: 1975 "Progress in the Development of a Reynolds-Stress Turbulence Closure," Journal of Fluid Mechanics, Vol. 68, Pt. 3, pp. 537- 566
- Law A.W.K., Ho W.F., Monismith S.G.: 2004 "Double Diffusive Effect on Desalination Discharges" J. of Hydraulic Engineering May 2004 pp 450-457
- Law A.W.K., Lee C.C., Qi Y.: 2002 "CFD modeling of a multiport diffuser in an oblique current" MWWD 2002, Istanbul Turkey, September 16-20, 2002"
- Lee J.H.W., Chu V.H.: 2003, "Turbulent jets and plumes - A Lagrangian Approach", Kluwer Academic Publishers
- Lesieur M., Metais O.: 1996. “New trends in large-eddy simulations of turbulence.” Ann. Rev. Fluid Mech. 28:45-82.
- Lindberg, W.R., Petersen, J.D.: 1991 "Negatively buoyant jet (or plume) with application to snowplow exit flow behavior" Transportation Res. Record. 1304, 219-229
- Lindberg W.R., 1994 "Experiments on negatively buoyant jets with and without cross-flow" Recent Research Advances in Fluid Mechanics of Turbulent jets and plumes pp 131-145 Kluwer Academic Publishers
- List E.J.: - 1982 "Mechanics of turbulent buoyant jets and plumes" Turbulent Buoyant jets and Plumes, Pergamon p. 1-68
- Lumley: 1970 "Toward a Turbulent Constitutive Equation." Journal of Fluid Mechanics, Vol. 41, pp. 413-434.
- Malvern L.E.: 1969 "Introduction to the Mechanics of a Continuous Medium", Prentice-Hall, Englewood Cliffs, NJ
- McLellam, T.N., Randall, R.: 1986 "Measurement of brine jet height and dilution" J. Water, Port, Coast, Ocean Eng. 112(2) , 200-216
- McClimans, T., Eidnes, G.: 2000 "Forcing nutrients to the upper layer of a fjord by a buoyant plume" Proc. 5$^{th}$ Intl. Symp. Stratified Flows Vancouver, 199-204
- Menter F. R.: 1994 "Two-Equation Eddy-Viscosity Turbulence Models for Engineering Applications" *AIAA Journal*, 32(8):1598-1605
- Mi J., Nathan G.J., Nobes, D.S.: 2001 "Mixing characteristics of axisymmetric free jets from a countered nozzle, an orifice plate and a pipe" J. of Fluids Engineering, 123, 878-883
- Mi J., Kalt P., Nathan G.J., Wong C.Y.: 2007, " PIV measurements of a turbulent jet issuing from round sharp-edged plate" Exp. Fluids 42(4), 625-637

- Mier-Torrecilla M., Idelsohn S.R., Onate E.: 2010 "Advances in the simulation of multi-fluid flows with the particle finite element method. Application to bubble dynamics" Int. J. Numer. Meth. Fluids DOI:10,1002/fld.2429
- Mier-Torrecilla M., Geyer A., Philips J.C., Idelsohn S.R., Onate E.: 2012 "Numerical simulations of negatively buoyant jets in an immiscible fluid using the particle finite element method" Int. J. Numer. Meth. Fluids 69: 1016 -1030
- Milione M., Zeng C. 2008 "The effects of temperature and salinity on population growth and egg hatching success of the tropical calanoid copepod, Acartia sinjiensis" Acquaculture 275, pp. 116-123
- Mittal .R., Iaccarino G.: 2005 "Immersed Boundary Methods" Annu. Rev. Fluid Mech. 37, 239-261
- Mohd-Yosuf J.: 1997 "Combined immersed-boundary / B-spline methods for Simulations of flow in complex geometries" Annual Research Briefs, Center for Turbulence Research, 317-328.
- Morton B.R., Taylor G., Turner J.S.: 1956 "Turbulent gravitational convection from maintained and instantaneous source". Proc. Roy. Soc of London, Series A, 234, 1-23
- Nemlioglu, S., Roberts, P. J.: 2006: "Experiments on Dense Jets Using Three-Dimensional Laser-Induced Fluorescence (3DLIF)" MWWD-IEMES. Antalya
- Okamoto, K., Nishio, S., Saga, T. and Kobayashi, T.: 2000, "Standard images for particle-image velocimetry," Measurement Science Technology, 11, 685-691.
- Oliver C.J., Davidson M.J., Nokes R.I.: 2008 "k-ε Prediction of the initial mixing of desalination discharges" Environ Fluid Mech, 8, 617-625
- Oliver C.J., 2012: "Near field mixing of Negatively Buoyant Jets" Phd Thesis
- Palomar P., Lara J.L., Losada I.J: 2010 " Desalination in Spain: Recent developments and recommendations " Desalination 255, 97-106
- Palomar P., Lara J.L., Losada I.J., Rodrigo M., Alvàrez A.: 2012 "Near field brine discharge modeling part. 1: Analysis of commercial tools" Desalination 290, 14-27
- Palomar P., Lara J.L., Losada I.J., Rodrigo M., Alvàrez A.: 2012 "Near field brine discharge modeling part. 2: Analysis of commercial tools" Desalination 290, 28-42
- Papakonstantis I., Kampourelli M., Christodoulou G.: 2007 "Height of rise of inclined and vertical negatively buoyant jets". In: Di Silvio, G., & Lanzoni, S. (eds), Proceedings of the 32nd IAHR Congress: Harmonizing the Demands of Art and Nature in Hydraulics; Fluid Mechanics and Hydraulics theme.

- Papakonstantis I. G., Christodoulou G. C., Papanicolaou P. N.: 2011a. "Inclined negatively buoyant jets 1: geometrical characteristics". J. of Hydraulic Research, 49(1), 3–12.
- Papakonstantis I. G., Christodoulou G. C., Papanicolaou P. N.: 2011b. "Inclined negatively buoyant jets 2: concentration measurements" J. of Hydraulic Research, 49(1), 13–22.
- Papanicolau P.N., Papakonstantis I.G., Christodoulou G.C.: 2008 "On the entrainment coefficient in negatively buoyant jets" J. Fluid Mech. 614, 447-470
- Patankar, S.V.: 1980 "Numerical Heat Transfer and Fluid Flow" Hemisphere, Washington, DC, 1980
- Peskin C.S.: 1972 "Flow patterns around heart valves: a digital computer method for solving the equation of motion" PhD thesis. Physiol., Albert Einstein Coll. Med., Univ. Microfilms , 378, 72-30
- Plumb B.R.: 2008 "Modeling desalination plant outfalls sedimentation" Final thesis report. University of New South Wales at the Australia Defence Force Academy
- Pope S.B.: 2000 "Turbulent Flows" Cambridge University Press
- Prandtl L.: 1910 "Bericht uber Untersuchungen zur ausgebildeten Turbulenz" Zsangew. Math. Mech. 5, 136-139
- Prasad A.K.: 2000, “Particle image velocimetry” Current Science, 79 (1)
- Priestley C.H.B., Ball Q.J.R. 1955, "Continuous convection from an isolated source of heat" Meteorol. Soc., 81, 144-157
- Querzoli, G.: 1996 "A Lagrangian study of particle dispersion in the unstable boundary layer", Atmospheric Environment, 30(16), 2821-2829
- Quinn W.R.: 2006 "Upstream nozzle shaping effects on near field flow in round turbulent free jets" European Journal of Mechanics B/Fluids 25, 279 - 301
- Raffel M., Willert C., Werelwy S., Kompenhans J.: 2007 "Particle Image Velocimetry - A practical Guide" Springer
- Roberts, P.J. W., Toms, G.: 1987 "Inclined dense jets in a flowing current" J. Environmental. Engineering., ASCE 114(5), 1175-1191
- Roberts Philip J.W. ,Ferrier A., Daviero G.: 1997 "Mixing in Inclined Dense jets" J. Hydraulic Eng. 123(8) , 693-699
- Roberts Philip J.W. ,Ferrier A., Daviero G.: 1999 Closure to "Mixing in Inclined Dense jets" J. Hydraulic Eng. 125(3) , 318-319
- Roberts P.J.W., Salas H.J., Reiff F.M., Libhaber M., Labbe A., Thomson J.C.: 2010 “Marine Wastewater Outfalls and Treatment System” IWA Publishing
- Seil, G. J., & Zhang, Q.: 2010 "CFD modelling of desalination plant brine discharge systems" Journal of the Australian Water Association, Sept 2010, 51-54.

- Shao S., Law A.W.K.: 2011 "Boundary Impingement and attachment of horizontal offset dense jets" J. of Hydro-environment Research 5 (2011)15-24
- Shao D.: 2010 "Desalination discharge in shallow coastal water" Phd thesis
- Smagorinsky J.: 1963 “General circulation experiments with the primitive equations” Mon. Weather Rev. 91:99–165.
- Speziale C. G.: 1987 "Second-Order Closure Models for Rotating Turbulent Flows," Q. Appl. Math., Vol. 45, pp. 721-733.
- Tang H.S., Paik J., Sotiropoulos F., Khangaonkar T.: 2008 "Three-dimensional numerical modeling of initial mixing of thermal discahrges at real-life configurations", J. Hydraulics Eng., 134(9), 1210 - 1224
- Turner, J.S.: 1966 "Jets and Plumes with negative or Reversing Buoyancy " J. of Fluid Mechanics, Vol. 26, Part 4, 779-792
- Vafeiadou P, Papakonstantis I, Christodoulou: 2005 "Numerical Simulation of Inclined negatively buoyant jets" Proc. of the 9th International Conference on Environmental Science and Technology
- Wang H.W., Law A.W.K.: 2002 "Second-order integral model for a round turbulent buoyant jet" J. of Fluid Mechanics 459 397-428
- Westerweel J.: 1993 "Digital Particle Image Velocimetry - Theory and Application" Delft University Press
- Westerweel J., Scarano F.: 2005 "Efficient detection of spurious vectors in particle image velocimetry data", Experiments in Fluids, 16 236-247
- Yannopoulos, P.C., Noutsopoulos, G.C.: 2006a "Interaction of vertical round turbulent buoyant jets 1: Entrainment restriction approach." J. Hydraulic Res. 44(2), 218–232.
- Yannopoulos, P.C., Noutsopoulos, G.C.: 2006b "Interaction of vertical round turbulent buoyant jets 2: Superposition method" J. Hydraulic Res. 44(2), 233–248.
- Zeitoun, M.A., McIlhenny, W.F., and Reid, R.O.: 1970 "Conceptual Designs on Outfall Systems for Desalination Plants" Report No. 550, Office of sSaline Water, US Department of Interior, Washington
- Zhang H., Baddour, R. E.: 1998 "Maximum penetration of vertical round dense jets at small and large Froude numbers." J. of Hydraulic Engineering, 124(5), 550–552.